DTIC
S ELECTE
JUN 1 6 1992
C D

②

AD-A251 485

An Experimental Investigation Of an Acoustic Technique To Determine Shallow Water Bottom Boundary Impedance

Lynne M. Maiocco-Dillman
Environmental & Tactical Support Systems Department

Naval Undersea Warfare Center Detachment
New London, Connecticut

92-15391

92 (

REPORT DOCUMENTATION PAGE

Form Approved
OMB No. 0704-0188

1. AGENCY USE ONLY (Leave blank)	2. REPORT DATE 1 May 1992	3. REPORT TYPE AND DATES COVERED Thesis

4. TITLE AND SUBTITLE

An Experimental Investigation of an Acoustic Technique to Determine Shallow Water Bottom Boundary Impedance

5. FUNDING NUMBERS

6. AUTHOR(S)

Lynne M. Maiocco-Dillman

7. PERFORMING ORGANIZATION NAME(S) AND ADDRESS(ES)

Naval Undersea Warfare Center Detachment
New London, CT 06320

8. PERFORMING ORGANIZATION REPORT NUMBER

TR 10,045

9. SPONSORING/MONITORING AGENCY NAME(S) AND ADDRESS(ES)

10. SPONSORING/MONITORING AGENCY REPORT NUMBER

11. SUPPLEMENTARY NOTES

12a. DISTRIBUTION/AVAILABILITY STATEMENT

Approved for public release; distribution is unlimited.

12b. DISTRIBUTION CODE

13. ABSTRACT (Maximum 200 words)

Acoustic propagation is highly dependent on bottom properties, particularly in shallow water. In the past, bottom properties have been determined directly (e.g., using core samples). An alternate method of determining bottom properties uses inverse techniques, obtaining geophysical parameters by means of acoustic data. Calibrated acoustic measurements were made on the New Jersey continental shelf in an area with known geophysical properties. The experiment was conducted under known oceanographic conditions that were shown by measurements of temperature, salinity, and sound speed versus depth. The acoustic measurements were performed with a vertical array of 24 equally spaced hydrophones, one of which was positioned on the bottom. A calibrated source transmitted discrete frequencies between 10 and 600 Hz for the collection of data. Low frequencies between 10 and 50 Hz were transmitted at discrete locations close to the measurement array. The water/sediment boundary impedance was calculated from the ratio of velocity to pressure. The normal component of the velocity can be related to the pressure gradient measured by the equally

14. SUBJECT TERMS

Boundary Impedance
Ocean Bottom Impedance

15. NUMBER OF PAGES

132

16. PRICE CODE

17. SECURITY CLASSIFICATION OF REPORT	18. SECURITY CLASSIFICATION OF THIS PAGE	19. SECURITY CLASSIFICATION OF ABSTRACT	20. LIMITATION OF ABSTRACT
UNCLASSIFIED	UNCLASSIFIED	UNCLASSIFIED	SAR

13. Abstract (Cont'd.)

spaced hydrophones close to the boundary. The complex pressure can be obtained from the hydrophone lying on the bottom. The ratio of these quantities can be related to the impedance. This calculation can be compared to the impedance derived from the measured geophysical properties. The experimental pressure versus depth profiles were compared to theoretical pressure profiles calculated by the computer model SAFARI by use of a representative model of the medium derived from measured geophysical properties. Transmission loss and wavenumber spectra data were obtained at frequencies between 50 and 600 Hz. The analysis of these results and comparisons with theory (SAFARI) provided supportive information with regard to determining the character of the medium.

LIST OF CONTENTS

i

LIST OF FIGURES

LIST OF TABLES

1 Introduction

The acoustic properties of the sea-bed are influential in controlling sound propagation in shallow water. Presently, the properties of the sea-bed are characterized by the compressional wave speed and attenuation for each layer in the sediment. Acoustic models such as SAFARI (Schmidt 1988) use these parameters to predict the sound field. An acoustic technique for estimating one of the properties, the impedance of the sea-bed, is the topic of this dissertation. The normal acoustic impedance is the product of the density and sound speed in the medium.

In the past, bottom properties have been determined directly using core samples. In deep water, where sediment cover is thick and more homogeneous, the propagation predictions using these core samples are generally accurate. However, in shallow water, a wide variety of behavior may be expected due to thinly covered and layered sediments. In addition the bottom will often be characterized by irregular stratification and anisotropy where occasional core samples may not accurately represent the sedimental properties.

The method proposed in this study measures the impedance acoustically using a vertical array of hydrophones, one hydrophone placed on the ocean bottom. This acoustic technique is advantageous in that it provides an in situ evaluation of impedance and is easier to implement

than the complicated process of taking core samples. Acquiring core samples involves significant time and expense due to the fact that a core is drilled from the sediment and transported to a laboratory which measures the sediment properties. The proposed method of determining impedance does not disturb the sediment. For this reason numerous samples could be obtained for a given area resulting in a more accurate representation of the sediment area.

The derivation of impedance is treated in many textbooks (Brekhovskikh 1980). In this dissertation, an experimental investigation of the vertical sound pressure distribution and of the impedance of the bottom will be described. Additional measurements of transmission loss and wavenumber spectra will be compared to theoretical predictions input with the geo-acoustical estimates obtained in previously documented investigations to validate and better understand the medium (bottom).

To facilitate an understanding of shallow water propagation, a mathematical derivation of the sound pressure field radiating from a point source in a homogeneous medium is presented. At the upper boundary (the surface), the sound pressure is equal to zero. At the lower boundary (the sea bottom), the pressure is expressed in terms of a normal acoustic impedance Z. The concept of acoustic impedance for the sea bottom results from an extension of the standard theory for a reflection of plane waves at the boundary between two media. For plane waves at normal incidence, the

2

acoustic impedance is defined as the ratio between the pressure and the normal particle velocity at the boundary.

Received pressure levels versus depth were collected using a vertical measurement array with a bottom mounted-hydrophone. Thus the pressure and the pressure gradient were measured at the boundary. Horizontal wavenumber spectra using a Hankel transform technique developed by Frisk and Lynch (1984) and transmission loss were obtained from the pressure versus range data.

Prior to the experiment, an extensive survey (Trevor-row et al. 1988) of the measurement area yielded estimated geo-acoustical properties of the sediment. Estimated values for the compressional and shear wave speed, attenuation, and density of the sediment were compared to measured geophysical data obtained from the AMCOR 6010 borehole. Seismic profiles of the sediment interface were available from The U.S. Geological Survey and from the Huntec Deep Towed Seismic boomer profiles. The Huntec survey conducted on the New Jersey shelf and the U.S. Geological Society data were evaluated in a report by Milliman (1989). During the experiment, oceanographic data were collected in the form of velocity profiles and bathymetry data. Wind and wave conditions were observed and recorded. The estimated geo-acoustical parameters were used as input for the acoustic prediction model SAFARI. The measured geophysical value of density and estimated value of sound speed could also be used as a comparison of the acoustically measured impedance

defined as the product of density and sound speed in the medium.

This dissertation describes a technique for determining the normal impedance using measurements of the pressure gradient in the water column. The experimental values are compared to theoretical predictions using SAFARI and the measured impedance resulting from the geophysical survey. SAFARI uses numerical methods to predict the sound field given the measured geophysical and geo-acoustical parameters. Measured and predicted transmission loss and wavenumber spectra are compared to examine the ability of SAFARI to accurately predict the sound field.

2 Background

The transmission of sound in the ocean is dependent on many factors. Of significant importance are: the depth of the water over the propagating path, the velocity of sound, the position of the source of excitation in the water column, the physical properties of the ocean bottom, and the roughness of the ocean surface. Since the solution of the wave equation involving all these variables is much too complicated and generally not attainable, a simplified model of the considered environment will be presented so that sound propagation in a waveguide may be understood. In the realistic situation where the properties in the ocean and sediment change continuously with depth, numerical methods must be used to obtain an evaluation for the given case.

2.1 Theory

In the following section, Section 2.1.1, a simple model where the ocean and the sediment are homogeneous is developed. The basis of this is contained in Officer (1958) with subsequent references to Pekeris (1948) and others as noted. The development of Officer (1958) is adapted to the purposes of this dissertation and is included in the completeness of the work for the ease of the reader.

In Section 2.1.2, the reflection of plane waves on a boundary is developed to yield the Rayleigh reflection coefficient. At normal incidence the Rayleigh reflection coefficient is shown to be the ratio of the relative impedances of the water and sediment, respectively.

The method of determining boundary impedance is presented in Section 2.1.3. The normal component of the complex impedance can be defined as the ratio of the pressure at the boundary to the velocity multiplied by the density of water. The development of the velocity potential and pressure in Section 2.1.1 is used as the basis for the computations of the experimental results. These results can then be compared with the Rayleigh reflection coefficient at normal incidence developed in Section 2.1.2.

Comparisons of the data with theory required the use of numerical computer models such as SAFARI (Schmidt 1988). Measured geophysical data were used to generate the geoacoustical parameters, such as compressional and shear wave

6

speeds and attenuation versus depth, necessary for the calculation. A brief summary of the basic theory of SAFARI will be presented.

2.1.1 Wave Equation and Solution in the Form of Velocity Potential

A simple acoustic model of the ocean is one where the water density ρ_1 and sonic velocity c_1 are homogeneous and where the ocean bottom is a liquid having a different density ρ_2 and sonic velocity c_2. The sound source is a point source situated at a depth d in a water column of depth H. The surface and bottom are parallel planes, as shown in Figure 2-1. The wave equation is the governing differential equation which describes the transmission of sound in the medium, and given in symmetrical cylindrical coordinates r and z is

$$\nabla^2 \psi = \frac{1}{r}\frac{\partial}{\partial r}\left(r\frac{\partial \psi}{\partial r}\right) + \frac{\partial^2 \psi}{\partial z^2} = \frac{1}{c^2}\frac{\partial^2 \psi}{\partial t^2} \qquad 2-1$$

A variable separable solution is assumed for a simple harmonic source transmitting a circular frequency: ω.

$$\psi = e^{i\omega t}M(r)F(z) \qquad 2-2$$

Differentiating equation 2-2 and substituting into equation 2-1 gives

$$\frac{\left(\frac{d^2F}{dz^2}\right) + \left(\frac{\omega^2}{c^2}\right)F}{F} = \frac{-\frac{d^2M}{dr^2} - \left(\frac{1}{r}\right)\left(\frac{dM}{dr}\right)}{M} \qquad 2-3$$

SURFACE

$z=0$

$z=d$

$\rho_1 c_1$

SOURCE

$\rho_1 c_1$

$z=H$

$\rho_2 c_2$ BOTTOM
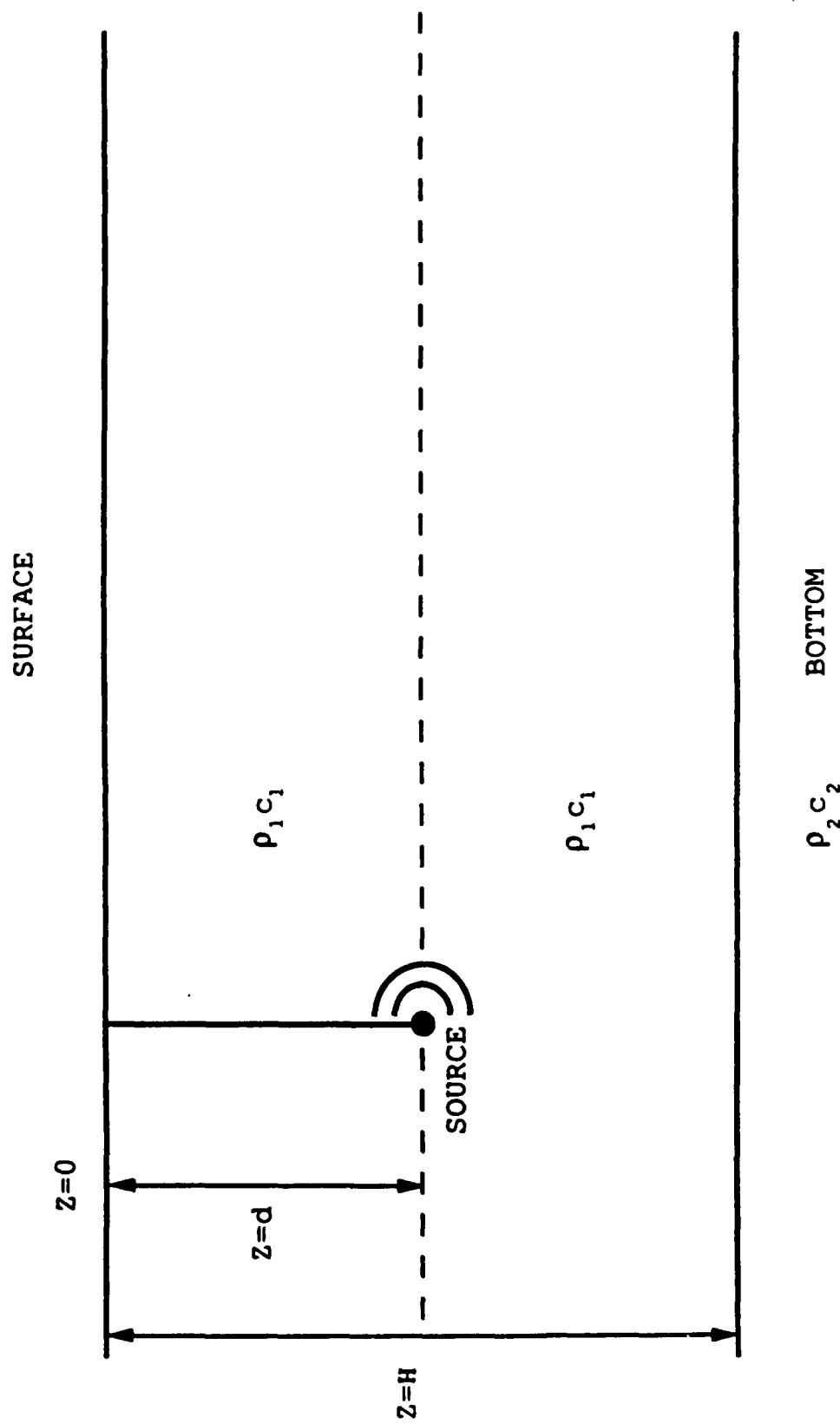
Figure 2-1 Homogeneous Model of the Ocean

8

Since the above equation is true for all r and z, the expressions on each side of the equality must be equal to a constant called k^2. The constant k is the water wavenumber defined as $\frac{\omega}{c}$. The water wavenumber squared k^2 can be represented by the sum of the squares of the horizontal and vertical wavenumbers k_h^2 and k_v^2. The horizontal wavenumber can be defined as $k_v = \frac{2\pi}{\lambda}\cos(\theta)$ and the vertical wavenumber can be defined as $k_h = \frac{2\pi}{\lambda}\sin(\theta)$ where θ denotes the angle of incidence of the elementary waves. We have then

$$\frac{d^2M}{dr^2} + \frac{1}{r}\frac{dM}{dr} + k^2 M = 0 \qquad\qquad 2-4$$

and

$$\frac{d^2F}{dz^2} + (\frac{\omega^2}{c^2} - k^2)F = 0 \qquad\qquad 2-5$$

The solution to equation 2-4 is the zero order Bessel function

$$M = J_0(kr) \qquad\qquad 2-6$$

A general form of the solution to equation 2-5 may be written in complex form as

$$F = e^{(+/-)i\beta z} \qquad\qquad 2-7$$

where

$$\beta = \sqrt{\frac{\omega^2}{c^2} - k^2}$$

The form of the solution to equation 2-7 depends on the sign of β^2. When $\frac{\omega^2}{c^2} > k^2$, β is a real quantity, the fundamental solution becomes

$$F = e^{(+/-)i\beta z}$$

When $\frac{\omega^2}{c^2} < k^2$, β becomes an imaginary quantity and the solution becomes

$$F = e^{(+/-)\beta z}$$

The solution with the positive βz is not realized as the pressure grows without bounds as z increases. Because the Sommerfeld Radiation Condition must be satisfied $(P \rightarrow 0, z \rightarrow \infty)$, this root will disappear. Thus, the fundamental solution can be written as

$$\psi = e^{i\omega t} J_0(kr) e^{(+/-)i\beta z} \qquad k^2 < \frac{\omega^2}{c^2} \qquad \text{2-8}$$

or

$$\psi = e^{i\omega t} J_0(kr) e^{-\beta z} \qquad k^2 > \frac{\omega^2}{c^2}$$

These fundamental solutions can be applied to the wave equation for each layer:

$$\nabla^2 \psi_j = \frac{1}{c_j} \frac{\partial^2 \psi_j}{\partial t^2} \qquad j = 1, 2, 3 \ldots \qquad \text{2-9}$$

where

$$\beta_1 = \sqrt{\frac{\omega^2}{c_1^2} - k^2} \qquad k < \frac{\omega}{c_1}$$

$$\beta_1 = -i \sqrt{k^2 - \frac{\omega^2}{c_1^2}} \qquad k > \frac{\omega}{c_1} \qquad \text{2-10}$$

and

$$\beta_2 = \sqrt{\frac{\omega^2}{c_2^2} - k^2} \qquad k < \frac{\omega}{c_2}$$

$$\beta_2 = -i\sqrt{k^2 - \frac{\omega^2}{c_2^2}} \qquad k > \frac{\omega}{c_2}$$

For F in regions 1, 2, and 3, the solutions for F from equation 2-7 are

$$F_1 = A\sin(\beta_1 z) + E\cos(\beta_1 z)$$

$$F_2 = B\sin(\beta_1 z) + C\cos(\beta_1 z) \qquad \text{2-11}$$

$$F_3 = De^{-i\beta_2 z} + Ge^{i\beta_2 z}$$

Long range propagation is primarily composed of multiple reflections within the water column and no significant contributions are made through the lower media. For this to be physically realizable, we will assume β to be a real quantity in regions 1 and 2 and imaginary, in region 3. If we choose β_1 to be imaginary this represents propagation outward from the source into the lower medium. The constant G in Eq 2-11 must equal zero so that F_3 will decrease exponentially with depth. If β_2 were imaginary and negative, this would make F_3 exponentially increase with depth, which would be physically impossible. The constants A, B, C, D, E, and G are determined by the boundary conditions.

It is convenient to solve the wave equation in terms of the velocity potential. The pressure field is determined from the potential ψ by the following:

$$p = \rho\frac{\partial \psi}{\partial t} \quad , \quad \dot{q} = \frac{\partial \psi}{\partial r} \quad , \quad \dot{w} = \frac{\partial \psi}{\partial z} \qquad \text{2-12}$$

11

where p is the pressure, q is the horizontal, and w is the vertical velocity components. At $z = 0$, the pressure must be equal to zero, which would make F_1 equal zero. At depth H, the continuity of pressure must be satisfied, which gives us

$$\rho_1 F_2 = \rho_2 F_3$$

$$\frac{dF_2}{dz} = \frac{dF_3}{dz} \qquad at \ z = H \qquad\qquad 2\text{-}13$$

At the source depth $z = d$, we must satisfy the continuity of pressure requirement, which gives us

$$F_1 = F_2 \qquad\qquad at \ z = d \qquad 2\text{-}14$$

The boundary condition for the continuity of velocity is more complex and can be treated in a number of ways. It is difficult because w is continuous everywhere except at the source where the water moves in opposite directions above and below the source. If we may say that $\frac{dF_1}{dz} = k$ at the discontinuity, then the difference becomes

$$\frac{dF_1}{dz} - \frac{dF_2}{dz} = 2k \qquad\qquad at \ z = d \qquad 2\text{-}15$$

Officer refers to this condition as a subterfuge. Basically, the condition follows from the principle of superposition and the expansion of the source field in terms of the fundamental solutions Φ_1 and Φ_2. This requires $\frac{\partial \Phi_s}{\partial z}$, $\frac{\partial \Phi_1}{\partial z}$ and $\frac{\partial \Phi_2}{\partial z}$ to be equal on a term-by-term basis near the source yielding this condition. Substituting equation 2-11 into

equations 2-13, 14, and 15, we see that E must be equal to zero and we get

$$A\sin(\beta_1 d) - B\sin(\beta_1 d) - C\cos(\beta_1 d) = 0$$

$$A\beta_1\cos(\beta_1 d) - B\beta_1\cos(\beta_1 d) + C\beta_1\sin(\beta_1 d) = 2k$$

$$B\rho_1\sin(\beta_1 H) + C\rho_1\cos(\beta_1 H) - D\rho_2 e^{-i\beta_2 H} = 0$$

$$B\beta_1\cos(\beta_1 H) - C\beta_1\sin(\beta_1 H) + iD\beta_2 e^{-i\beta_2 H} = 0 \qquad 2-16$$

If we solve for the constants A, B, C, D and then define b as $\dfrac{\rho_1}{\rho_2}$ we obtain

$$A = \frac{2k}{\beta_1}\left[\frac{\beta_1\cos[\beta_1(H-d)] + ib\beta_2\sin[\beta_1(H-d)]}{\beta_1\cos(\beta_1 H) + ib\beta_2\sin(\beta_1 H))}\right]$$

$$B = \frac{2k\sin(\beta_1 d)}{\beta_1}\left[\frac{\beta_1\sin(\beta_1 H) - ib\beta_2\cos(\beta_1 H)}{\beta_1\cos(\beta_1 H) + ib\beta_2\sin(\beta_1 H)}\right]$$

$$C = \frac{2k\sin(\beta_1 d)}{\beta_1}$$

$$D = \frac{2bke^{-ik\beta_2 H}\sin(\beta_1 d)}{\beta_1\cos(\beta_1 H) + ib\beta_2\sin(\beta_1 H)} \qquad 2-17$$

The velocity potential is obtained by substituting equation 2-17 into 2-11 and then into the wave equation solution, equation 2-8. To obtain the total solution, the velocity potential is integrated with respect to k over the region of zero to infinity. A solution for each region is then

$$\Phi_1 = e^{i\omega t}\Psi(r, z, \omega) \qquad 2-18$$

$$\Phi_1 = 2e^{i\omega t}\int_0^\infty J_0(kr)k\,dk\,\frac{\sin(\beta_1 z)}{\beta_1}\left[\frac{\beta_1\cos[\beta_1(H-d)] + ib\beta_2\sin[\beta_1(H-d)]}{\beta_1\cos(\beta_1 H) + 1b\beta_2\sin(\beta_1 H)}\right]$$

13

$$\Phi_2 = e^{i\omega t}\Psi(r,z,\omega) \qquad\qquad 2-19$$

$$\Phi_2 = 2e^{i\omega t}\int_0^\bullet J_0(kr)kdk\frac{\sin(\beta_1 d)}{\beta_1}\left[\frac{\beta_1\cos[\beta_1(H-z)]+ib\beta_2\sin[\beta_1(H-z)]}{\beta_1\cos(\beta_1 H)+ib\beta_2\sin(\beta_1 H)}\right]$$

$$\Phi_3 = e^{i\omega t}\Psi(r,z,\omega) \qquad\qquad 2-20$$

$$\Phi_3 = 2e^{i\omega t}\int_0^\bullet J_0(kr)kdk\frac{\sin(\beta_1 d)e^{-i\beta_2(z-H)}}{\beta_1\cos(\beta_1 H)+ib\beta_2\sin(\beta_1 H)}$$

The above expressions are formal solutions for the velocity potential for a periodic point source. Equation 2-19 will be used to determine the pressure distribution as a function of depth for the analysis of the boundary impedance technique.

The normal mode solution is obtained by the transformation and evaluation of the integral in equation 2-19 into the wavenumber (k) domain. In this evaluation, β_1 and β_2 are multi-valued functions with roots or branch points at

$$k_1 = \frac{\omega_1}{c_1} \quad , \quad k_2 = \frac{\omega}{c_2} \qquad\qquad 2-21$$

and the normal modes are obtained from the residues of the integral in the k plane. Normal modes may be thought of as mutually reinforced image waves travelling in certain particular directions together with their reflections at the surface and bottom. The k plane is cut up as shown in Figure 2-2, where to the left of k_1

$$\beta_1 = \sqrt{k_1^2-(k_1-i\alpha)^2} = \sqrt{\alpha^2-i2\alpha k_1} \qquad Re(k) < \frac{\omega}{c_1} \qquad\qquad 2-22$$

14
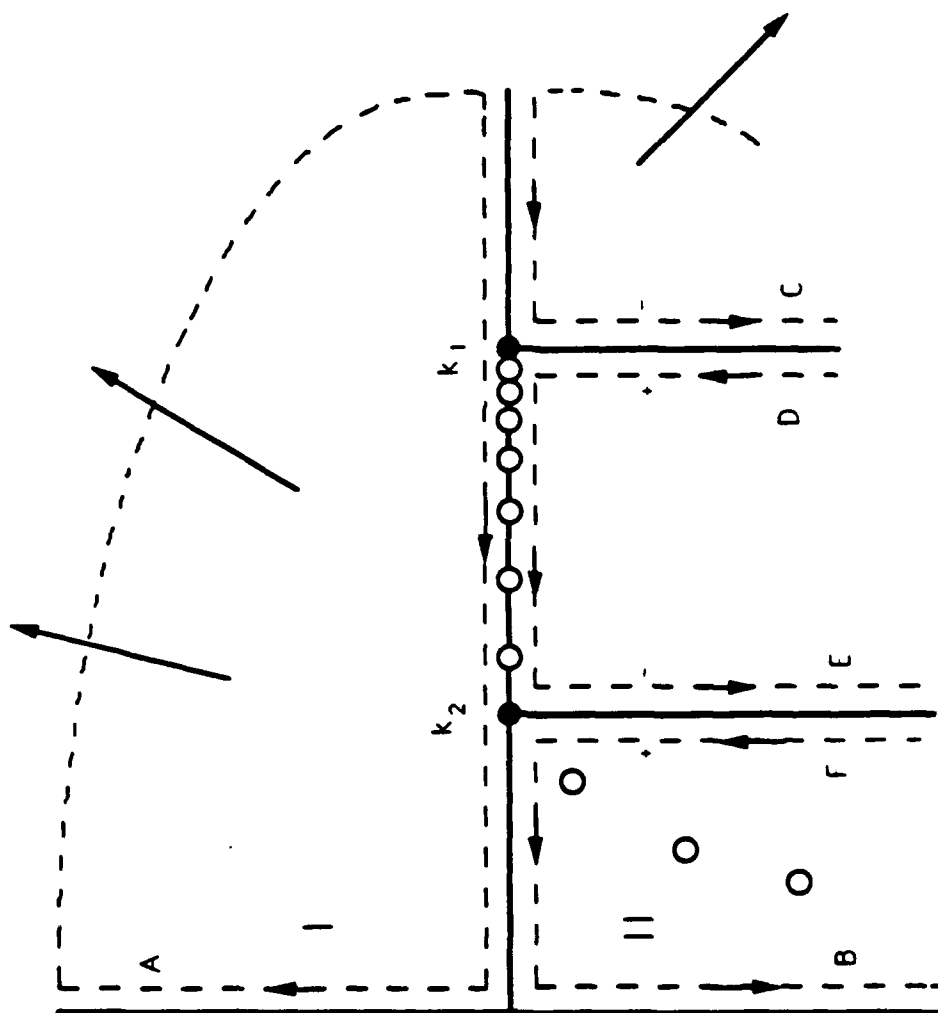
Figure 2-2 Branch Cuts for k Plane Integration

and to the right of k_1

$$\beta_1 = -i\sqrt{(k_1 - i\alpha)^2 - k_1^2} = -i\sqrt{-(\alpha^2 - i2\alpha k_1)}$$

$$= -\sqrt{\alpha^2 - i2\alpha k_1} \qquad\qquad Re(k) > \frac{\omega}{c_1}$$

β_2 will remain the same. The signs of β_1 and β_2 change across the k_1 and k_2 branch lines, respectively. The poles of the integrand equation 2-19 lie on the real axis between k_1 and k_2 if $c_1 < c_2$ or in the fourth quadrant if $c_1 > c_2$. Substituting

$$2J_0(kr) = H_0^{(1)}(kr) + H_0^{(2)}(kr) \qquad\qquad 2\text{-}23$$

into equation 2-19 where $H_0^{(1)}$ and $H_0^{(2)}$ are Hankel functions of the first and second kind and integrating, we have, from Cauchy's integral theorem,

$$\int_0^\infty H_0^{(1)}(kr)F(\beta_1,\beta_2)k\,dk = \left(\int_{A^0}^{i\infty} + \lim_{k\to\infty}\int_{i\infty}^0 \right) H_0^{(1)}(kr)F(\beta_1,\beta_2)k\,dk \qquad 2\text{-}24$$

and

$$\int_0^\infty H_0^{(2)}(kr)F(\beta_1,\beta_2) = \left(\int_0^{-\infty\,B} + \lim_{k\to\infty}\int_{-i\infty}^0 + \int_{k_1}^{-\infty\,C} + \int_{-i\infty}^{k_1\,D} + \int_{k_2}^{-i\infty\,E} + \int_{-i\infty}^{k_2\,F} \right)$$

$$H_0^{(2)}(kr)f(\beta_1,\beta_2)k\,dk + \sum RESIDUES \qquad 2\text{-}25$$

where $F(\beta_1,\beta_2)$ is defined as

$$F(\beta_1,\beta_2) = \frac{\sin(\beta_1 d)}{\beta_1}\left[\frac{\beta_1\cos[\beta_1(H-z)] + ib\beta_2\sin[\beta_1(H-z)]}{\beta_1\cos(\beta_1 H) + ib\beta_2\sin(\beta_1 H)} \right] \qquad 2\text{-}26$$

The evaluation of the integral equation 2-19 is best defined as the sum of equations 2-24 and 2-25. If we note that $H_0^{(1)}$ vanishes at ∞ over the first quadrant and $H_0^{(2)}$

vanishes at ∞ over the second quadrant, we are left with, after reductions and cancellations,

$$\Psi = \int_{-i\infty}^{k_2} H_0^{(2)}(kr)k\,dk[F(\beta_1,\beta_2)-F(\beta_1-\beta_2)]+\sum RESIDUES \qquad 2-27$$

The residues, as stated earlier, are the normal modes located at the values of $k=k_n$ for which the denominator of equation 2-26 is equal to zero:

$$\beta_1\cos(\beta_1 H)+ib\beta_2\sin(\beta_1 H)=0$$

$$or \qquad\qquad\qquad \beta_2=\frac{i\beta_1}{b\tan(\beta_1 H)} \qquad\qquad 2-28$$

The residues are equal to, using Cauchy's integral formula

$$\Psi' = \sum RESIDUES \int H_0^{(2)}(kr)F(\beta_1,\beta_2)k\,dk \qquad 2-29$$

$$= -2\pi i\sum_n H_0^{(2)}(k_n r)k_n\left(\frac{\sin(\beta_1 d)\{\beta_1\cos[\beta_1(H-z)]+ib\beta_2\sin[\beta_1(H-z)]\})}{\beta_1\left(\frac{\partial}{\partial k}\right)[\beta_1\cos(\beta_1 H)+ib\beta_2\sin(\beta_1 H)]}\right.$$

$$= \frac{-2\pi i}{H}\sum H_0^{(2)}(k_n r)\frac{\beta_1 H\sin(\beta_1 d)\sin(\beta_1 z)}{\beta_1 H-\sin(\beta_1 H)\cos(\beta_1 H)-b^2\sin^2(\beta_1 H)\tan(\beta_1 H)}$$

The above expression is valid for all of medium 1. The Hankel function, for large values of r, may be approximated by its asymptotic representation as

$$H_0^{(2)}(k_n r)\to\sqrt{\frac{2}{\pi k_n r}}e^{i[(\frac{\pi}{4})-k_n r]}=i\sqrt{\frac{2}{\pi k_n r}}e^{-i[k_n r+(\frac{\pi}{4})]} \qquad 2-30$$

Substituting equation 2-30 into equations 2-29 and 2-19 gives

$$\Phi_2' = \frac{2\pi}{H}\sqrt{\frac{2}{\pi r}}\sum_{n=1}^{\infty}e^{i[\omega t-k_n r-(\frac{\pi}{4})]}G(K_n)\sin(\beta_1 d)\sin(\beta_1 z) \qquad 2-31$$

where $G(k_n)$ is

$$G(k_n) = \frac{1}{\sqrt{k_n}} \; \frac{\beta_1 H}{\beta_1 H - \sin(\beta_1 H)\cos(\beta_1 H) - b^2 \sin^2(\beta_1 H)\tan\beta_1 H} \qquad 2\text{-}32$$

The residues define the propagation in the r direction with a phase velocity V for each mode:

$$V_n = \frac{\omega}{k_n} \qquad 2\text{-}33$$

The amplitude variation is a function of the source depth d and receiver depth z and is given by $\sin(\beta_1 d)\sin(\beta_1 z)$. The relative strength of each mode is defined by the function $G(k_n)$. In addition, the velocity potential is inversely proportional to the square root of the range. Using the definition $b = \frac{\rho_1}{\rho_2}$ and substituting equations 2-3 and 2-10 into 2-18 yields an equation for real values of k_n for unattenuated propagation:

$$\tan(\beta_1 H) = \frac{i\beta_1}{i\beta_2} \qquad 2\text{-}34$$

$$\tan\left(\frac{2\pi f_n H}{V}\sqrt{\frac{V^2}{c_1^2} - 1}\right) = -\frac{\rho_2\sqrt{\frac{V^2}{c_1^2} - 1}}{\rho_1\sqrt{1 - \frac{V^2}{c_2^2}}} \qquad 2\text{-}35$$

Equation 2-35 is a multi-valued function with respect to frequency. It shows the relationship between the phase velocity and the frequency. The dispersion of the propagating wave results from the interference of multiple reflections. The relationship of frequency versus phase velocity can be plotted to form dispersion curves for each value of n. The first mode corresponds to $n = 1$, the second mode corresponds to $n = 2$ and so forth. The above relationship

18

is only true for angles less than critical with respect to horizontal. The steeper angles, greater than critical, will have most of their energy refracted into the bottom and will very quickly be dissipated. The net contribution over many bottom surface interactions will negligible over long ranges.

2.1.2 Reflection of a Plane Wave Incident on a Boundary

The wave equation for a simple harmonic wave incident on a plane boundary between two fluids each with its own velocity and density is

$$\frac{\partial^2 \psi}{\partial t^2} = c^2 \frac{\partial \psi}{\partial r^2} \qquad 2-36$$

The simple harmonic solution for a ray propagating in the r direction is

$$\psi = A e^{i(\omega t - kr + \eta)} \qquad 2-37$$

If z is normal to r, this becomes

$$\psi = A e^{i(\omega t - kx\cos\theta - ky\sin\theta + \eta)}$$

$$\psi = A e^{i(\omega t - ax - by + \eta)} \qquad 2-38$$

where

$$a = k\cos\theta$$

$$b = k\sin\theta \qquad 2-39$$

a and b are the x and y components of the velocity of propagation in the x and y direction. Equation 2-38 can be

rewritten as

$$\psi = A e^{\left\{i\left[\omega\left(t-\frac{x}{Va}-\frac{y}{Vb}\right)+\eta\right]\right\}}$$ 2-40

where

$$Va = \frac{c}{\cos\theta} \qquad Vb = \frac{c}{\sin\theta}$$ 2-41

If the plane wave impinges on a boundary, some energy would be lost into the bottom due to partial refraction and some energy would be reflected back into the ocean. The amount of energy refracted and reflected depends on the incident angle, the density, and the velocity differences of the relative media:

$$\psi_{in} = A e^{i(\omega_{in}t+a_{in}+b_{in}y)}$$

$$\psi_{re} = B e^{i(\omega_{re}t-a_{re}x+b_{re}y)}$$ 2-42

and $$\psi_2 = C e^{i(\omega_2 t+a_2+b_2 y)}$$

where "in" represents the incident plane wave and "re" represents the reflected plane wave. Since the boundary conditions must be met at the interface, this requires the first boundary condition to maintain the continuity of pressure at the interface, while the second boundary condition requires the continuity of vertical particle velocity at the interface. In terms of the velocity potential and pressure from equation 2-12 and the prescribed boundary conditions, this gives

20

$$\frac{\partial \psi_1}{\partial x} = \frac{\partial \psi_2}{\partial x}$$

and $\qquad\qquad\qquad\qquad\qquad\qquad\qquad\qquad at\, x = 0 \qquad 2\text{-}43$

$$\rho_1 \frac{\partial \psi_1}{\partial t} = \rho_2 \frac{\partial \psi_2}{\partial t}$$

It follows that

$$\omega_{in} = \omega_{re} = \omega_2 = \omega$$

$$b_{in} = b_{re} = b_2 = b \qquad\qquad\qquad 2\text{-}44$$

$$\sin\theta_{in} = \sin\theta_{re} = \sin\theta_1$$

and $\qquad\qquad\qquad \dfrac{\sin\theta_1}{c_1} = \dfrac{\sin\theta_2}{c_2}$

These equations demonstrate that the frequency is unchanged by the boundary. These equations also demonstrate Snell's law, which states that the angle of the incident ray equals the angle of the reflected ray. The coefficients a_1 and a_2 become

$$a_1 = a_{in} = a_{re} = \frac{\omega}{c_1}\cos\theta = k_1\cos\theta = \sqrt{1 - \sin^2\theta_1} \qquad 2\text{-}45$$

$$a_2 = \frac{\omega}{c_2}\cos\theta_2 = k_2\cos\theta_2 = k_1\sin\theta_1\cot\theta_2 = \sqrt{\frac{c_1^2}{c_2^2} - \sin^2\theta_1}$$

The solutions become

$$\psi_{in} = Ae^{i(\omega t + a_1 x + by)} = Ae^{i\omega\left[t + \frac{(x\cos\theta_1 + y\sin\theta_1)}{c_1}\right]}$$

$$\psi_{re} = Be^{i(\omega t - a_1 x + by)} = Be^{i\omega\left[t + \frac{(-x\cos\theta_1 + y\sin\theta_1)}{c_1}\right]} \qquad 2\text{-}46$$

$$\psi_2 = Ce^{i(\omega t + a_2 x + by)} = Ce^{i\omega\left[t + \frac{(x\cos\theta_2 + y\sin\theta_2)}{c_2}\right]}$$

By substituting the above equations into the boundary conditions in equation 2-43, we obtain an expression for the relative amplitude of the incident to reflected wave:

$$a_1(A-B) = a_2 c$$

$$\rho_1(A+B) = \rho_2 c \qquad\qquad 2\text{-}47$$

Substituting and re-arranging terms gives us

$$\frac{B}{A} = \frac{a_1\rho_2 - a_2\rho_1}{a_1\rho_2 + a_2\rho_1}$$

and
$$\frac{C}{A} = \frac{2a_1\rho_1}{a_1\rho_2 + a_2\rho_1} \qquad\qquad 2\text{-}48$$

Substituting a_1 and a_2 from equation 2-45 obtains

$$\frac{B}{A} = \frac{\rho_2\cot\theta_1 - \rho_1\cot\theta_2}{\rho_2\cot\theta_1 + \rho_1\cot\theta_2}$$

and
$$\frac{C}{A} = \frac{2\rho_1\cot\theta_1}{\rho_2\theta_1 + \rho_1\cot\theta_2} \qquad\qquad 2\text{-}49$$

If we rewrite equation 2-45 in terms of the velocities and densities of medium 1 and 2, we will get the Rayleigh reflection coefficient

$$\frac{B}{A} = \frac{\dfrac{\rho_2}{\rho_1} - \dfrac{\sqrt{\left(\dfrac{c_1^2}{c_2^2}\right) - \sin^2\theta_1}}{\sqrt{1 - \sin^2\theta_1}}}{\dfrac{\rho_2}{\rho_1} + \dfrac{\sqrt{\left(\dfrac{c_1^2}{c_2^2}\right) - \sin^2\theta_1}}{\sqrt{1 - \sin^2\theta_1}}} \qquad\qquad 2\text{-}50$$

and
$$\frac{C}{A} = \frac{2}{\dfrac{\rho_2}{\rho_1} + \dfrac{\sqrt{\left(\dfrac{c_1^2}{c_2^2}\right) - \sin^2\theta_1}}{\sqrt{1 - \sin^2\theta_1}}} \qquad\qquad 2\text{-}51$$

If the angle theta equals zero-normal incidence, then the above equations will reduce to

$$\frac{B}{A} = \frac{\rho_2 c_2 - \rho_1 c_1}{\rho_2 c_2 + \rho_1 c_1} \qquad \text{2-52}$$

$$\frac{C}{A} = \frac{2\rho_1 c_1}{\rho_2 c_2 + \rho_1 c_1}$$

If we define the acoustic impedance as

$$Z_1 = \frac{\rho_1 c_1}{\cos\theta_1} \quad , \quad Z_2 = \frac{\rho_2 c_2}{\cos\theta_2} \qquad \text{2-53}$$

then we can rewrite equation 2-52 as the reflection coefficient

$$Z_R = \frac{Z_2 - Z_1}{Z_2 + Z_1} \qquad \text{2-54}$$

which describes the Rayleigh reflection coefficient as the ratio of the acoustic impedance in each medium.

2.1.3 Boundary Impedance

Brekhovskikh (1980) describes the physical and mathematical significances of the boundary impedance involved with such a problem description. The sound field can be characterized by the velocity potential defined by equation 2-20. The particle velocity and acoustic pressure can be expressed using the relationships from equation 2-12, where

$$v = -grad(\Psi) \quad \text{and} \quad p = -i\omega\rho\Psi \qquad \text{2-55}$$

The particle velocity can be expressed as

23

$$v = -\frac{i}{\omega\rho}grad(p) = \frac{k\,p}{\omega\rho} \qquad k = \frac{\omega}{c} \qquad \qquad 2\text{-}56$$

Substituting $k = \frac{\omega}{c}$, we obtain, for the normal component of the velocity

$$v_n = \frac{p}{\rho c}\cos\theta \quad \text{or} \quad \frac{p}{v_n} = \frac{\rho c}{\cos\theta} \qquad 2\text{-}57$$

This demonstrates that the acoustic impedance is the ratio of the acoustic pressure to the normal component of the particle velocity of a plane wave propagating in the positive z direction. The above relationship will be used in determininig the driving point impedance of the ocean bottom. The pressure gradient is used to derive the particle velocity, and the pressure at the boundary (bottom) can be measured directly. The ratio of these quantities, as previously stated, can be used to determine the impedance acoustically.

2.1.4 Numerical Methods of Comparison, SAFARI

The theoretical solution of the wave equation, which incorporates many experimental variables such as compressional wavespeed versus depth and shear wave speed versus depth in the sediment, is complex and generally unattainable. For this reason, it is necessary to use a numerical method to obtain a solution.

The numerical method chosen was the computer model

24

called SAFARI. The SAFARI model was chosen for the follow-
ing reasons. First, the SAFARI model is a shallow water
model and the Hudson Canyon Experiment was performed on the
New Jersey continental shelf in a water depth of 73 meters.
Second, SAFARI is able to incorporate a layered sediment
model rather than a single valued bottom type. Since the
problem of predicting propagation in shallow water may be
due to thinly covered and layered sediments, the SAFARI
model is capable of more accurately matching the real envi-
ronmental conditions. Thirdly, SAFARI can incorporate val-
ues of shear in the sediment, which requires the bottom to
be treated as a solid rather than a liquid. Some
researchers believe that shear has an important role to
play in the propagation of sound through shallow water
environments. Lastly, the SAFARI model predictions are
derived from an exact solution to the wave equation. This
contrasts with other models which approximate the solution
to the wave equation for their results.

A general explanation of SAFARI is presented in this
section. In summarizing the process by which SAFARI calcu-
lates the field, many details will be omitted. Additional
information can be obtained through the SAFARI users guide
(Schmidt 1988). The principle of wave equation separation
for a horizontally stratified medium is a solution tech-
nique for many theoretical models. The SAFARI model
requires the wave equation separation and utilizes the Fast
Field (FFP) or the full wavefield technique (DiNapoli and

Deavenport 1980) for an exact solution to the wave equation. The model can treat the medium as a solid or liquid stratified environment. The computation of the depth-dependent Green's function is performed for many wavenumbers simultaneously using a global matrix approach. The sound field produced by multiple sources in each layer is solved by superposition of the field described by a homogeneous wave equation. The boundary conditions are introduced and solved at each interface simultaneously. These local solutions then form a linear system of equations which can be represented by Hankel transforms. These Hankel transforms can then be approximated using Fast Fourier Transform (FFT) algorithms. This provides a relatively quick method of solving the exact wave equation for the wavefield.

3 Description of Experiment

An experiment was designed in a surveyed area where the geophysical properties had been established from previous surveys. The acoustic experimental results were compared to predictions using a theoretical computer model and the previously obtained sediment properties. The comparisons were made to ascertain the validity of the geophysical and geo-acoustical parameters needed to correctly predict a specific sound field.

The purpose of this study was to investigate a technique to determine one of these bottom properties, the boundary impedance, acoustically. The data for this study were collected as a part of a larger experiment to obtain acoustic data to determine transmission loss and synthetic aperture wavenumber spectra. Although the results of the transmission loss and wavenumber spectra are not a necessary part of the boundary impedance study, an investigation of these results was performed to provide supportive information with regard to understanding the characteristics of modal propagation in the experimental results. For this reason, the results of these measurements will be presented in this paper.

3.1 Description of Measurement Area Overview

The Hudson Canyon experiment was conducted on the continental shelf off the New Jersey coast in the vicinity of the AMCOR 6010 borehole. A map of the experimental area is shown in Figure 3-1. The site provided a constant water depth as well as a gradually changing water depth along fixed bearing radials. A prime reason for this site selection was that the area around the AMCOR 6010 borehole was the site of numerous measurements by the Office of Naval Research (ONR). The U.S. Geologic`'` Survey performed an extensive study of morphology and shallow seismic character during the 1970's. Milliman and Ewing et al. (1989) have better examined the geology of the New Jersey outer shelf by combining the interpretation of Huntec Deep Towed seismic profiles taken by the Woods Hole Oceanographic Institute, and a re-interpretation of the USGS data. This area was also the site of a series of experiments conducted by the Geo-Acoustics Laboratory of the University of Miami to determine the geophysical properties of the sediment. The most recent survey was performed just prior to the Hudson Canyon Experiment to produce values of the shear and compressional wavespeeds and the attenuation in the sediment.

A 24 element hydrophone array was anchored in the experimental area using an acoustic release anchor and a sub-surface buoy to hold the array vertical. A spar buoy was tethered to the sub-surface buoy and fitted with a
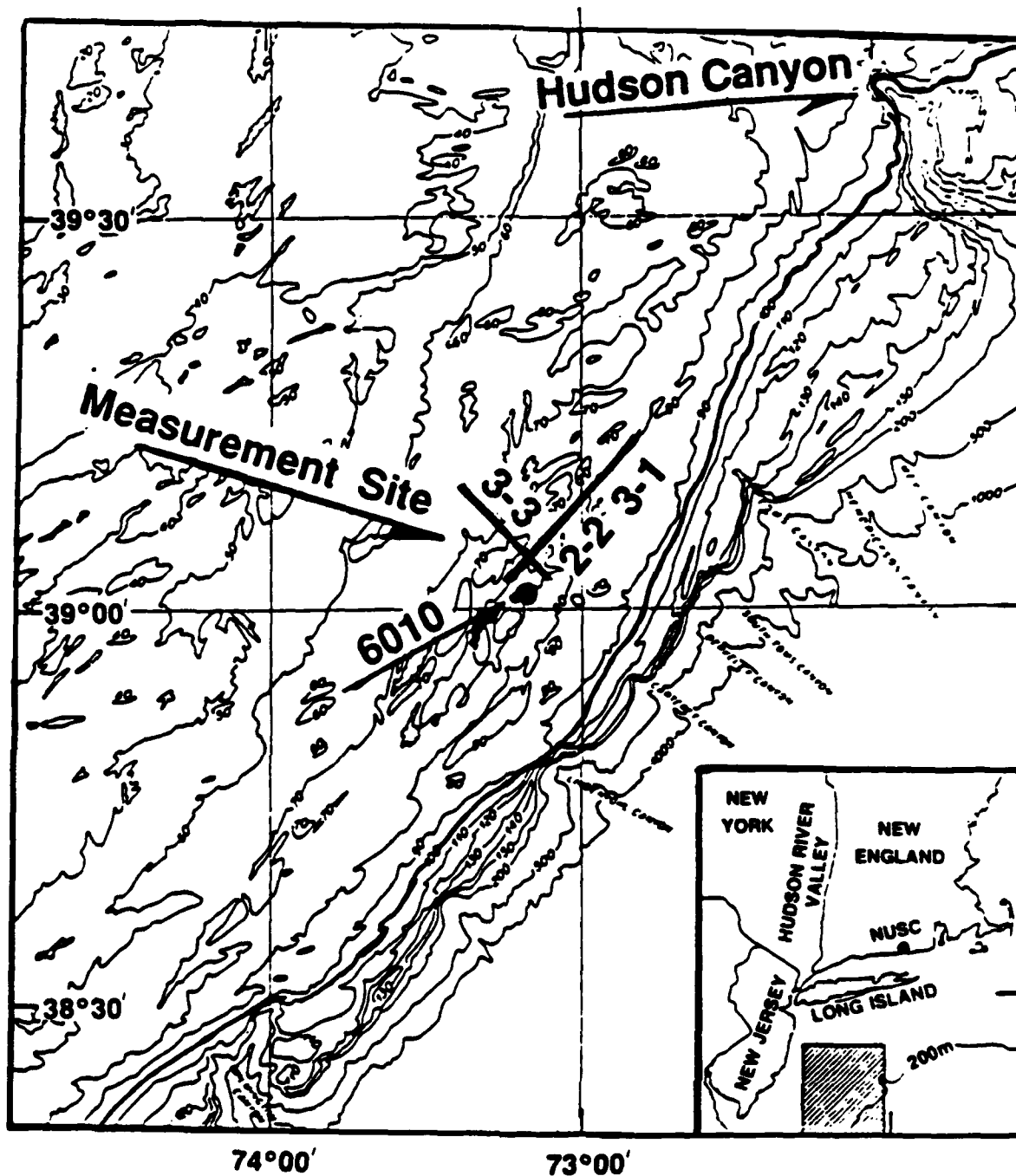
Figure 3-1 Map of Experimental Area

radar transponder to determine range. The array consisted of Benthos AQ-17 hydrophones, which had a calibrated sensitivity of -174 dB//1V spaced at 2.5 meters. Hydrophone 24 was positioned on the ocean floor. Figure 3-2 shows the experimental test set-up. The NUSC Ranger towed a calibrated NRL J15-3A acoustic source along constant water depth and varying depth radials at speeds between 1 and 5 knots over ranges of 4 and 26 kilometers.

Measurements of transmission loss versus range for ranges to 26 kilometers were obtained for eight frequencies: 50, 75, 175, 275, 375, 425, 525, and 600 Hz. At these same frequencies, the source was towed at slow speeds (1-2 knots) with radar ranging to produce data suitable for synthetic aperture processing. The measured signal versus time was Fourier transformed to yield complex pressure versus time. These data were merged to yield complex pressure versus range. The data were processed using the Hankel transform technique of Frisk and Lynch (1984) to determine the eigenvalues (wavenumbers) of the propagating modes. The propagating modes depend on the bottom impedance. The sound source transmitted low frequencies of 10, 15, 20, 25, 30, 35, 40, 50, and 55 Hz for the collection of data with the vertical array of hydrophones to determine boundary impedance. The impedance of the bottom can be derived from the normal component of the pressure gradient for frequencies shown to propagate in a single mode.
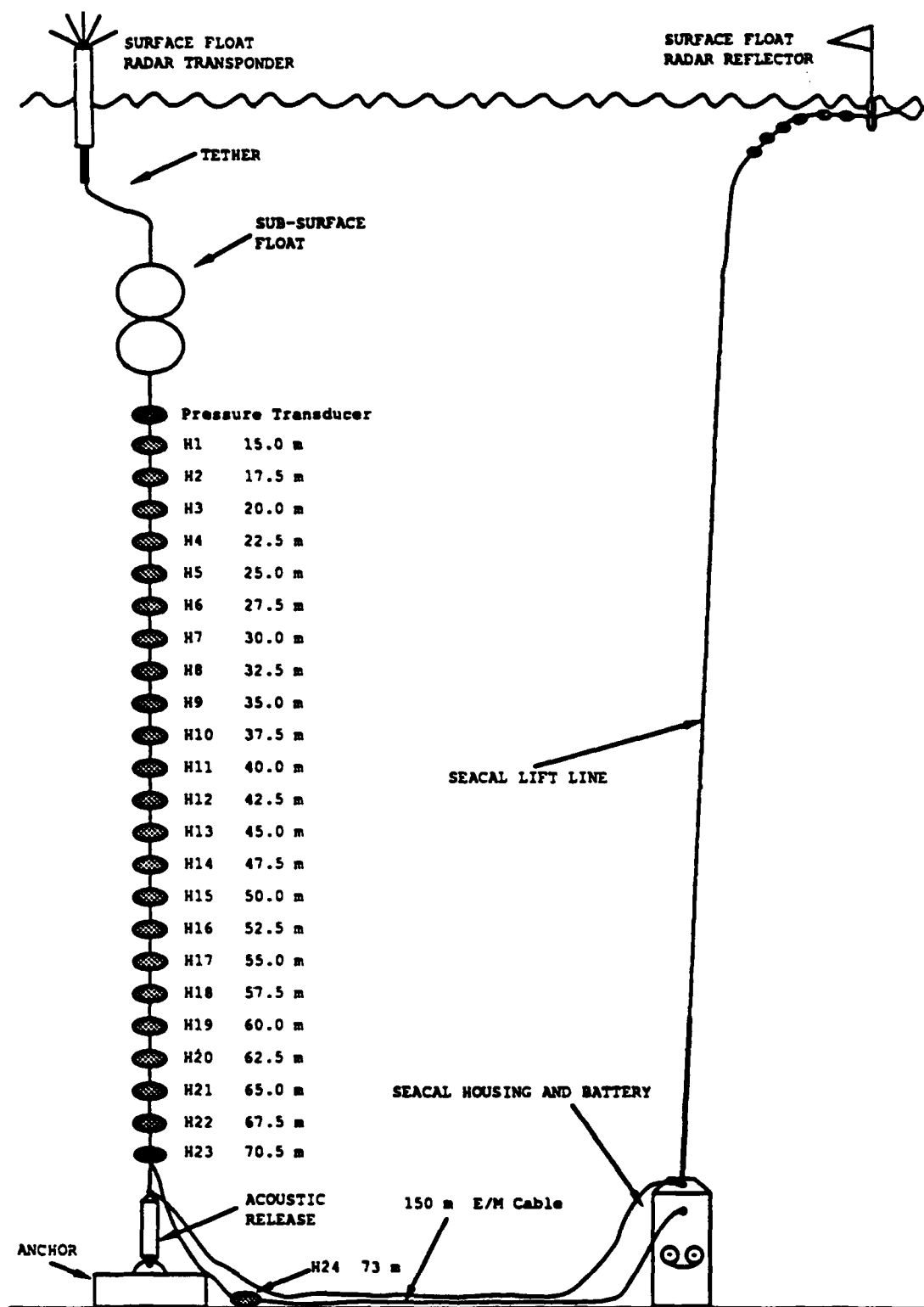
Figure 3-2 Experimental Test Set-up

31

3.1.1 Geophysical Description of Area

In shallow water, it is imperative to understand the effects of the physical properties of the sea-bed to correctly calculate wave propagation. The Hudson Canyon experimental site was chosen because it fulfilled two experimental criteria: (1) the area had constant water depth over a selected range, and (2) it was located in a highly surveyed area. Constant bathymetry (water depth) was needed to minimize the effects of water depth variations on modal propagation. Thus, theoretical comparisons could be made using the surveyed physical and acoustical properties of the sea-bed.

A suitable location for the experiment was on the continental shelf off the New Jersey coast in the vicinity of the Atlantic Margin Core (AMCOR) 6010 borehole, which was the site of extensive ONR measurements. This particular site had been the subject of many studies, and the resultant geo-acoustical parameters (compressional and shear wavespeeds) were believed to be known.

3.1.1.1 Seismic Data

High resolution seismic profiles of the sediment interface were available from the U.S. Geological Survey (USGS) and from the Huntec Deep Towed Seismic (DTS) boomer profiles. The USGS effort included site surveys as well as

regional surveys in 1975. High resolution data were collected using a seismic profiler. Coarse resolution data were collected using the seismic profiler together with a 3.5 kHz echosounder. The USGS data was reinterpreted by Milliman and Ewing (1989) and combined with the Huntec survey data collected in the same area.

The Huntec DTS system is a deep towed seismic boomer. A single hydrophone mounted within the boomer collects high resolution data (1/2 to 1 meter). A six element hydrophone array is used for deeper penetration into the sediment but with less resolution (2.5 meters). The DTS system is pitch and heave compensated to offset the sea-surface effects. Frequencies transmitted for data reception were between 1000-2500 Hz.

The Huntec DTS boomer profiles collected on the New Jersey shelf map well with the existing USGS data. The compiled data describe the sediment thickness in the area. A fairly constant sediment thickness was found for the direction of the constant depth radial runs. However, for the varying depth runs, the sediment layer decreases in the landward direction.

3.1.1.2 Sediment Properties

The AMCOR 6010 borehole provided sedimentological reference data derived from the samples taken in 1976 for comparison with several experiments done by T. Yamamoto of

University of Miami. Ocean Bottom Seismic (OBS) and pressure measurements were made in the vicinity of the AMCOR 6010 borehole site by the University of Miami during several recent experiments (1986, 1987, 1989). The most recent experiment occurred in July 1989, just prior to the Hudson Canyon Experiment. These studies provided estimates of porosity, shear and compressional wavespeed, and attenuation.

The Bottom Shear Modulus Profiler (BSMP) system makes real-time measurements of the small amplitude, low frequency (0.001 to 1.0 Hz) sea-bed motions induced by water waves and sea-bed microseisms. The seismometers measure acceleration along the principal axes (vertical, radial, and transverse), recording continuously along with the pressure. Spectral analysis of the data yields results suitable for a geophysical inversion technique to extract the elastic shear modulus versus depth (Yamamoto and Torii 1986, Trevorrow et al. 1988). Other parameters (such as porosity, bulk density, compressional and shear wave velocity, and attenuation versus depth) can be estimated from the shear modulus profile using well known empirical and theoretical stress, strain relations. Figure 3-3 a-d shows the estimated geo-acoustical parameters compiled by T. Yamamoto of the University of Miami for the experimental area. These data were used as input for the theoretical models for predictions of transmission loss, wavenumber, and the pressure field.
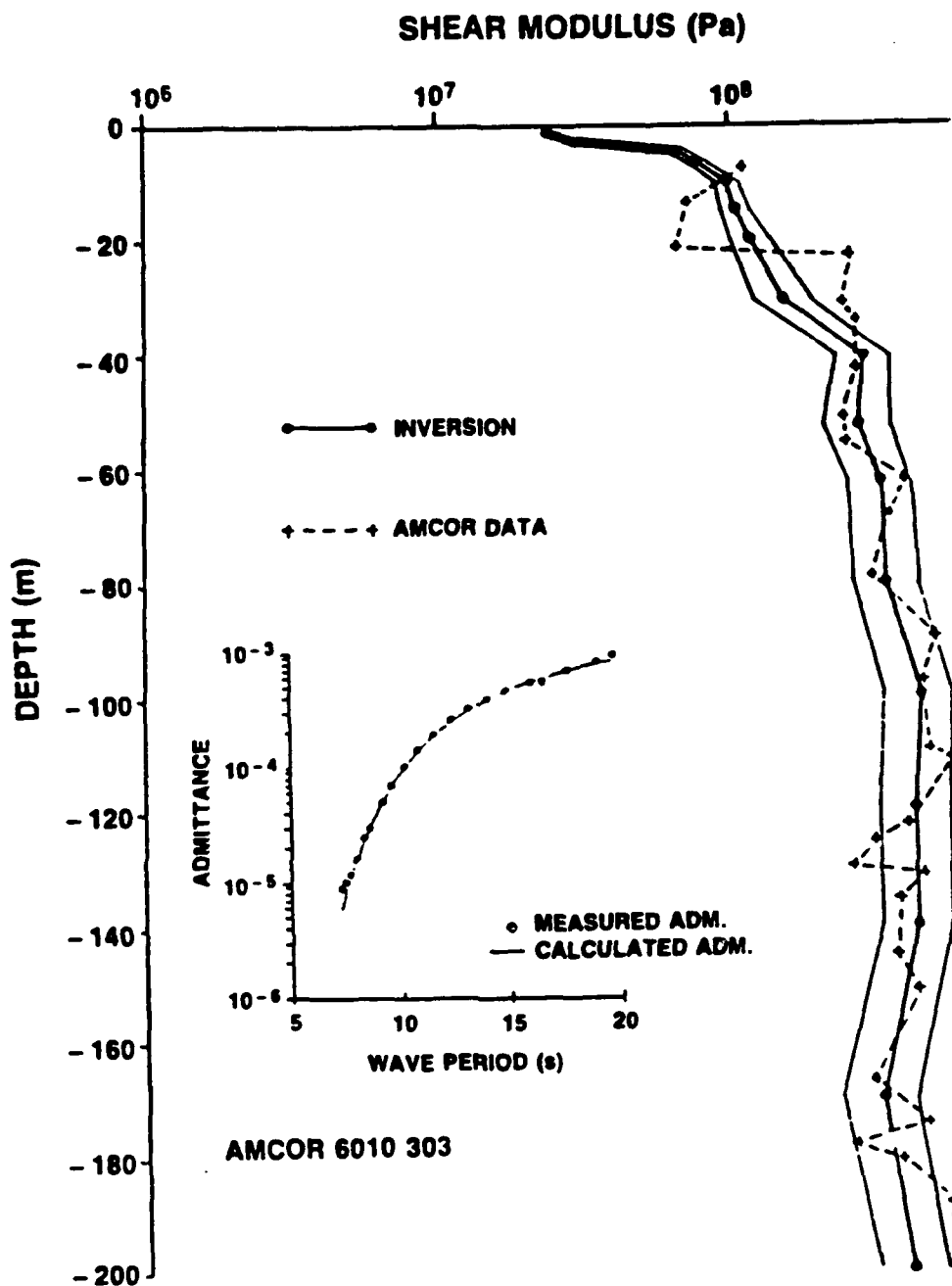
SHEAR MODULUS (Pa)

Figure 3-3 Geo-acoustic Estimates of AMCOR 6010 Borehole
Site a. Shear Modulus versus Depth

Reprinted from Trevorrow et al., "Summary of Ocean Bottom
Seismic Pressure Measurements taken in July 1988 on the
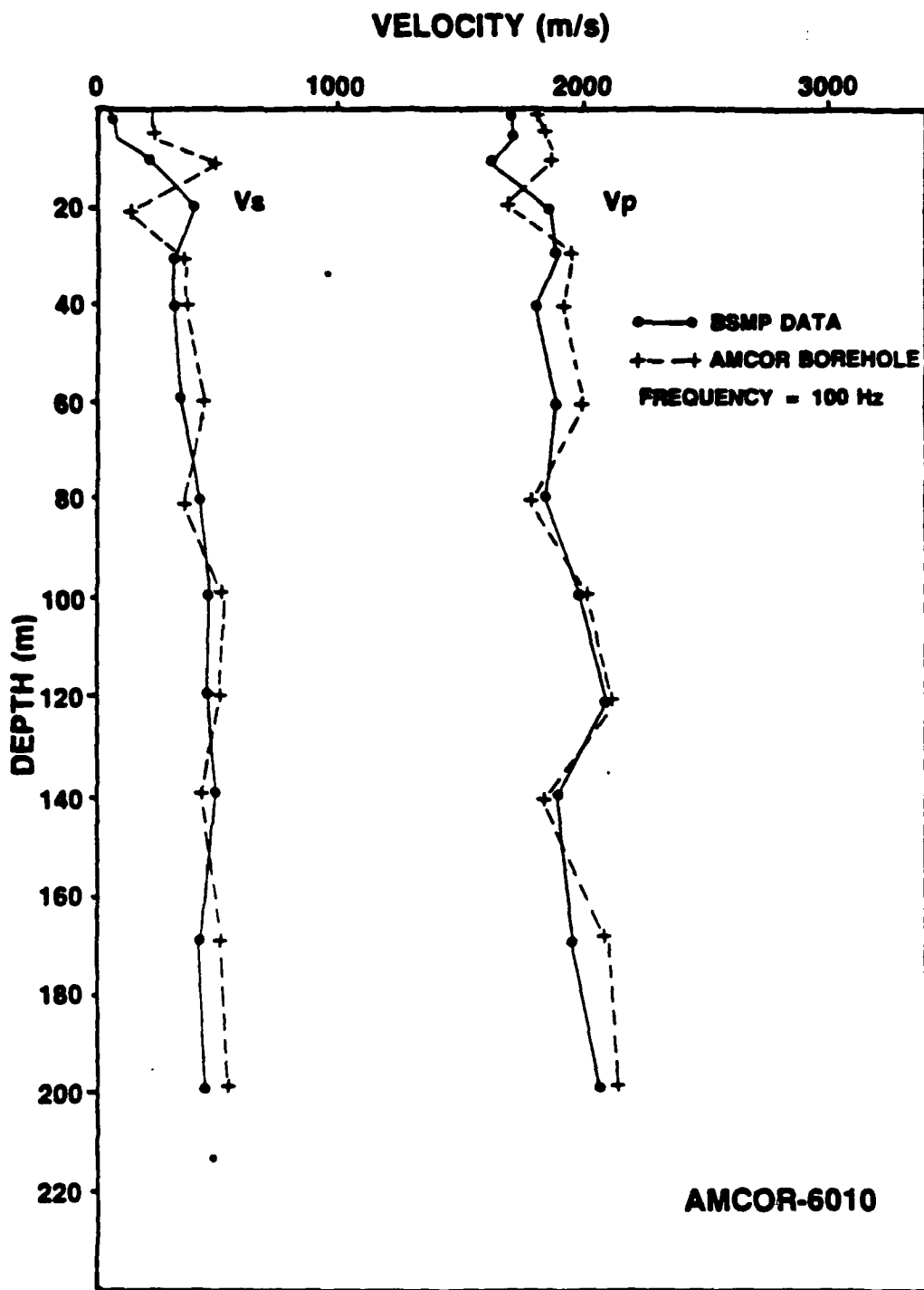New Jersey Shelf and Georges Bank," 1988
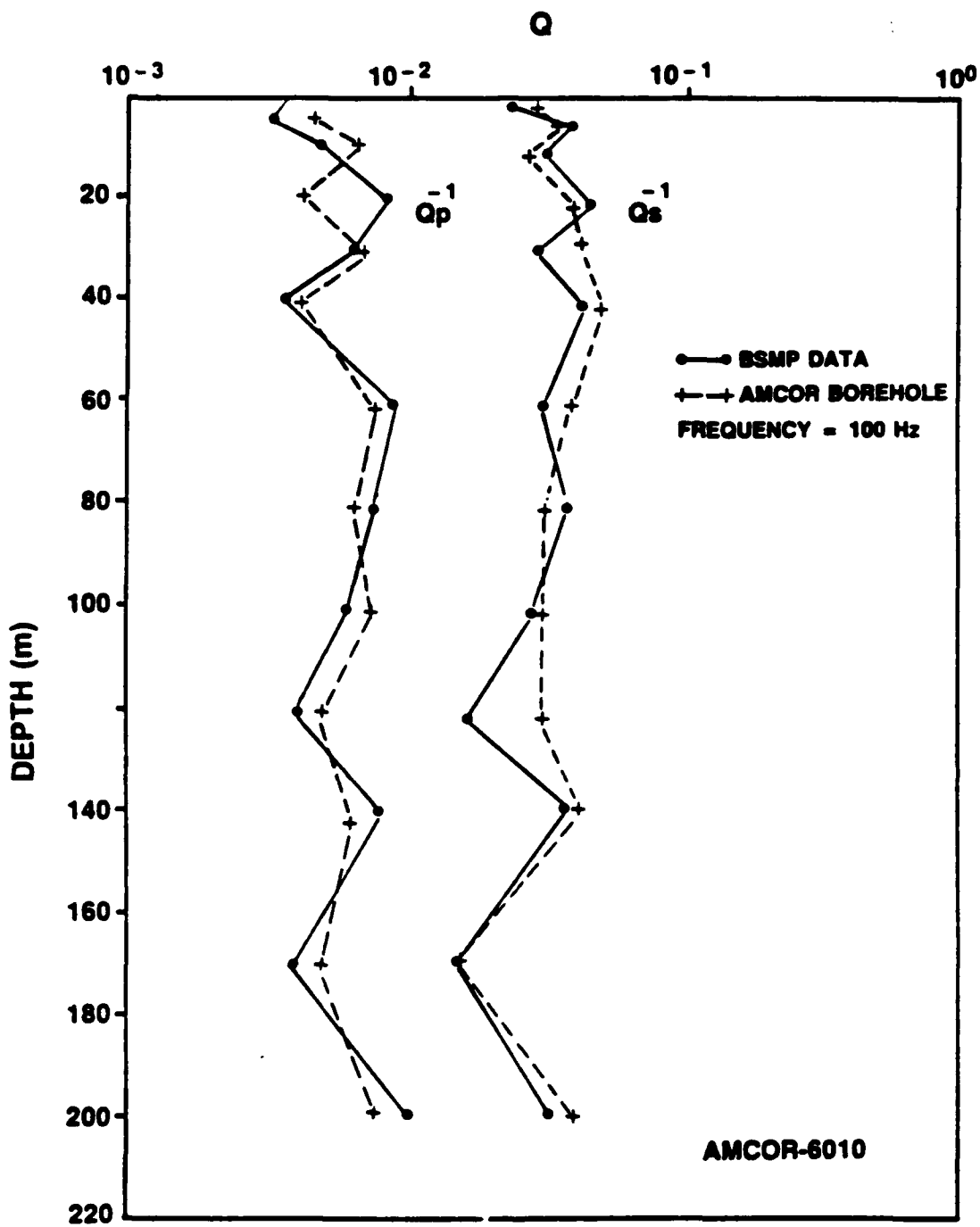
35

Figure 3-3 (cont'd) b. Velocity versus Depth
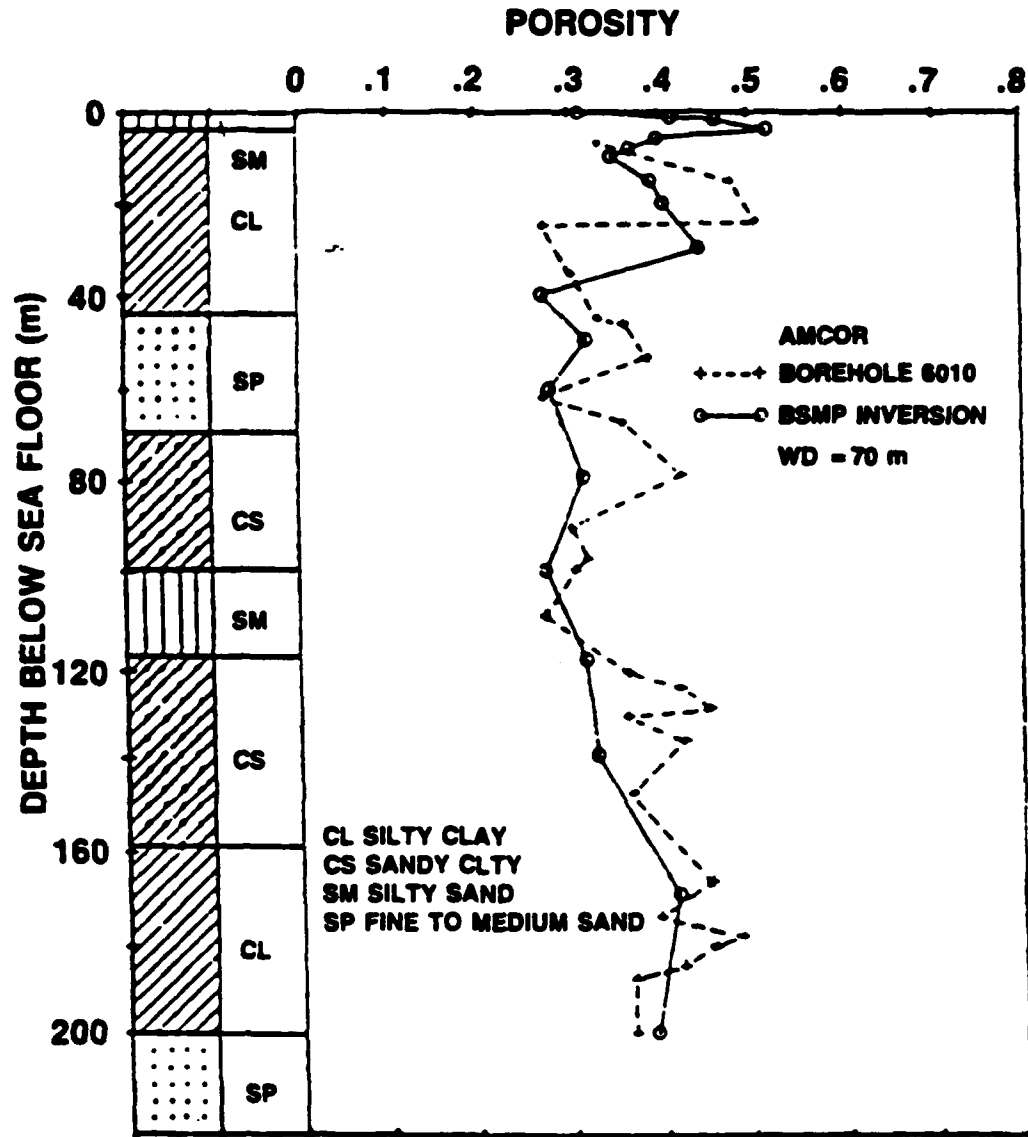
Figure 3-3 (cont'd)   c. Q versus Depth

Figure 3-3 (cont'd) d. Porosity versus Depth

38

3.1.2 Geo-acoustical Parameters

The physical characteristics of the water, such as the sonic velocity and water depth, must be known to correctly determine propagation in the waveguide. A continuous measure of the compressional wavespeed throughout the experiment is necessary as the eigenvalues are affected by changes in sound velocity. Also of importance is the water depth. This parameter controls which modes will propagate or which modes will "fit" in the height of the waveguide.

3.1.2.1 Oceanographic Profiles

Two oceanographic measurement systems were used during the experiment: an Applied Microsystems Sound Velocity Profiler (SVP-16) and a SEABIRD Conductivity Temperature and Depth (CTD) system. The SVP-16 system measures the sound velocity directly. This method is a contrast to the CTD system, which calculates sound velocity using Wilson's equation and measurements of conductivity, temperature, and depth. It was difficult to deploy the measurement system while the ship was underway, which resulted in sparse sampling of the sound speed profiles. Figure 3-4 a-c shows the SVP and CTD velocity profiles for runs TL3-1 (uniform depth), TL2-2 (synthetic aperture), and TL3-3 (varying depth). The profiles exhibit similar characteristics and can be broken up into three basic regions: a mixed layer
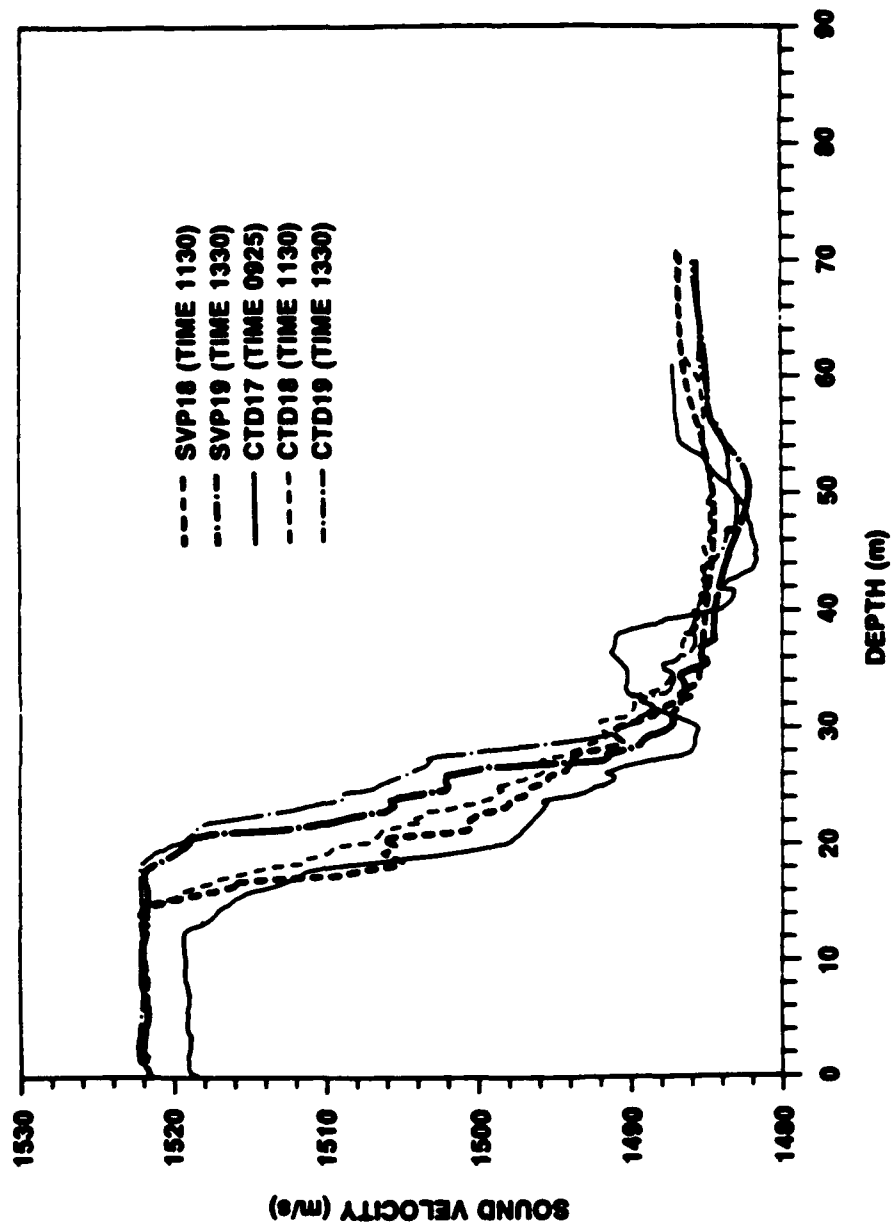
Figure 3-4 Experimental SVP/CTD Velocity Profiles
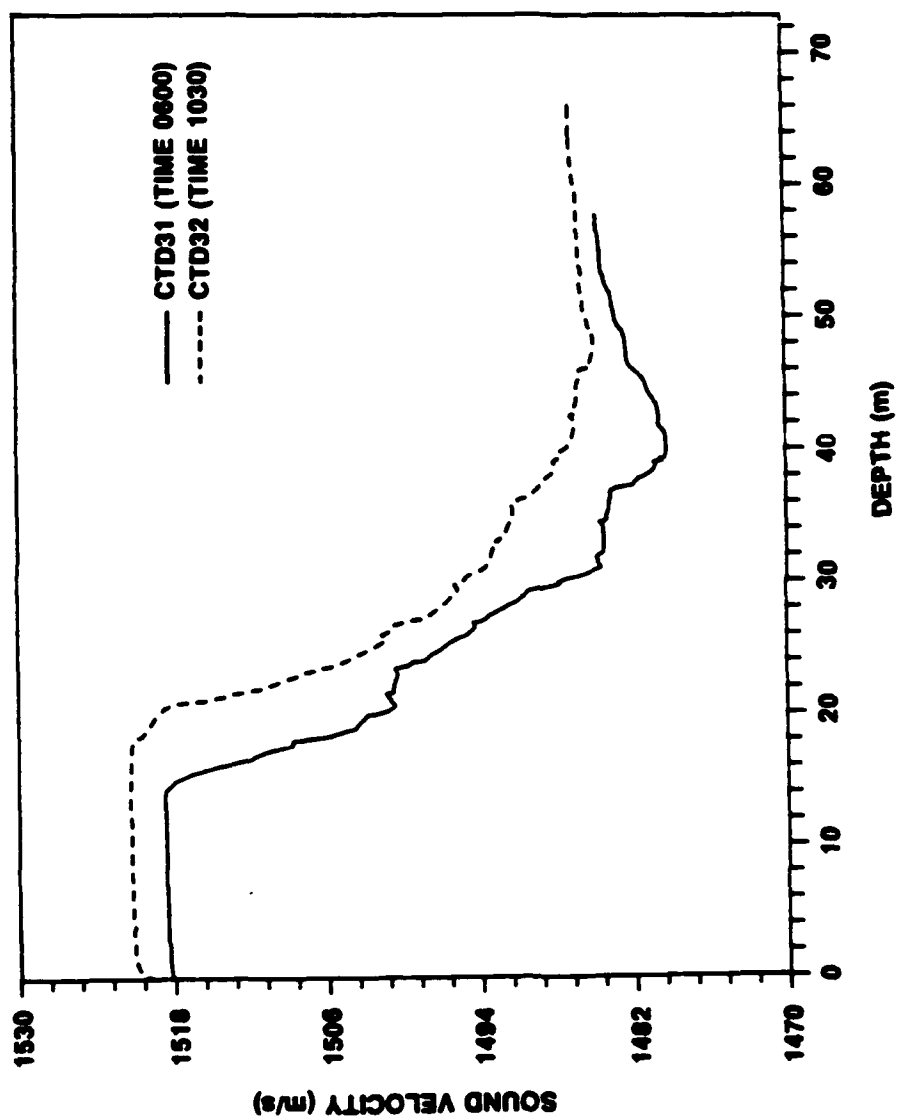a. Sound Velocity versus Depth, Run TL3-1

40

Figure 3-4 (cont'd) c. Sound Velocity versus Depth, Run TL3-3
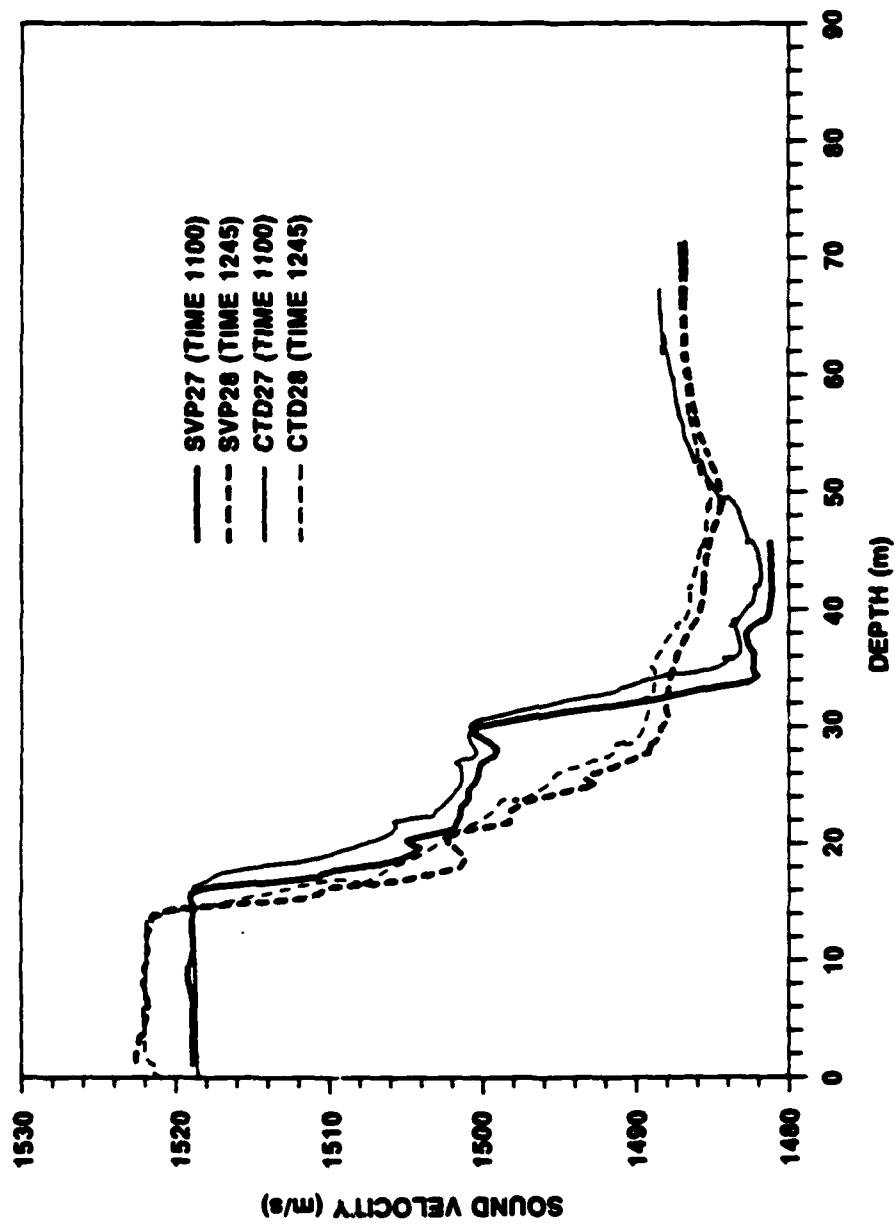
Figure 3-4 (cont'd) b. Sound Velocity versus Depth, Run TL2-2

42

where the sound velocity is fairly constant versus depth, a
thermocline layer in which the sound velocity changes rap-
idly as a function of depth, and a deep layer where the
sound velocity is constant or varies slowly with increasing
depth. The profiles are changing both temporally and spa-
tially according to the measurement range, as illustrated
in Figure 3-4. The mixed layer sound velocity changes from
1518 m/s to 1522 m/s. The depth of the thermocline layer
varies from 14 m to 18 m. An important parameter influenc-
ing the received wavefield is the position of the source in
the water column. For this reason the variability of the
sound velocity must be considered. At the 61 m depth the
sound velocity varies between 1486 m/s to 1489 m/s. At the
shallower source depth 54.6 m the sound velocity changes
between 1483 m/s and 1488 m/s. An average or mean sound
velocity of 1496 m/s was calculated for the velocity pro-
file shown in Figure 3-4 b.

3.1.2.2 Bathymetry Data

Shallow water propagation is highly dependent on the
height of the waveguide as shown in Section 2. The Hudson
Canyon Experiment was performed for two basic cases: a uni-
form depth case and a varying depth case. A good estimate
of the water depth was obtained using a UQN-15 fathometer
located on the bridge. The data were recorded continuously
on a strip chart recorder. This measurement was cross

checked periodically with the redundant measurement of the ship's fathometer. Bathymetry data taken with the UQN-15 fathometer for the experimental runs are included in Figures 3-5 a,b. The data were corrected for the average experimental sonic velocity and the transducer position on the keel. The uniform depth shown has a mean value of 72.08 m and is bounded by 70 m and 74.7 m. The sloping depth case has a mean value of 64.6 m and has a maximum depth of 74.7 m and minimum depth of 55 m.
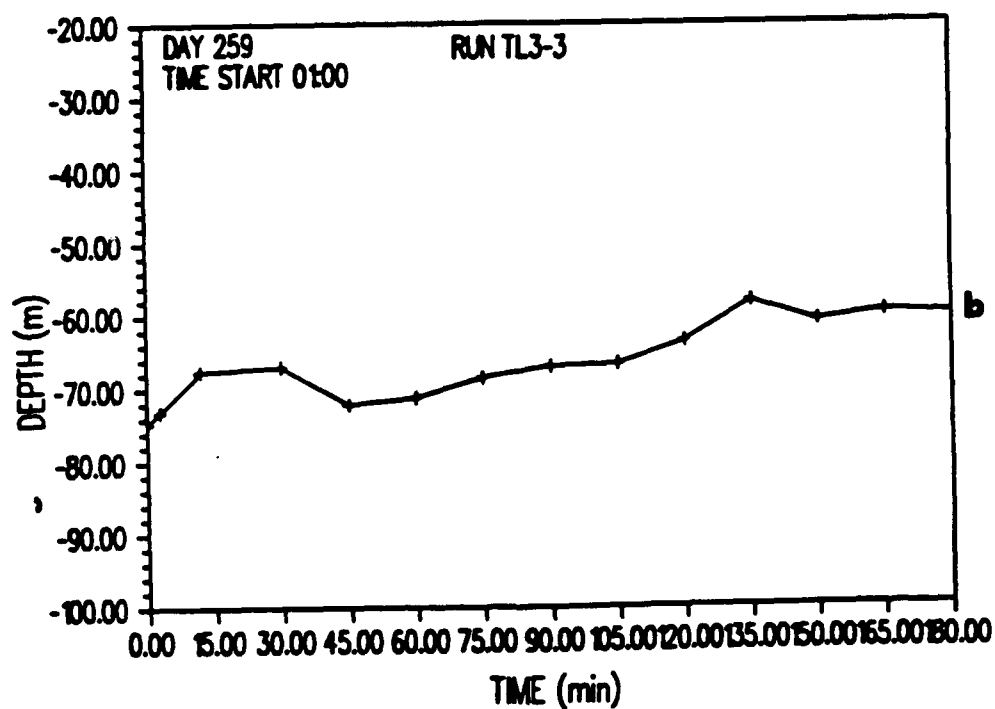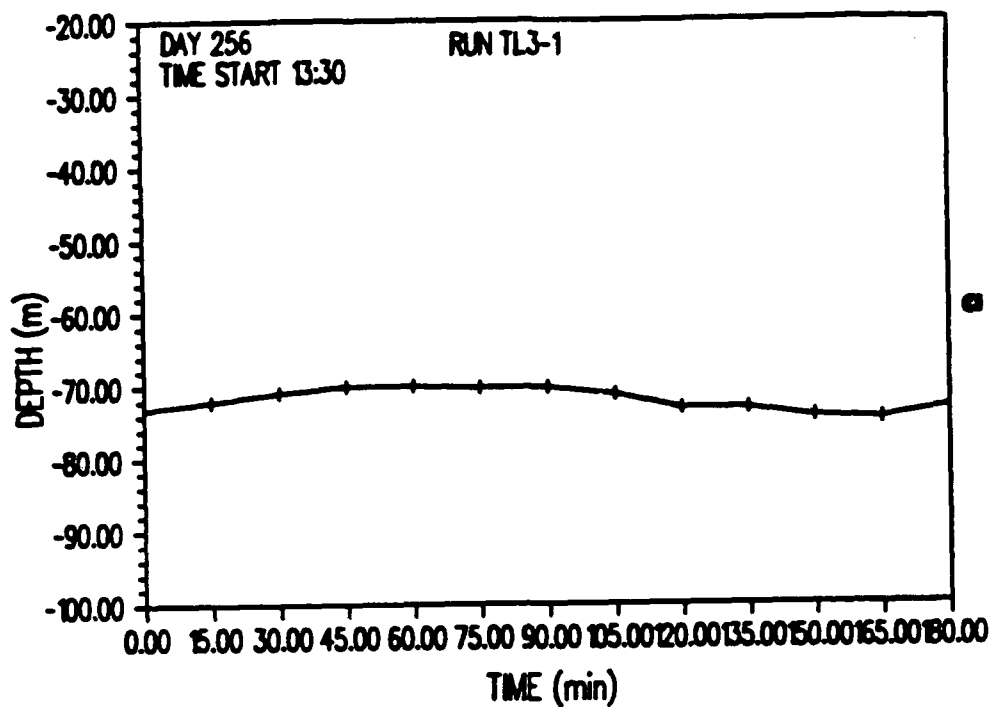
Figure 3-5 Measurement Area Bathymetry
a. Run TL3-1 , b. Run TL3-3

3.2 Experimental Measurement Systems

An electrodynamic transducer, the NRL J15-3A, was used as the waveform projector for the experiment. The NRL J15-3A source was operated over the frequency range of 10 to 600 Hz at sound pressure levels of 155 to 175 dB//1uPa at 1 meter. The transducer was mounted in a tow body as shown in Figure 3-6. Also mounted in the tow body were an H-91 monitor hydrophone and a depth sensor. The H-91 hydrophone was positioned at a distance of 2 meters behind the acoustic center of the transducer for the purpose of monitoring source levels. The calibrated depth sensor output provided the position of the source in the water column as well as measured the length of the tow cable. The calibration of the NRL J15-3A and the H-91 hydrophone was performed at the NUSC Dodge Pond Facility (Parssinen, 1989).

Figure 3-7 shows a block diagram of the dry-lab data acquisition and monitoring system. This system was used to generate the waveforms, provide power to the sound source, and monitor the output. Waveforms were generated using a Analogic 2020 waveform generator. The four frequencies transmitted simultaneously were chosen to minimize the variation of source level with frequency. The waveform generator was controlled by an Austron master clock oscillator, which was accurate to 10^{-9} seconds. The output levels were adjusted using a Daven attenuator as well as a voltage

Fixed elevator 12"x22"x¼" both sides of rudder

fixed rudder

12"

42"

tow point

6" U channel

U chann

3

U chan 4"

J15-3 Source 29" Diameter

8½" d

6"

5"

6"

½"
2"

12½"
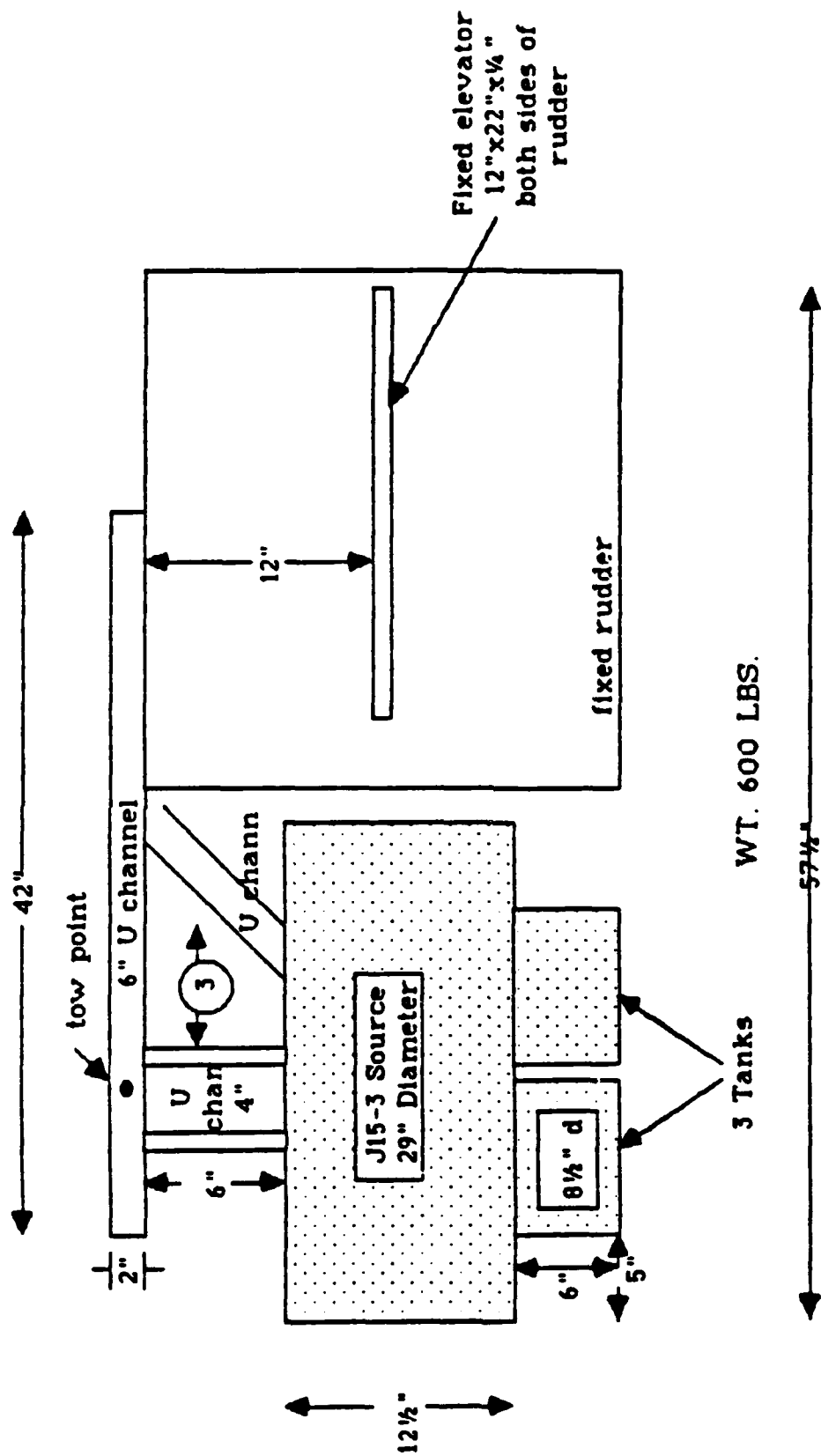
3 Tanks

WT. 600 LBS.

57½"
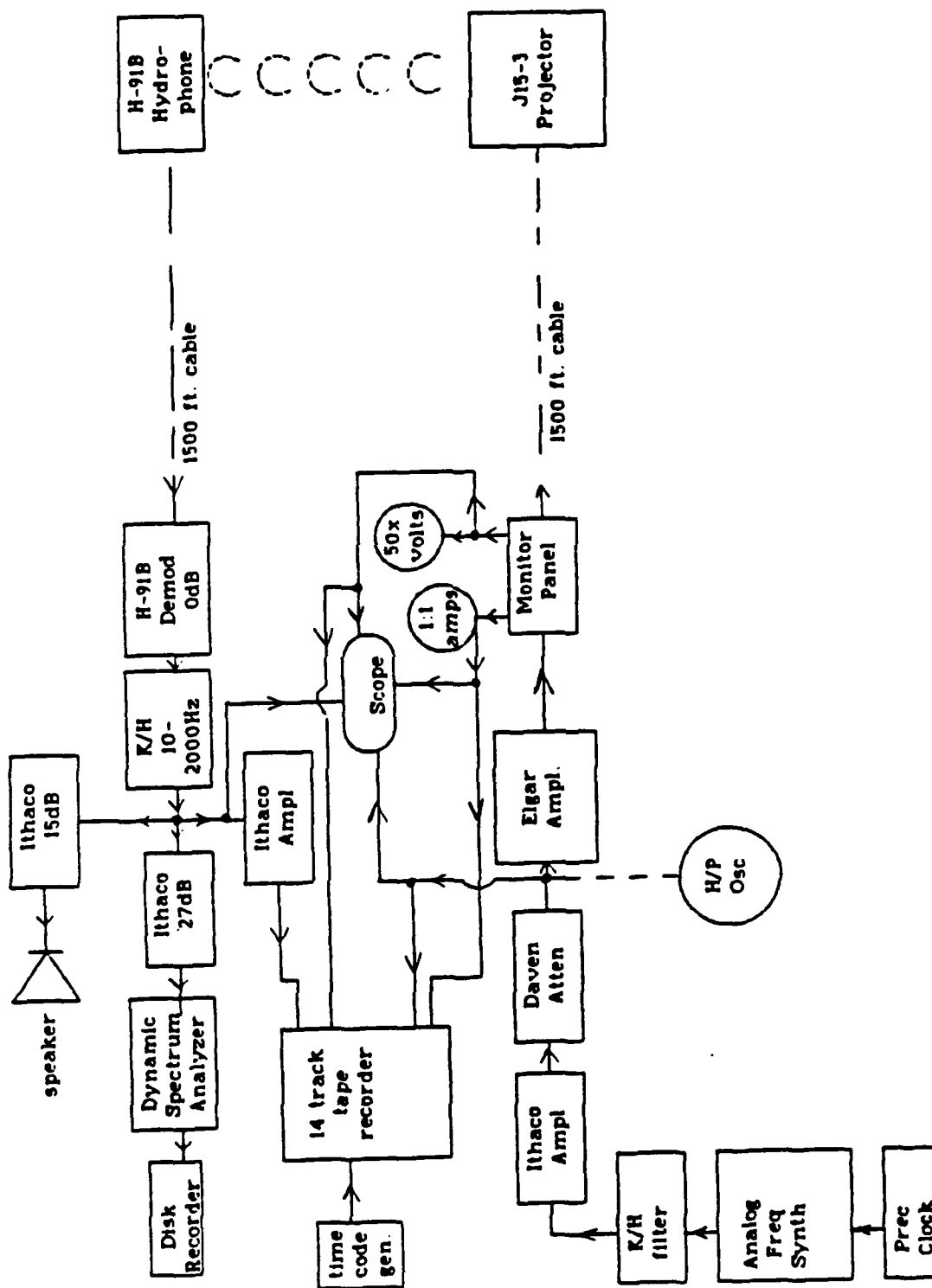
Figure 3-6 Sound Source J15-3A in Tow Body

Figure 3-7 Block Diagram of Data Acquisition System

and current monitor with a calibrated Ballantine RMS volt-
meter. The signal generator drove the Elgar power ampli-
fier. In order to maintain accurate and verifiable source
levels, the voltage and current outputs of the Elgar
amplifier were recorded and compared against calibrated
measurements of transmit current and voltage response
curves generated at Dodge Pond and the Orlando Reference
Detachment. A fourteen track analog tape recorder recorded
the output of the waveform generator, depth sensor, and
Elgar amplifier current and voltage. Data logs were kept
which periodically logged the outputs specified above.

Monitoring of the sound source was accomplished by the
use of the H-91 hydrophone. The output of the H-91 was band
pass filtered, amplified, and input into an HP-3362 spec-
trum analyzer from which averaged spectral levels were
recorded for each test. The H-91 output was also recorded
on analog tape recorder. All the above data were used to
determine the source levels for the experiment (Parssinen
1989). A separate self-contained measurement system was
used to collect the acoustic data

The acoustic data were recorded with the SEACAL data
acquisition system manufactured by C&M Technology. The
acquisition system consisted of a 24 element electro-
mechanical hydrophone array and 2 VCR cassette tape record-
ers housed within the instrumented pressure vessel (IPV).
The self-contained unit was able to record 4 hours (fast

speed) or 16 hours (slow speed) of acoustic data in a con-
tinuous mode or a sequence of pre-programmed ON/OFF times.

The 24 element array was anchored in the test area and
supported with a sub-surface flotation buoy. The IPV was
hard wired to the array using a length of cable approxi-
mately 150 m. This allowed the instrument housing to be
raised and the VCR cassettes to be changed without
disturbing the position of the hydrophone array.

The array shown in Figure 3-2 consisted of 24 Benthos
AQ-17 hydrophones with an approximate spacing of 2.5 m
between the elements. Hydrophone sensitivity was determined
to be -174 dB//1V/1uPa at the Dodge Pond calibration. The
array was positioned with an acoustic release anchor and a
sub-surface flotation buoy. A marker buoy with a Del Norte
radar transponder was tethered to the sub-surface buoy.
Another radar transponder was attached to the mast of the
NUSC Ranger. This radar ranging system was used to obtain
accurate range information.

The acoustic signal was received on the hydrophone
array and recorded with the SEACAL data acquisition system.
The SEACAL system electronics are shown in Figure 3-8. The
major components are the hydrophone signal conditioning
cards, the real time clock and controller, the depth sensor
interface, the system control panel, the video encoder, and
the two VCR cassette decks. Each hydrophone interfaces with
its own signal conditioning card as shown in Figure 3-9,
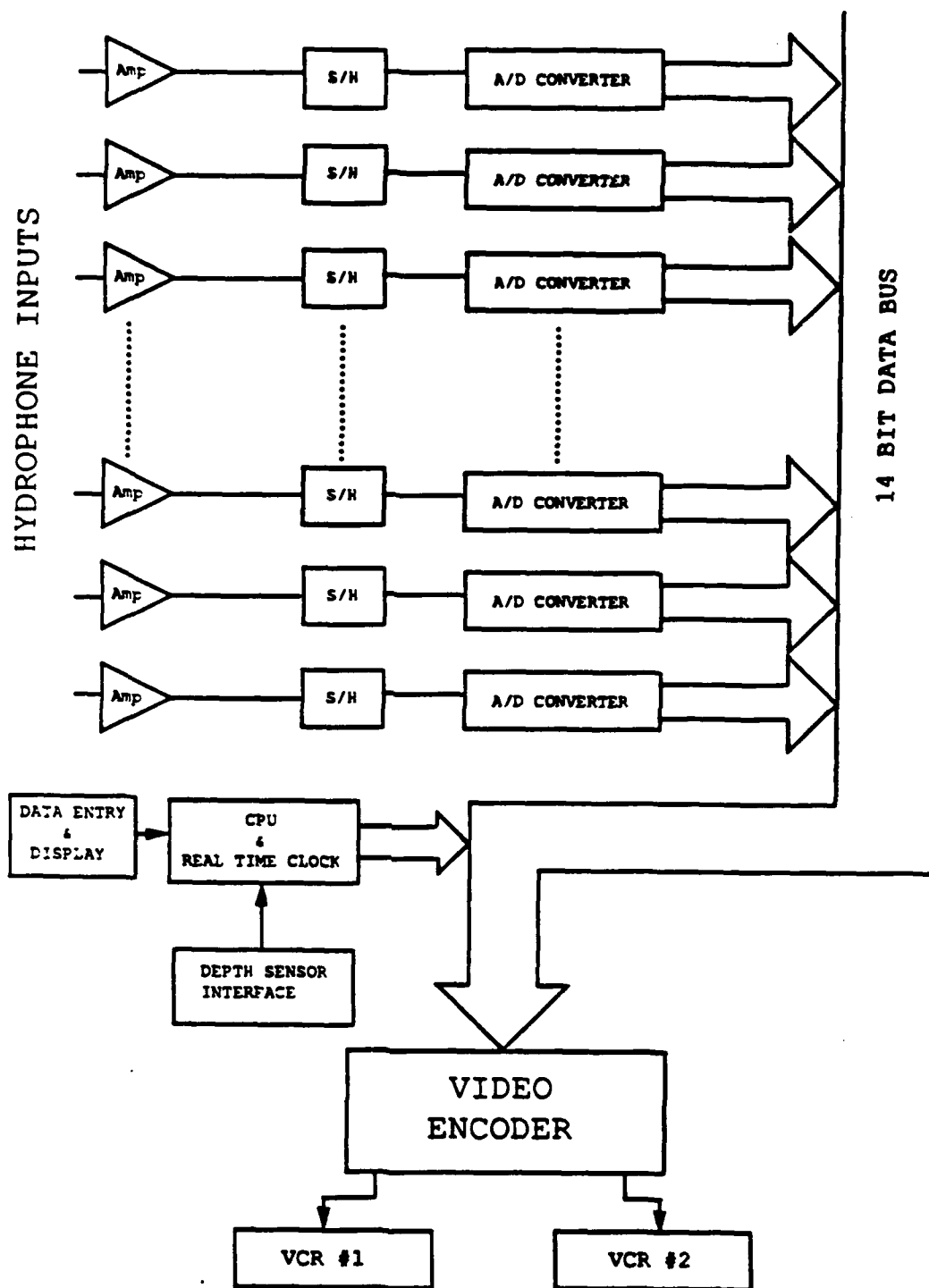where gain and pre-emphasis were applied via thumbwheel

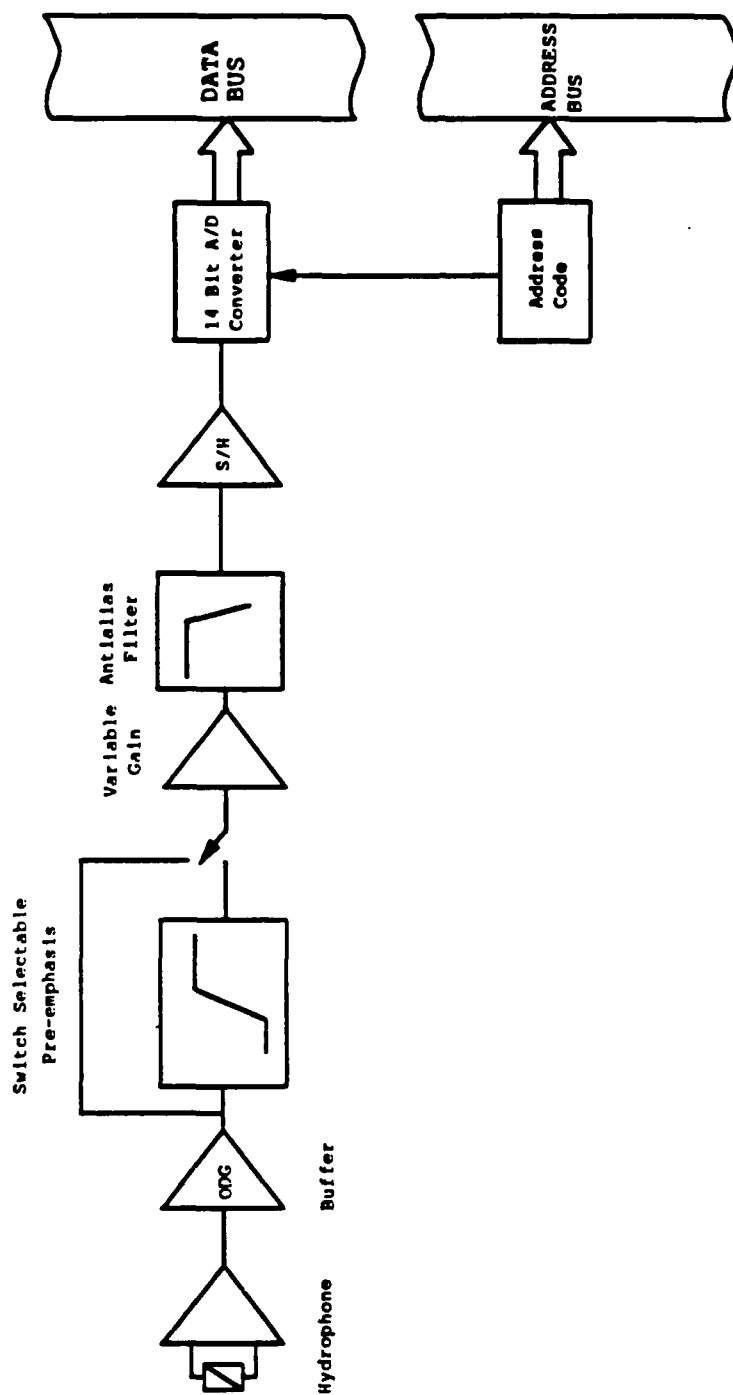Figure 3-8 Block Diagram of SEACAL System Electronics

Figure 3-9 Block Diagram of SEACAL Single Hydrophone

settings on each of the cards. Selecting pre-emphasis
applied a 6 dB/octave (starting at 0 dB rolloff at 1000 Hz)
to the incoming signal. Table 3-1 contains the computed
values for the frequencies used during the experiment.

Table 3-1 SEACAL Pre-Emphasis Values

Pre-emphasis(G2) = 20 log (freq/1000)	
Frequency (Hz)	Pre-emphasis (dB)
10	-40.00
15	-36.48
20	-33.98
25	-32.04
30	-30.46
35	-29.12
40	-27.96
45	-26.94
50	-26.02
55	-25.19
75	-22.50
175	-15.14
275	-11.21
375	-8.52
425	-7.43
525	-5.60
600	-4.40

An anti-aliasing filter and an eight pole Tchebychev filter were applied prior to 14 bit A/D conversion. The channels were sampled simultaneously to preserve the phase information and transferred along with digital words containing depth, time code, and synchronization data in a fixed repeating sequence to the video encoder circuit. The video encoder circuit converted the data to a serial format for recording onto the VCR's. The SEACAL system ON/OFF recording sequences were programmed on the system control panel prior to deployment. The buoy and array were powered with a 12 volt gelled electrolyte battery housed separately.

The "Quick Look" playback system was used at-sea to assess the quality of the data tapes recorded with the SEA-CAL system. The unit decoded the digital data from the video format in both analog and digital form. The playback system was equipped with a single DAC (digital-to-analog) channel, which was used to view the recorded data. Quality assessment of the data was accomplished at-sea with the dry-end companion "Quick Look" system. After retrieving the VCR cassette tapes, the "Quick Look" playback system allowed the identification of problems and adjustment of the signal gain for optimum signal-to-noise ratios. Shown in Figure 3-10 is an example of an at-sea spectrum. The source transmitted four frequencies simultaneously.

Accurate measurements of the distance between source and receiver were required since the objective of the experiment was to measure transmission loss as a function
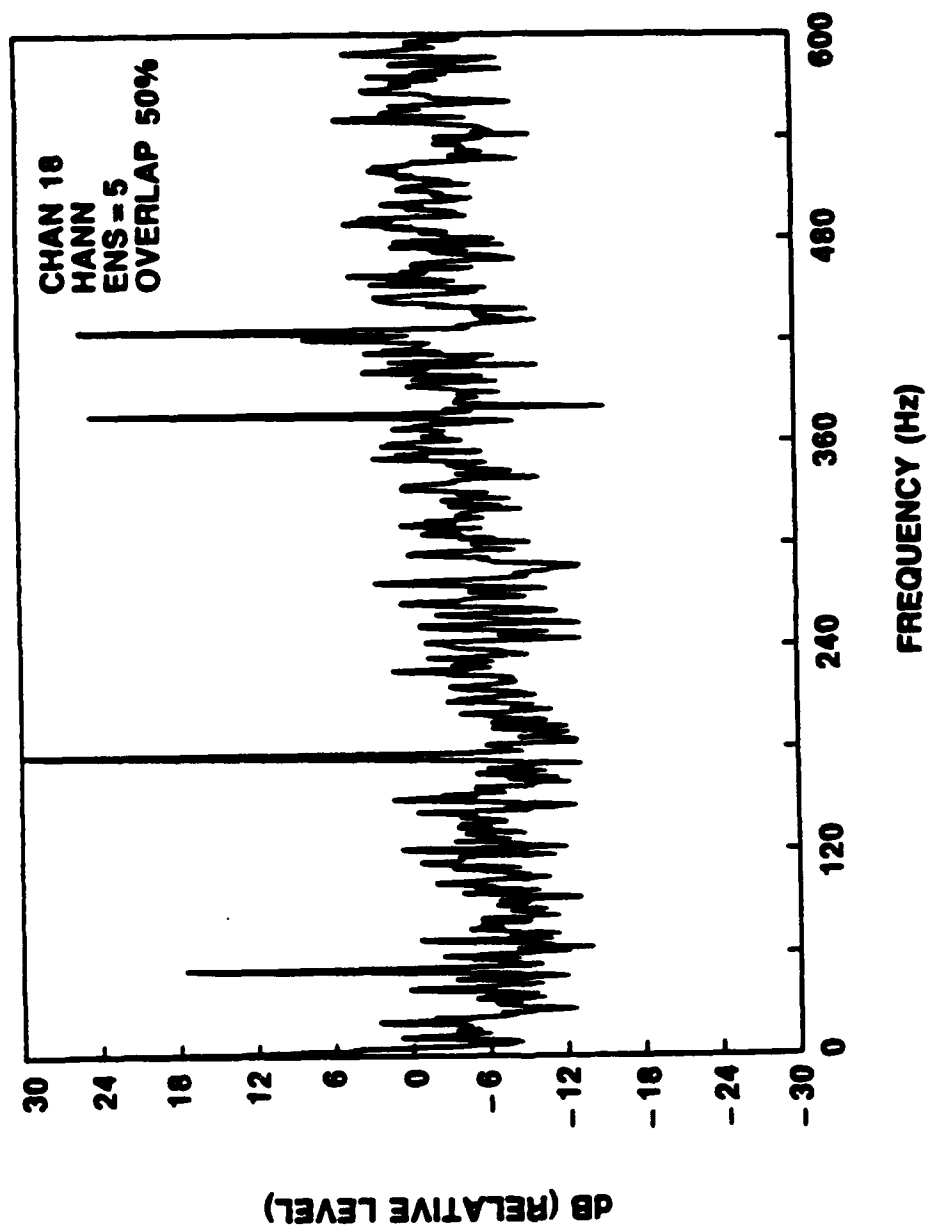
54

Figure 3-10 At-Sea Spectra of Four Frequencies

of range. Even greater accuracy was needed for the synthetic aperture processing, which requires integration of the pressure field over known range intervals. A Del-Norte radar ranging system and a SAIC auto-logging program for LORAN data were employed for the measurement of the range between the source and receiver.

The Del-Norte radar ranging system, which is the more accurate system, was used for the synthetic aperture processing. A radar transponder was attached to the spar buoy, which was tethered to the receive hydrophone array. Another radar transponder was attached to the mast of the ship which towed the source. The ship's radar transponder interfaced with a Compaq computer for automatic logging of the range data. The Del-Norte system was calibrated prior to the experiment and corrected for any range offset errors. This calibration was checked at-sea by comparison with sextant readings at close ranges. Figure 3-11 displays the Del-norte radar range transponder data for run TL2-2, the synthetic aperture run. The linearity with time indicates high resolution synthetic aperture processing is feasible.

Since the range of the transmission loss experiment exceeded the operational range of the Del-Norte system, the SAIC computer program was used to automatically log the output of the LORAN system. Latitude and longitude were stored at specified time intervals. A computer program was subsequently written to convert the latitude and longitude
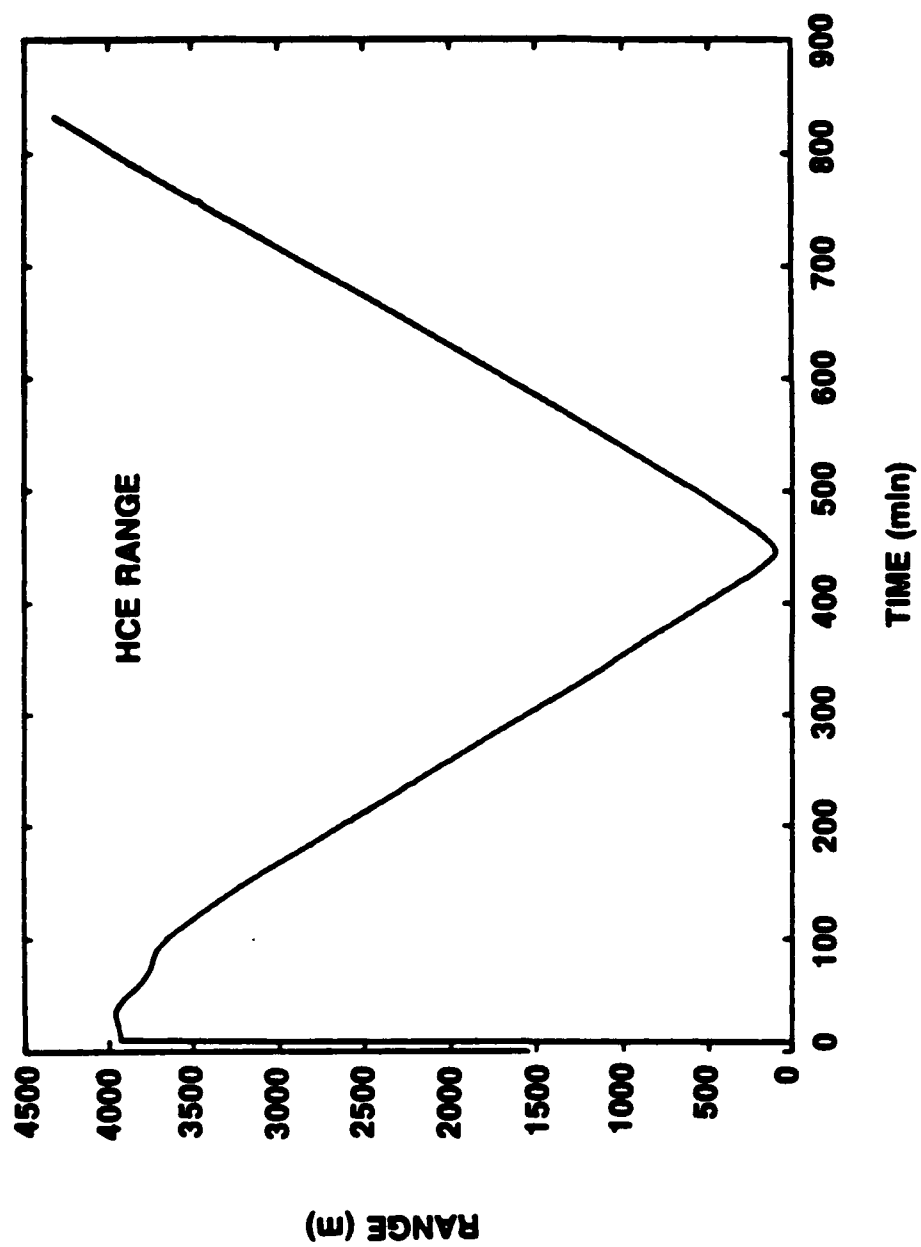
Figure 3-11 Del-Norte Radar Range Data

data to range versus time files, the latitude and longitude of the receive array being constant. At 15 minute intervals, the ship's bridge also logged the latitude and longitude of the ship to mark its position. This log was used as a check for the SAIC auto-logging system. Both agreed closely.

3.3 Data Processing

Hydrophone and depth sensor data were recorded on VCR cassette tapes using the C&M SEACAL data acquisition system described in Section 3.2. The SEACAL playback system was incorporated to transcribe the data from VCR tapes onto nine track digital tapes compatible with the VAX operating system, which was used to process the data.

Each data tape contained about 15 minutes of acoustic data. Since some of the experimental events lasted 4 hours, a two step process was used to reduce the data set to a size that could be stored in a computer file. The processing required the received signal level of the transmitted frequency. The data were transformed into the frequency domain using an FFT algorithm. The frequency bins containing the transmitted frequencies were stored along with adjacent frequency bins to ensure that the peak was recorded. Four noise bins were also stored to obtain estimates of the signal-to-noise ratios.

Several computer programs were developed to process the data contained on the nine track tapes. Data analysis of the boundary impedance results at discrete ranges required the source level and the addition of gain and calibration factors to determine transmission loss at a particular range. Transmission loss as a function of range required that the range versus time data be merged with the signal to noise versus time data. The range data for each

run were fit with a cubic spline and interpolated at the times when acoustic data were collected. The source level, gain, and calibration factors were added to estimate transmission loss versus range. The received signal versus range data were used to determine the wavenumber spectra using the techniques developed in Section 4.5.

4 Experimental Results

The ocean, together with its boundaries, forms a complex medium for the propagation of sound. The intricacies of the internal structure, surface, and bottom properties create many diverse effects on the initial waveform emitted from the sound source. In this section, the results of the pressure gradient measurements, transmission loss, and wavenumber spectra are presented.

Sound waves with discrete frequencies between 10 Hz to 55 Hz were transmitted from an acoustic source to obtain a single mode in the waveguide with adequate signal strength. A single mode simplifies the determination of boundary impedance using the method proposed in this dissertation. For unattenuated transmission, there will be a low frequency cutoff for each mode. The water depth, which was greater than expected, decreased the frequency for single mode propagation. Due to the poor low frequency response of the sound source and the high noise levels, the result for frequencies below cutoff were noise contaminated.

The pressure profile results are presented as pressure magnitude and pressure phase versus depth. For the frequencies shown to propagate a single dominant mode, the pressure gradient at the boundary was calculated and the impedance determined as described in Section 2.1.3. The lower frequencies, below 20 Hz, were shown to have poor signal-to-noise ratios. The frequencies of 25 and 35 Hz

appeared to have a dominant mode with adequate signal strength. Frequencies of 45 Hz and higher appeared to contain additional modes shown as a more complex modal structure.

The transmission loss and wavenumber results will be used to determine many factors, such as the number and amplitude of propagating modes, bottom properties by inverse methods, and uniformity of the sound channel as a function of range. The complex pressure versus range is required for the calculation of wavenumber spectra. The transformation into the wavenumber domain displays the propagating modes in the waveguide. The wavenumber spectra can also illustrate other effects such as shear waves. Shear waves, which travel through the sediment at a slower velocity, would be seen at the higher wavenumbers due to the relationship $k = \frac{\omega}{c}$. The uniformity of the sound channel can be analyzed by comparisons of the pressure fields of the incoming and outgoing radials.

4.1 Determination of Pressure Gradients

Theoretical expressions may be derived for the vertical distribution of sound pressure in a homogeneous medium bounded by a free surface and a bottom with normal impedance Z. These expressions are valid if certain constraints are applied. The vertical distribution of underwater sound pressure for a propagating mode should form a standing wave shape. The character of this mode shape is a function of the physical and acoustical characteristics of the experimental site and is also a function of the bottom impedance, which is generally complex. The real part determines the limits between which the shape oscillates; the imaginary part determines the initial phase of the system. The expression from section 2-1, equation 2-12, defines the pressure and particle velocity as

$$P = \rho \frac{\partial \psi}{\partial t} \qquad\qquad 4-1$$

$$\dot{w} = U = \frac{\partial \psi}{\partial z}. \qquad\qquad 4-2$$

In Section 2.1.3 the normal complex impedance is defined as the ratio of the acoustic pressure to the normal component of the particle velocity. This can be expressed as

$$Z = \frac{P}{U} = \frac{\rho\left(\frac{\partial \psi}{\partial t}\right)}{\left(\frac{\partial \psi}{\partial z}\right)}. \qquad\qquad 4-3$$

Taking the expression derived in section 2.1.1, equation 2-19, for the solution of the wave equation for the inhomogeneous case and differentiating with respect to time results in the following expression for the acoustic pressure:

$$\Phi_2 = e^{i\omega t}\Psi(r,z,\omega) \qquad\qquad 4-4$$

$$\rho\frac{\partial\Phi_2}{\partial t} = \rho i\omega\Psi(r,z,\omega). \qquad\qquad 4-5$$

The normal component of the particle velocity can be obtained by using equation 2-12:

$$U = \frac{\partial\psi}{\partial z} = \frac{\partial\Phi_2}{\partial z} = \frac{\partial e^{i\omega t}\Psi_2(r,z,\omega)}{\partial z} \qquad\qquad 4-6$$

$$= 2e^{i\omega t}\int_0^\infty J_0(k_r)k\,dk\frac{\sin\beta_1 d}{\beta_1}\left[\frac{1}{\beta_1\cos(\beta_1 H)+i\sin\beta_1 H}\right]$$

$$[\beta_1^2\sin[\beta_1(H-z)]-i\beta_2\beta_1\cos[\beta_1(H-z)].$$

As stated previously, the impedance is the ratio of the pressure to the normal component of the particle velocity. Substituting equation 4-5 and equation 4-6 into equation 4-3 and cancelling common terms give us

$$Z = -i\rho\omega[\frac{\beta_1\cos[\beta_1(H-z)]+ib\beta_2\sin[\beta_1(H-z)]}{\beta_1^2\sin[\beta_1(H-z]-ib\beta_1\beta_2\cos[\beta_1(H-z)]]} \qquad\qquad 4-7$$

The above equation describes the impedance as a function of the height of the waveguide H, the density ρ, the frequency ω, and the wavenumber k (which is contained in the term β). Substituting $z = H$ into the above expression yields the following expression for the impedance at the ocean bottom:

64

$$Z = \frac{\rho_2 c_2}{\cos\theta} \qquad\qquad 4-8 :$$

This is the same result obtained in equation 2-53. At normal incidence, this equation is further reduced to $\rho_2 c_2$.

4.2 Boundary Impedance Calculations

Data obtained at frequencies of 10 Hz to 55 Hz were analyzed for the determination of the specific normal acoustic impedance at the boundary. The acoustic pressure was measured as a function of depth using the 24 element hydrophone array. The hydrophones were equally spaced at 2 1/2 m apart. The deepest hydrophone, number 24, was positioned on the ocean bottom to measure the acoustic pressure at the boundary. The data for all 24 hydrophones were processed to obtain calibrated pressure levels as a function of depth. Sixty- four ensemble averages of the spectra were used to obtain a stable result. Ensemble averaging of the spectra reduces the effect of the incoherent noise. The increased number of data samples increases the statistical data base and subsequently reduces the confidence interval. The data which have signal-to-noise ratios less than 6 dB were not considered.

The cutoff frequency of the waveguide for a single mode for a water depth of 73 m was calculated to be 23 Hz. The cutoff frequency for mode n for unattenuated propagation in a waveguide of height H is calculated by the equation

$$f_{co} = \frac{(2n-1)c_1}{4H\sqrt{1 - \frac{(c_1^2)}{(c_2^2)}}}$$

4-9

$$f_{co1} = \frac{(2(1)-1)1496m/s}{4(73m)\sqrt{\frac{(1496^2)}{(2017^2)}}} = 7.6Hz$$

$$f_{co2} = \frac{(2(2)-1)1496m/s}{4(73m)\sqrt{\frac{(1496^2)}{(2017^2)}}} = 22.9Hz$$

$$f_{co3} = \frac{(2(3)-1)1496m/s}{4(73m)\sqrt{\frac{(1496^2)}{(2017^2)}}} = 38.2Hz$$

where c_1 is the average sound speed in the water from Section 3.1.2.1. Since the calculation of the cut off frequencies is only approximate and subject to the specific environmental conditions, a sound source transmitted discrete frequencies between 10 and 55 Hz to attempt to obtain a single propagating mode. Higher frequencies were transmitted from the source for a number of reasons: (1) it was not clear that the signal-to-noise ratio would be adequate at the low frequencies to produce stable results and (2) the frequencies of 50 Hz and 55 Hz could be compared with the transmission loss and wavenumber spectra results. To measure the gradient and determine the impedance when two or more modes are present, it would have been necessary to separately measure the contributions of the individual modes before determining the gradient.

Data from 24 hydrophones were processed to generate pressure versus depth profiles in the water column. Shown

in Figure 4-1 a-j are signal plus noise and noise versus depth for the transmitted frequencies. Sixty-four ensemble averages of the spectra produced a stable result in most cases. The results at 10 and 15 Hz were not stable enough for a good estimate of the pressure fields. Low source levels at these frequencies might have contributed to the poor signal-to-noise levels in the results. Both the 25, 30, and the 35 Hz results appear to have a dominant mode in the waveguide. At 45 Hz, the influence of an additional mode can be seen. This is more pronounced in the 55 Hz results. A strong interference can be seen between two dominant modes as a function of depth. This analysis is further supported by the phase plots shown in Figure 4-2 a-d for each of the four frequencies. Phase is a sensitive parameter which can show the interference between the modes. The 25 and 35 Hz results show a constant phase, as expected when one dominant mode propagates with a constant phase velocity. The 45 and 55 Hz results show a more complicated phase structure indicating the interference between modes.

Since the determination of impedance is a complex quantity, both the amplitude and phase of the pressure profiles need to be used in the calculation of the pressure gradient. As expected, the gradient of the phase for a single dominant mode is shown to be essentially zero, and the phase measurement does not yield any information except to verify that a single mode is dominant in the waveguide. The impedance can then be calculated by the ratio of the
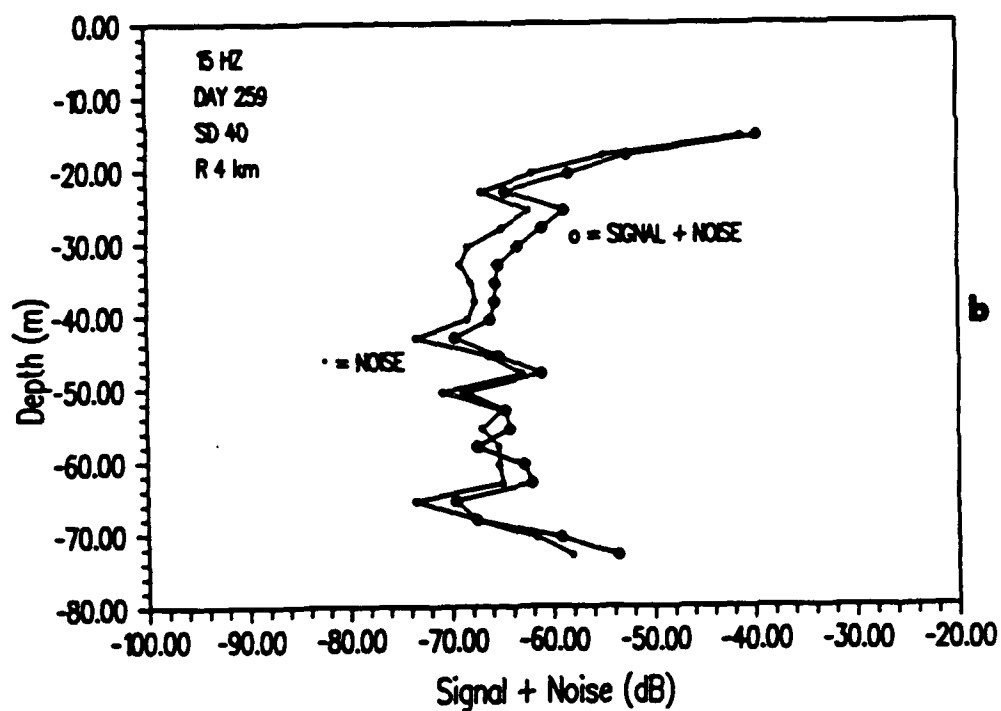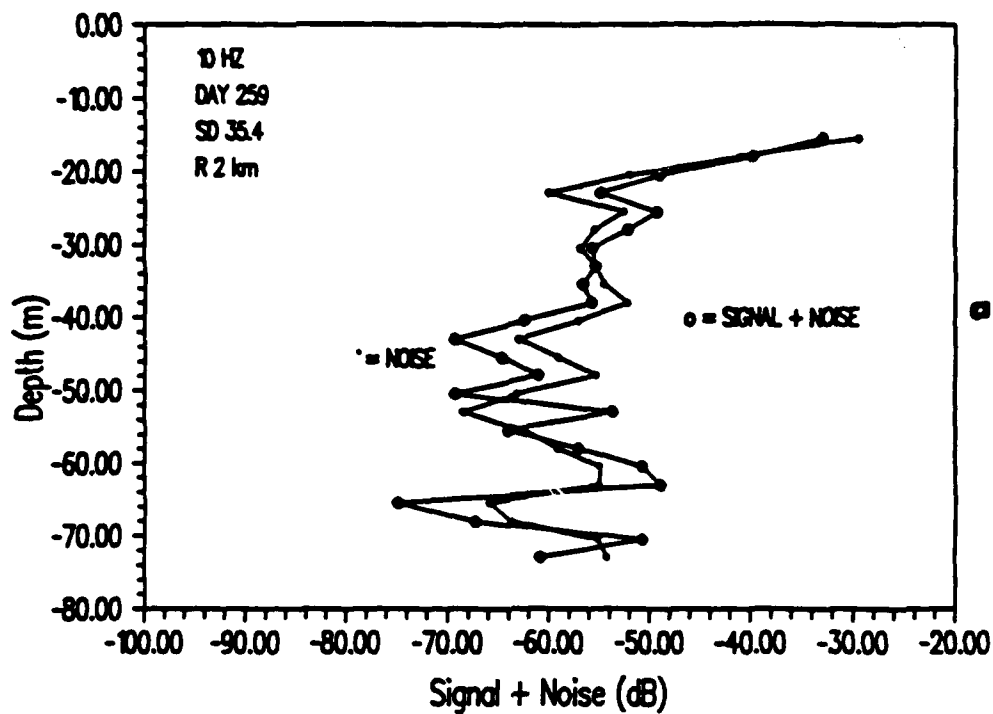
Figure 4-1 Signal plus Noise and Noise versus Depth
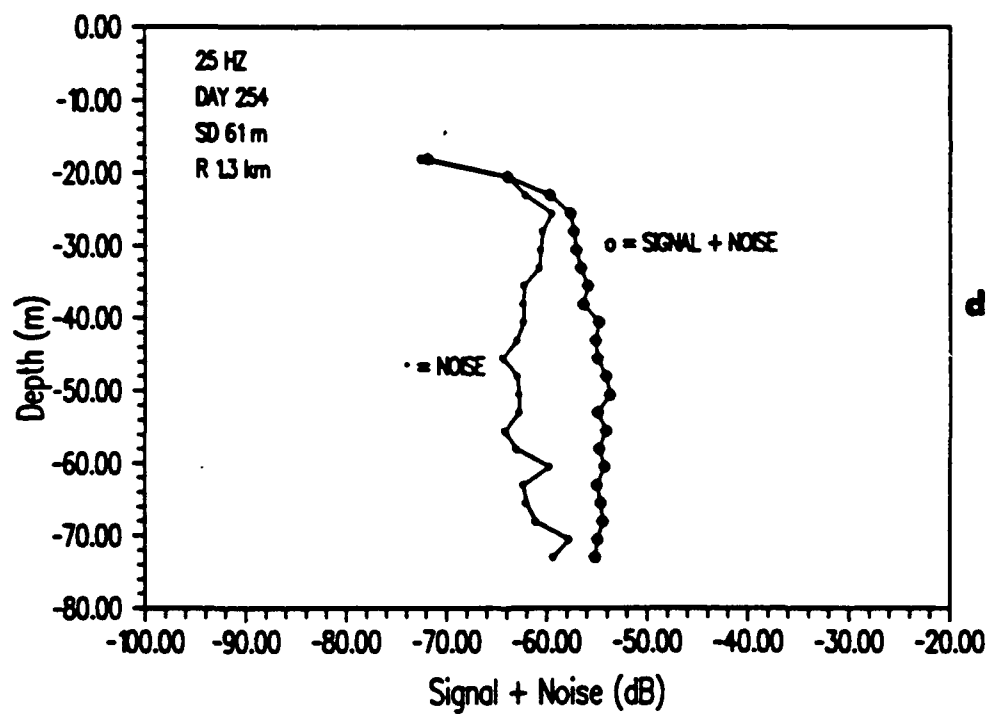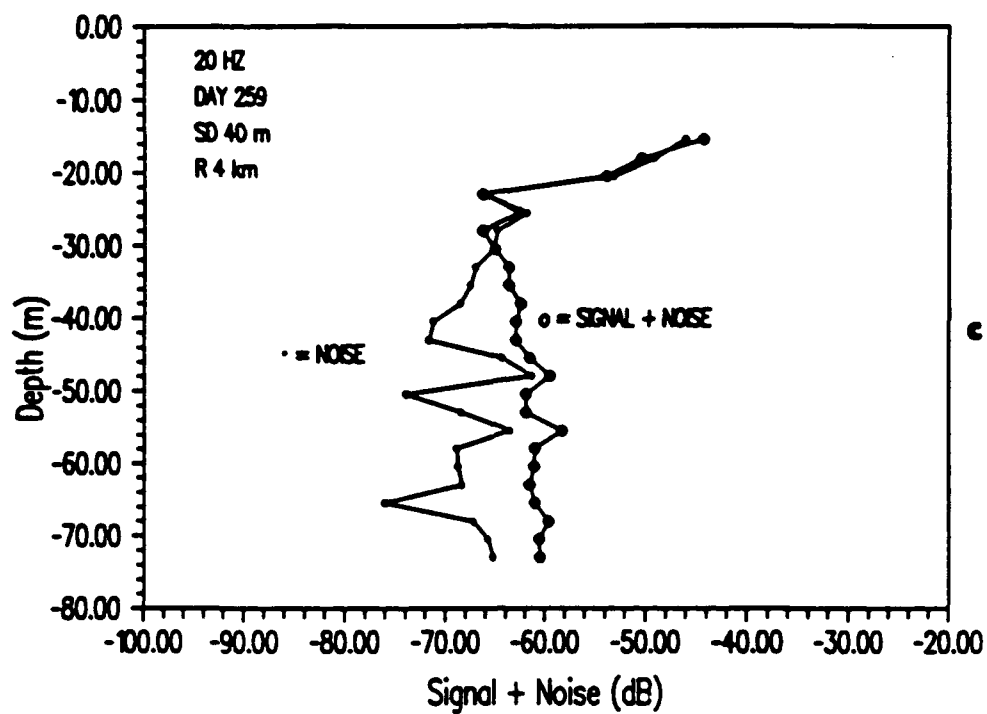a. 10 Hz , b. 15 Hz

Figure 4-1 (cont'd) c. 20 Hz , d 25 Hz Day 254

70
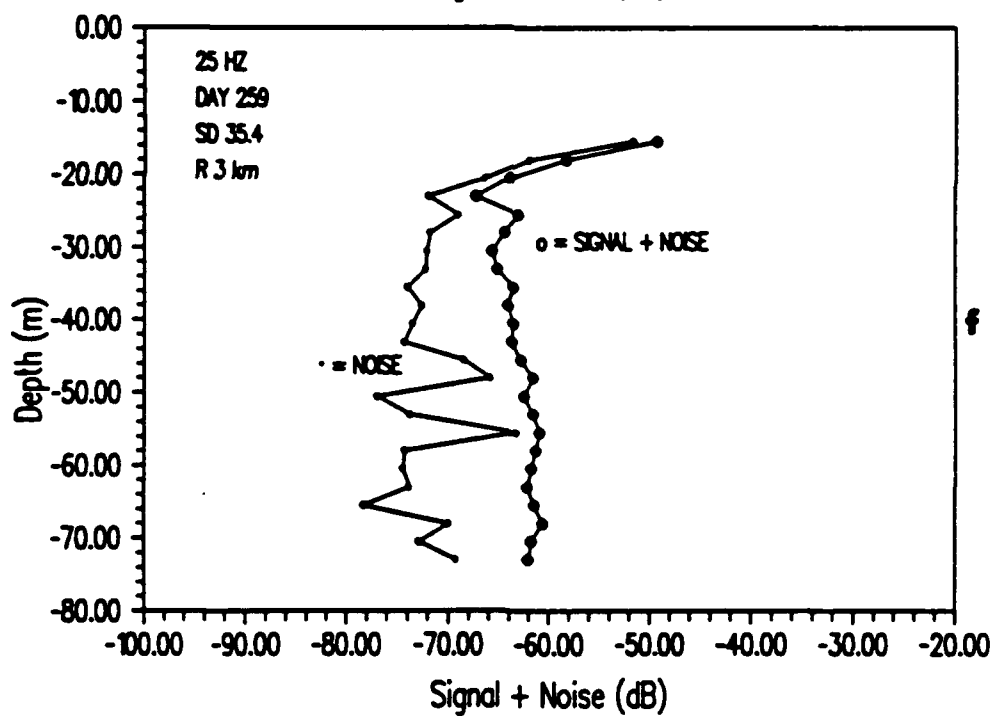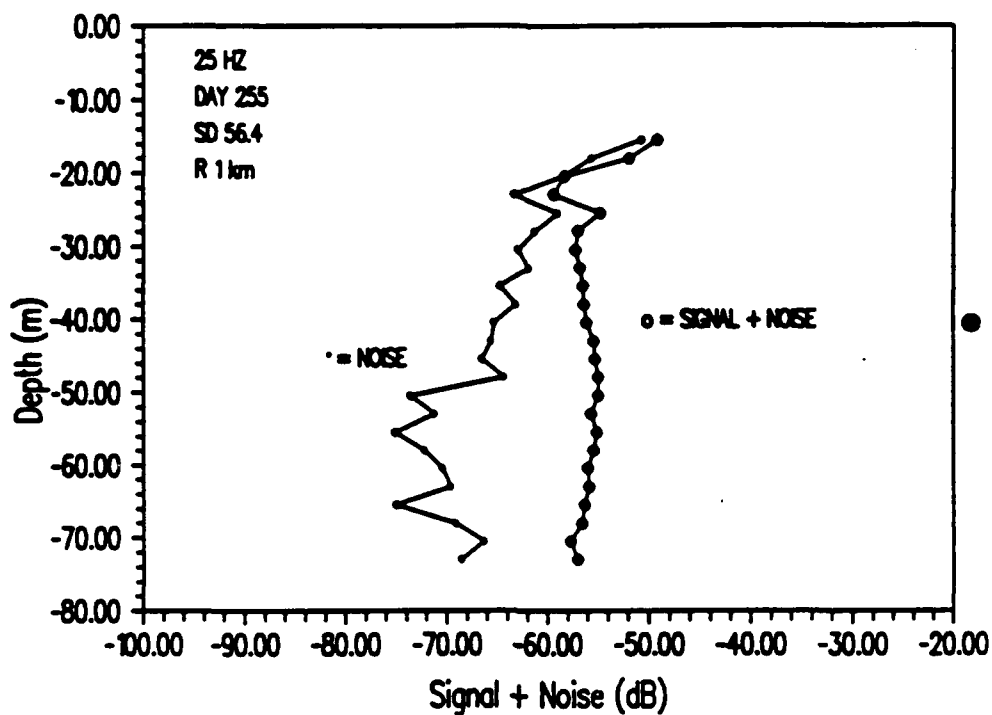
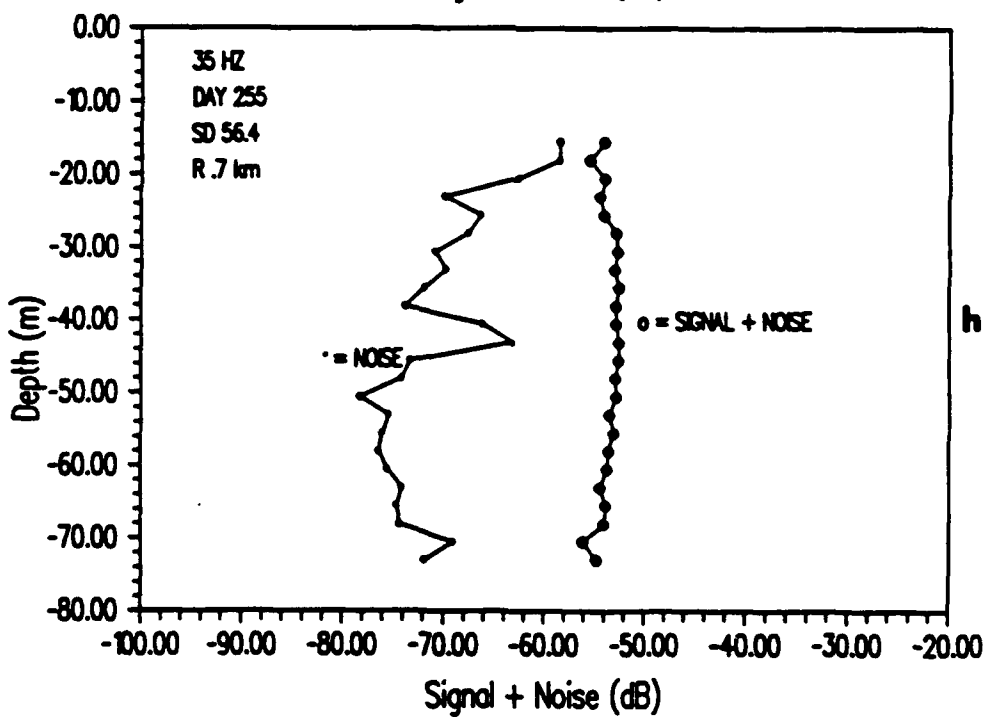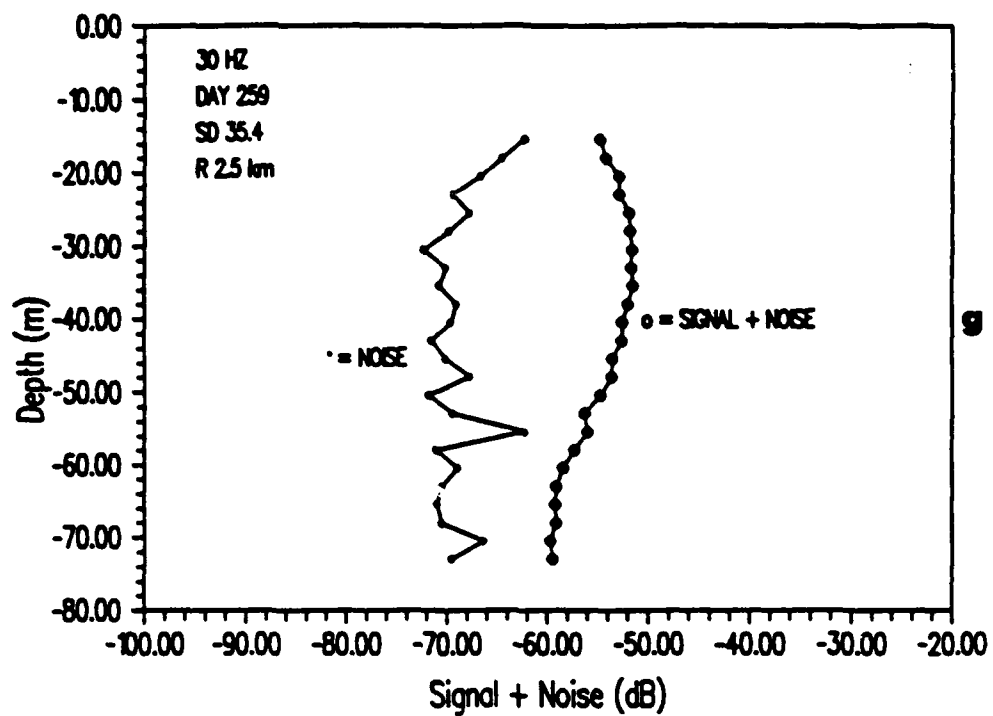Figure 4-1 (cont'd) e. 25 Hz Day 255, f. 25 Hz Day 259
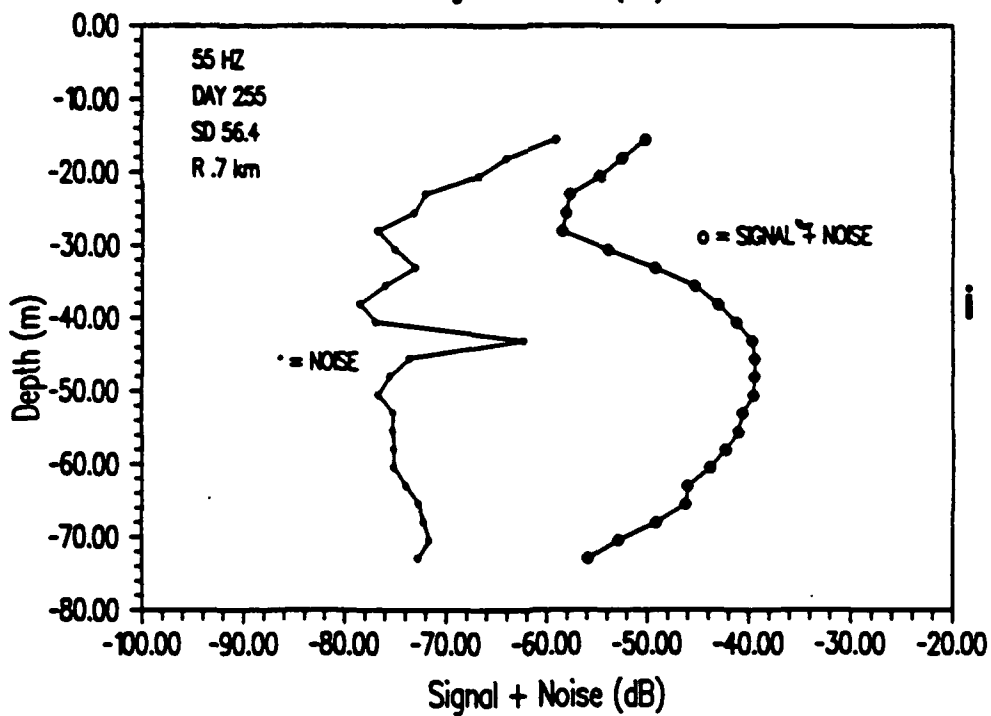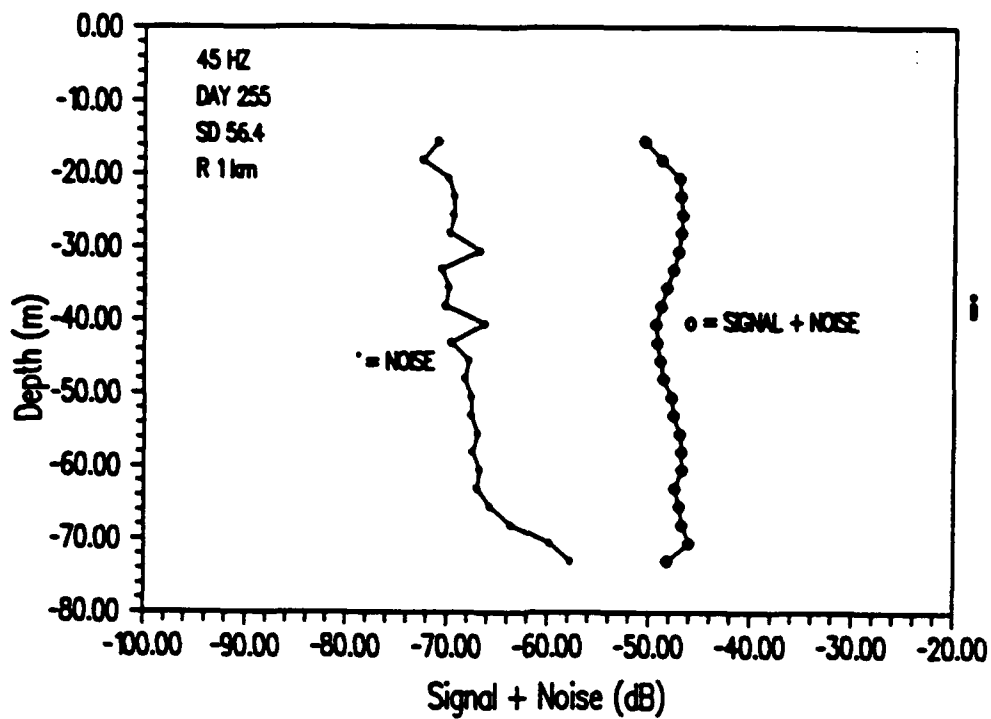
Figure 4-1 (cont'd) g. 30 Hz , h. 35 Hz

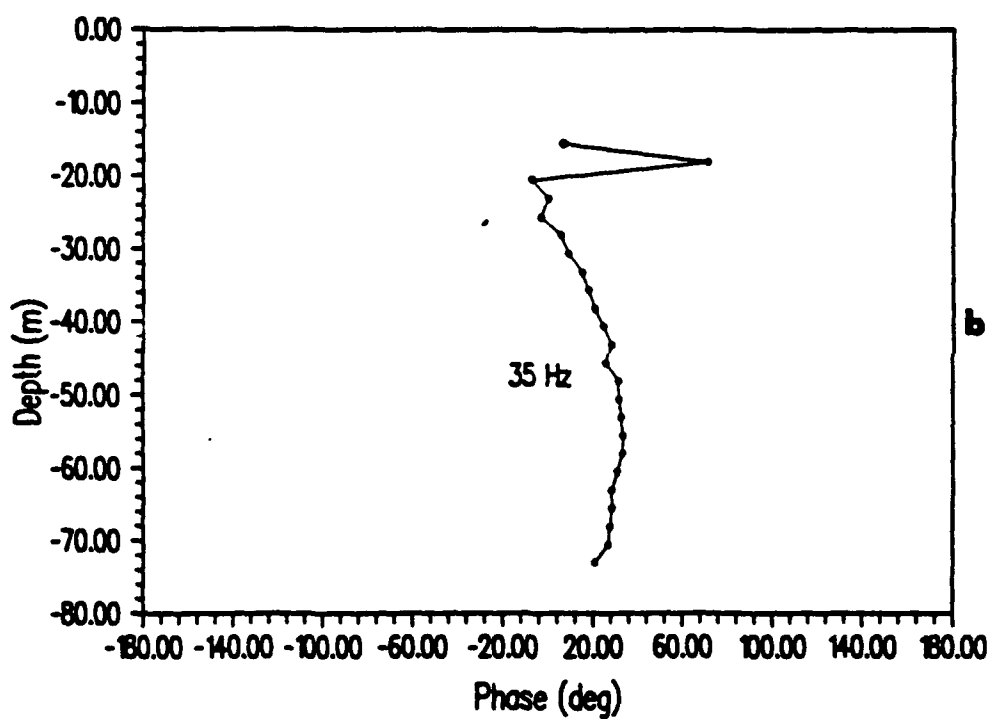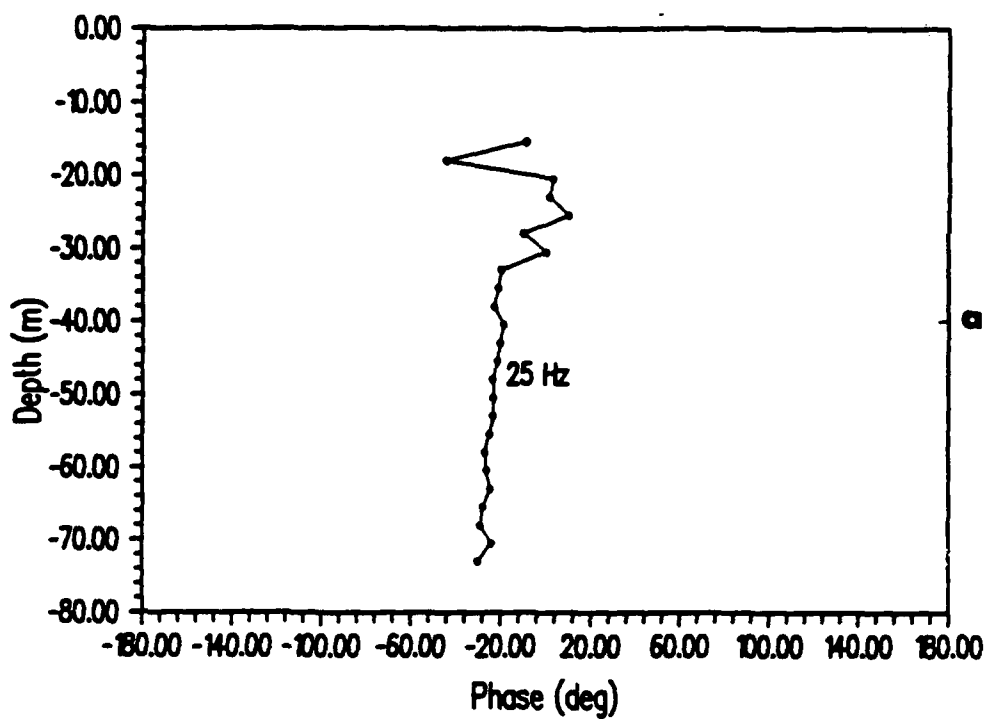Figure 4-1 (cont'd) i. 45 Hz , j. 55 Hz

Figure 4-2 Pressure Phase versus Depth
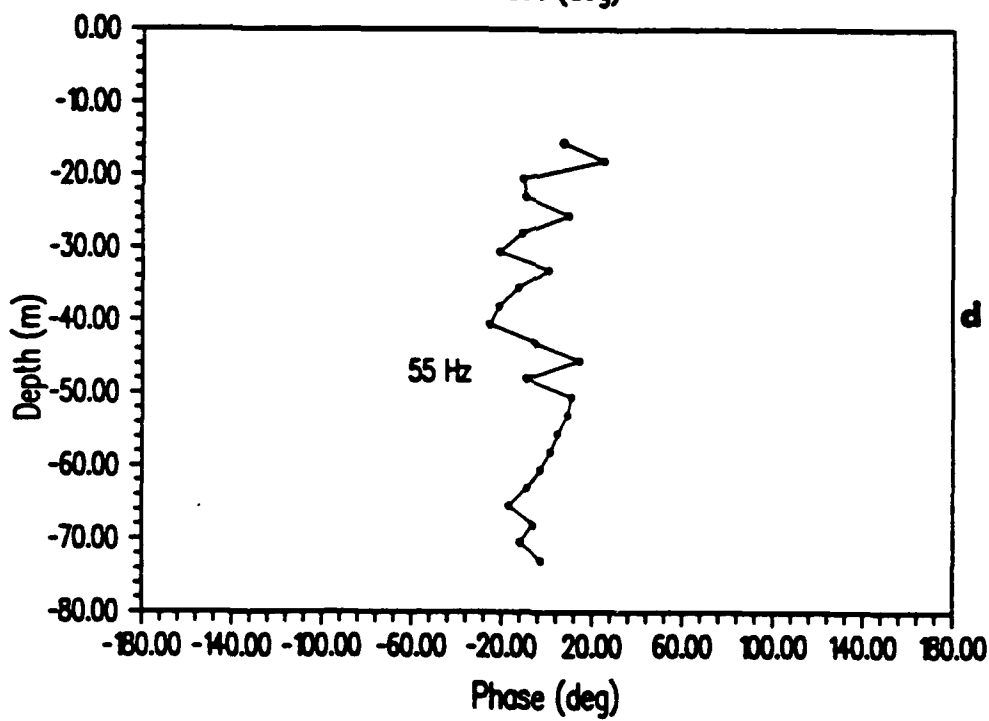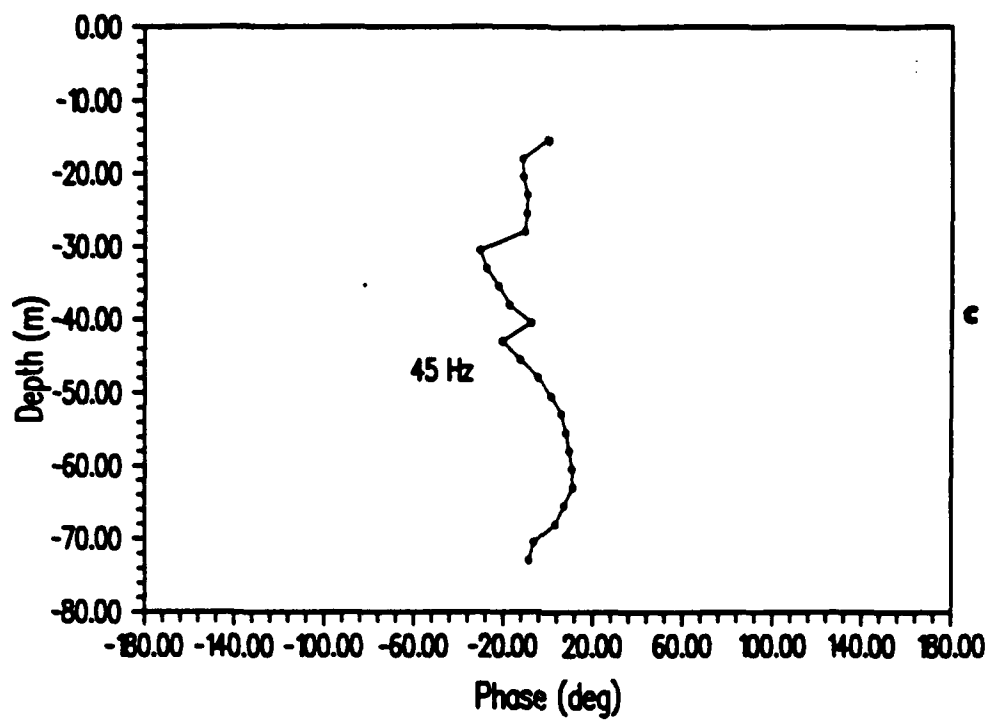a. 25 Hz , b. 35 Hz

Figure 4-2 (cont'd) c. 45 Hz , d. 55 Hz

gradient of the pressure magnitude to the complex pressure.

Determination of the normal component of the particle velocity was obtained using the following relationship:

$$U = \frac{\partial \psi}{\partial z} = \frac{1}{i \omega \rho} \frac{dp}{dz}$$
4-10

The above equation is true considering the following condition; the only variable in the evaluation is the pressure as a function of depth, the range and frequency are held constant.

The pressure magnitudes of the hydrophones positioned near the bottom were used to calculate the gradient for the 25, 30, and the 35 Hz results. The number of hydrophones were chosen by a least squares calculation of slope, which yielded the maximum correlation coefficient. The correlation coefficients are a judge as to the fit of a line through the given points. Determining the number of hydrophones using the maximum correlation coefficient evaluates the pressure gradient with minimum error. The gradient calculations are used to determine dP/dz.

Figure 4-3 a-f shows the least squares fit of the calibrated pressure amplitude versus depth results for 25 Hz, 30 Hz, and 35 Hz. The signal plus noise results were calibrated to obtain values of transmission loss versus depth using equations to be presented in the following section. The 25 Hz data were obtained on 3 different days at three different source depths: Julian day 254 at a source depth of 61 meters, Julian day 255 at a source depth of
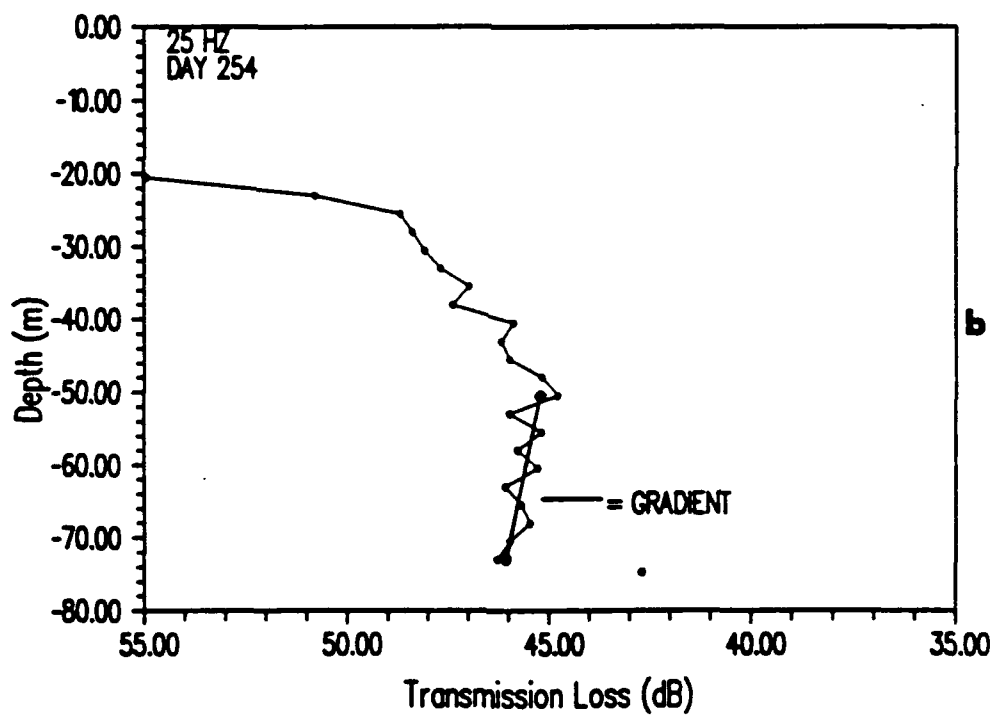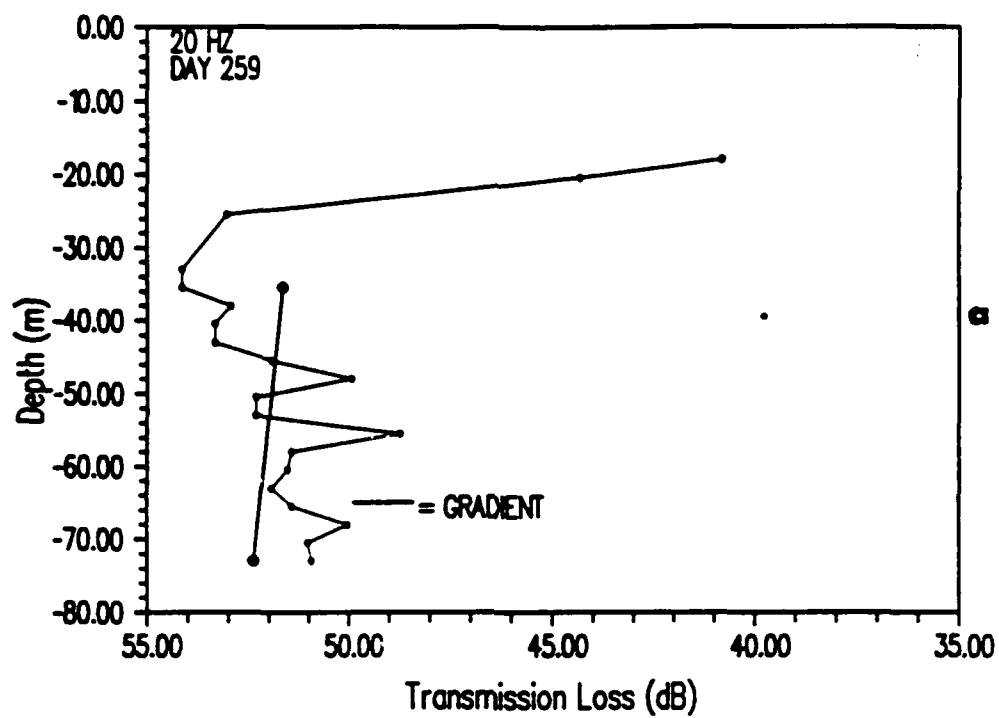
Figure 4-3 Least Squares Fit of Pressure Gradient
a. 20 Hz , b. 25 Hz Day 254
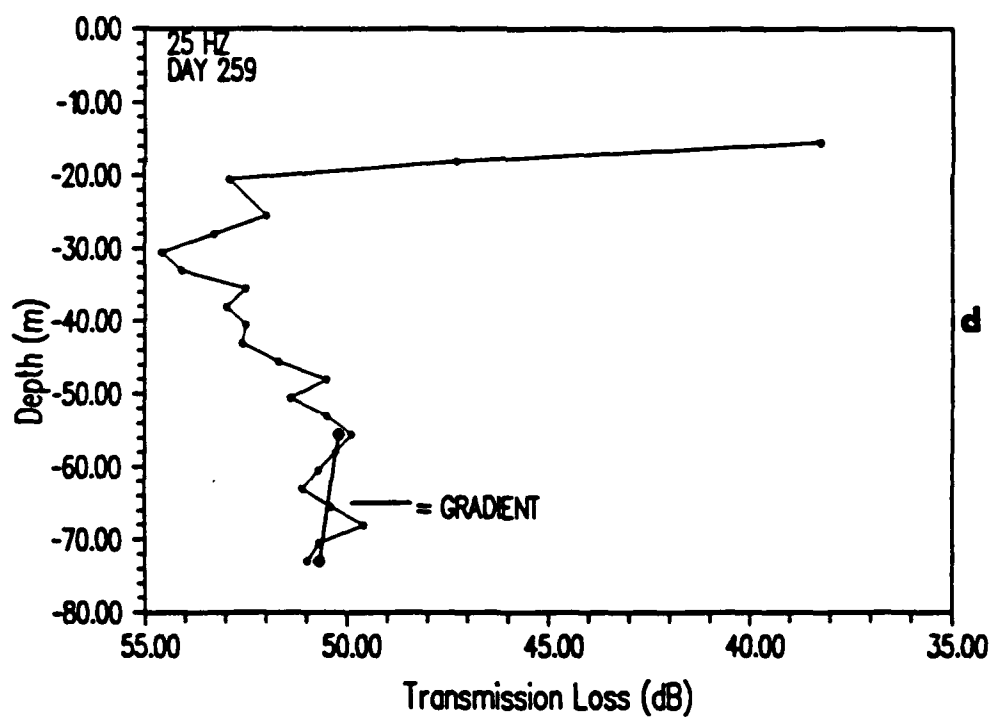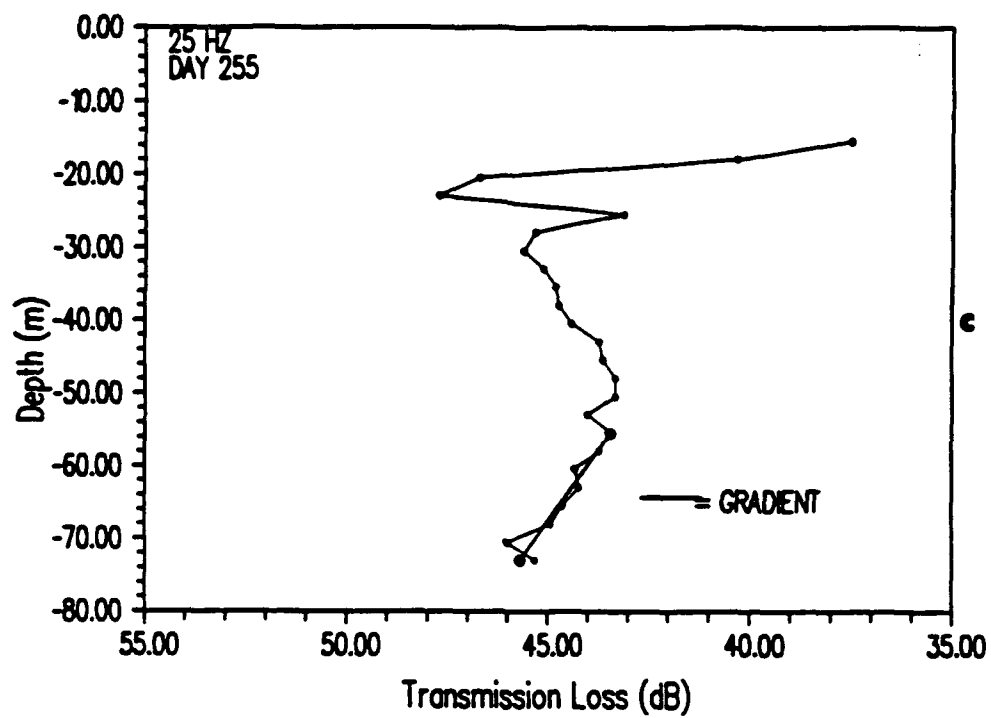
Figure 4-3 (cont'd) c. 25 Hz Day 255 d. 25 Hz Day 259
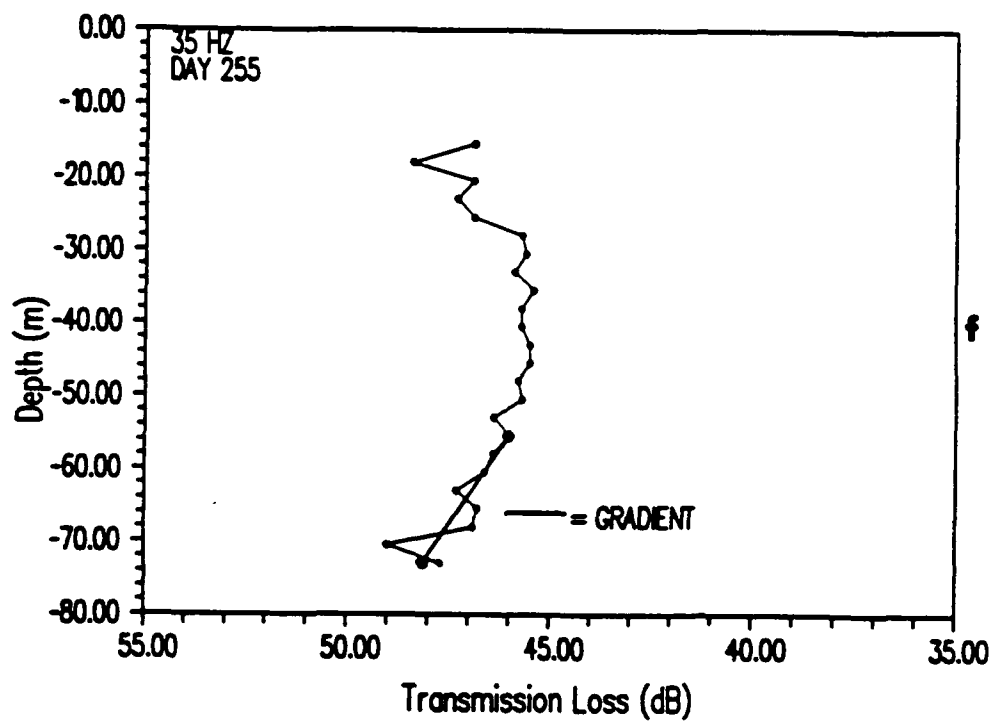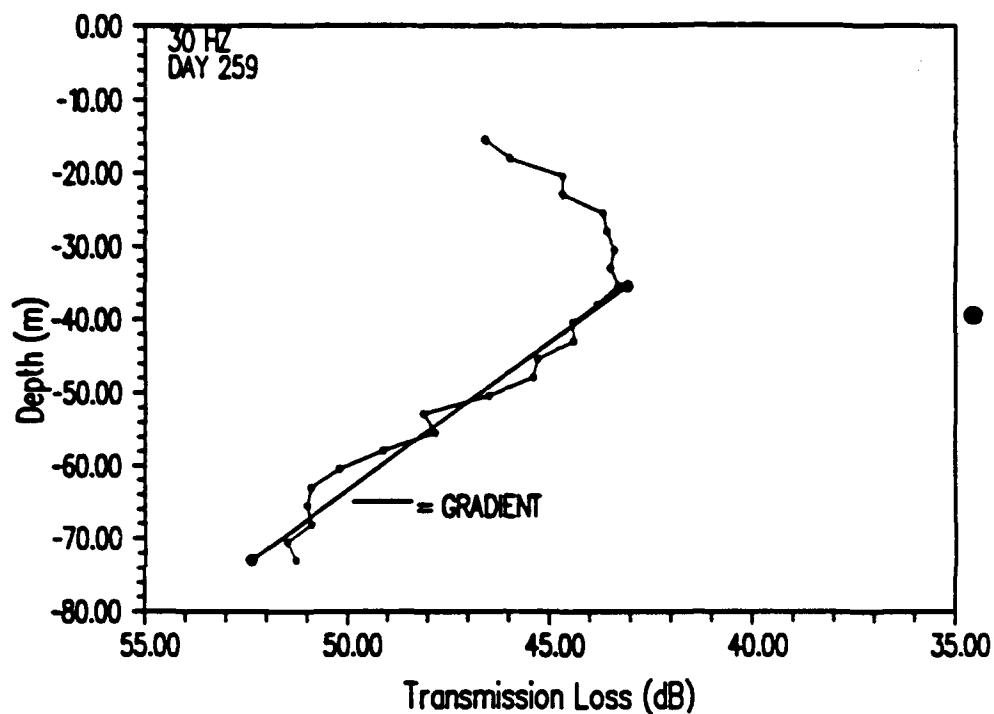
Figure 4-3 (cont'd) e. 30 Hz , f. 35 Hz.

56.4 meters, and Julian day 259 at a source depth of 35.4 meters. The 30 Hz results occurred on Julian day 259, and the 35 Hz results occurred on Julian day 255. The slope obtained from the least squares fit was used to determine the pressure at the boundary, P_1, and the pressure at the hydrophone, P_2. The resulting ΔP was used to calculate the gradient as follows:

$$Z = i\omega\rho \frac{P_1}{\frac{\Delta P}{\Delta z}} = i\omega\rho \frac{\Delta z P_1}{P_2 - P_1} \qquad 4-11$$

If we divide through by P_1, we then have

$$Z = i\omega\rho \frac{\Delta z}{[\Delta P - 1]} \qquad 4-12$$

Since the pressure profiles were computed using a logarithmic scale, the ratio of P_2 to P_1 needed to be calculated as follows

$$20\log\left[\frac{P_2}{P_1}\right] = P_2 - P_1 \qquad 4-13$$

$$\left[\frac{P_2}{P_1}\right] = 10^{\left(\frac{P_2 - P_1}{20}\right)}$$

The values of impedance determined using this method are included in Table 4-1. Freq is the frequency, SD is the source depth, R is range, CC is the correlation coefficient, and Z is the impedance. The results summarized in Table 4-1 display a wide range of values for both impedance and correlation coefficients. The data which have the high-

est values for the correlation coefficient, 0.9 and higher, report values for impedance of 9.320 x 10^6kg/m^{2}s and 3.686 x 10^6kg/m^{2}s.

Table 4-1 Measured Values of Boundary Impedance

Freq.	Day	SD	R	CC	Z (10^6)
20 Hz	259	40 m	4 km	.5584	16.412 kg/m^{2}s
25 Hz	254	61 m	1.3 km	-.6090	3.199 kg/m^{2}s
25 Hz	255	56.4 m	1 km	-.9297	9.320 kg/m^{2}s
25 Hz	259	35.4 m	3 km	-.3191	49.439 kg/m^{2}s
30 Hz	259	35.4 m	2.5 km	-.9807	3.686 kg/m^{2}s
35 Hz	255	56.4 m	.7 km	-.7910	13.990 kg/m^{2}s

These results can be compared to a simple calculation of impedance using the equation $Z_2 = \rho_2 c_2 \cos\theta$. Since the vertical array measures the normal component of the impedance this equation reduces to $Z_2 = \rho_2 c_2$. The values of ρ and c derived from measured geophysical parameters reported by T. Yamamoto yields an impedance of 4.034 x $10^6 \frac{kg}{m^2 s}$.

A calculation of impedance using a single value of the sonic velocity at the boundary may be misleading since many layers of different sound speeds have been reported. Table 5-1 shows the estimated sound speed in the sediment to a depth of 250 meters. In addition, T. Yamamoto reports the existence of a gradient in the first layer of the sediment. For these reasons, the calculation of impedance using these parameters needs to be considered or bounded.

The maximum impedance was calculated using the average sound speed over 250 meters (all six layers) of 2109 m/s. This corresponds to an impedance of 4.437 x 10^6kg/m^{2}s . The minimum impedance of 2.974 x 10^6kg/m^{2}s was obtained using an average sound speed in the first layer of 1752 m/s.

In general, the impedance determined using the acoustic technique yielded higher values than the calculated impedance using the measured geophysical properties. Only two estimates of the impedance using the acoustic technique, 25 Hz and 30 Hz, fell within the bounds of the impedance calculated using the sediment properties.

4.3 Determination of Transmission Loss

Transmission loss is a measure of the magnitude of the decay of sound between the source and receiver, and it includes all the attributes and characteristics of the internal structure, including the surface and bottom boundaries. By definition, the transmission loss describes the decay of sound between a point 1 m from the source and the receiver. The definition is, from Urick (1967),

$$TL = 10 \log \frac{I_o}{I_1} \qquad\qquad 4-14$$

where I_o is the intensity at the reference point located 1 m from the acoustic center of the transducer and I_1 is the intensity at the receiver.

Transmission loss or propagation loss for at-sea measurements were determined using the following equation:

$$TL = SL - SW \qquad\qquad 4-15$$

where SL is the source level in decibels (dB//1μPa at 1 meter) emitted from the sound source and SW is the signal level (dB//1μPa) in the water received by the array. The signal level in the water was determined from the voltage level and the addition of the signal conditioning gains of the SEACaL system, amplification, attenuation, and correction gains. The equation used to determine the signal level in the water was

$$SW = VOLT + HYDSENS + GAIN1 + GAIN2 \qquad\qquad 4-16$$

where $VOLT$ is the voltage level (dB//1µPa) obtained from the digital tape, $HYDSENS$ is the hydrophone sensitivity (dB//1microPa at 1 meter), $GAIN1$ is the channel amplifier gain in the SEACAL System, and $GAIN2$ is the de-emphasis gain in the SEACAL System. The de-emphasis was used to reduce the effects of strum in the array cable and the clanging of the sub-surface buoy. The hydrophone sensitivity was determined during the calibration procedure. The calculation of transmission loss as a function of range required that the results of the transmission loss versus time be merged with the range versus time files from the Del-Norte and LORAN-C ranging systems.

4.4 Transmission Loss Results

Transmission loss results were obtained at eight frequencies between 50 and 600 Hz for ranges of approximately 30 kilometers. The transmission loss was calculated using equations in section 4.3. Only three hydrophones were analyzed for the transmission loss test due to time constraints imposed by the computer processing. The three hydrophones were located approximately mid-water depth (hydrophone 12), three-quarter water depth (hydrophone 18), and on the bottom/sediment (hydrophone 24)

Figure 4-4 shows the transmission loss results for four frequencies over a 4 km range. A strong interference pattern, indicating two modes, is apparent in the 50 Hz data. The periodic interference pattern can be thought of as a "beating" occurring between two modes travelling at different velocities, which would correspond to different path lengths. A stationary source or receiver would not exhibit this phenomenon because two paths travelling at different velocities would exhibit only a constant phase difference. Since the source is moving, it is moving through the points where the received signal is alternately interfering with itself in a constructive and destructive manner. The magnitude of the pressure as a function of range for two trapped modes can be expressed as

$$(p(r)) = \frac{1}{\sqrt{r}}\left(a_1 e^{ik_{A1}r} + a_2 e^{ik_{A2}r}\right) \qquad 4-17$$
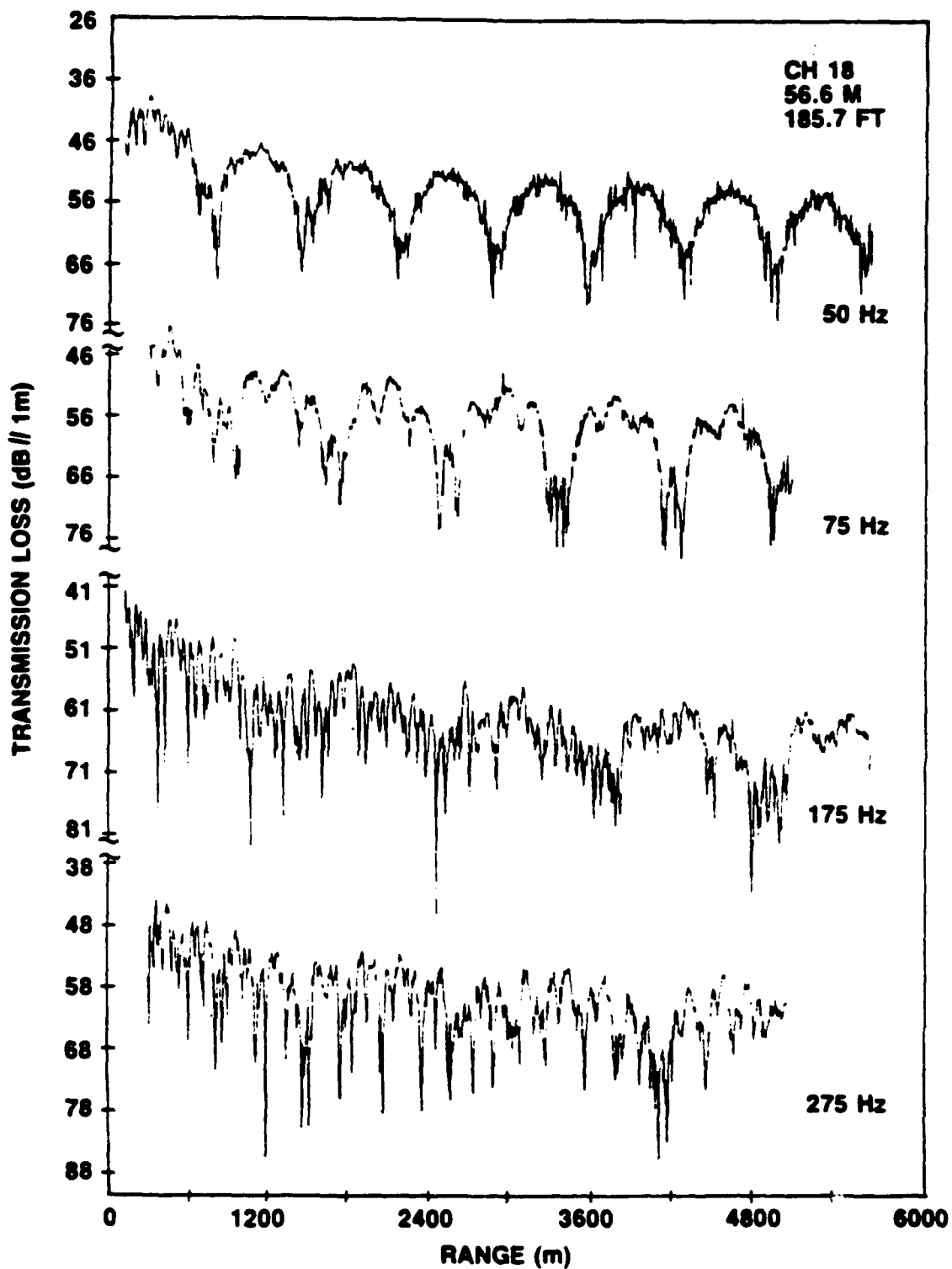
Figure 4-4 Transmission Loss Results for Four Frequencies

86

where a_1 and a_2 are the amplitudes of each mode. The envelope of the transmission loss will decay as a function of the square root of the range. This was also shown in Section 2.1.1. referring to the attenuation of the velocity potential due to cylindrical spreading. Multiplying equation 4-17 times its complex conjugate and reducing produces

$$|p(r)| = \frac{1}{\sqrt{r}}[a_1^2 + a_2^2 + 2a_1a_2\cos(k_{h1} - k_{h2})r]^{1/2} \qquad 4-18$$

The constructive and destructive interference pattern is controlled as shown in equation 4-18 as the cosine of the difference in the horizontal wavenumbers multiplied by the range. The difference in the wavenumbers of the two modes, Δk_r, can be calculated from measuring the distance between the nulls, or the "skip distance", on the propagation loss plots. The inverse of the measured distance is the difference in the wavenumbers. This can be thought of as calculating the difference between two "beating" frequencies by measuring the period T and inverting the result:

$$(k_1 - k_2)r = 2\pi \qquad 4-19$$

$$\Delta k_r = \frac{2\pi}{r}$$

$$\Delta k_r = \frac{2\pi}{685m} = .009175$$

This result for TL2-2, the synthetic aperture run, can be checked since the wavenumber spectra will be evaluated for this run. The deepness of the nulls of the processed data

indicates an excellent signal-to-noise ratio. The data for the transmission loss in Figure 4-4 were taken on Julian day 258 when calm seas were prevalent.

As the frequency increases, the waveguide is able to support more modes due to the inverse relationship between wavelength and frequency. This is shown by the increasing complexity of the transmission loss plots. Smoothing the data using a linear average of eight shows the pronounced effect of "mode stripping". This occurs because the higher order modes are dispersed or attenuated as the range increases. This results in a less complex, almost periodic, modal structure.

The Hudson Canyon experiment was conducted for two basic cases: a uniform depth radial and a sloping depth radial. A comparison of the 50 Hz transmission loss results is shown in Figure 4-5. The distinct interference pattern of the two modes can be seen in both cases. The data for the two plots were taken 3 days apart. The uniform radial test data were obtained on day 256, and the sloping radial test data on day 259. The robust nature of the interference pattern is evident. On closer inspection, the ranges below 4 km compare, but the modal structure between the ranges of 4 and 16 km shows some differences. Some of the nulls are not as deep or regular. The nulls caused by the interference of two modes is on the order of 20 dB. In the sloping bottom case at ranges greater than 6 kilometers, these nulls alternately measure 10 dB and 20 dB.
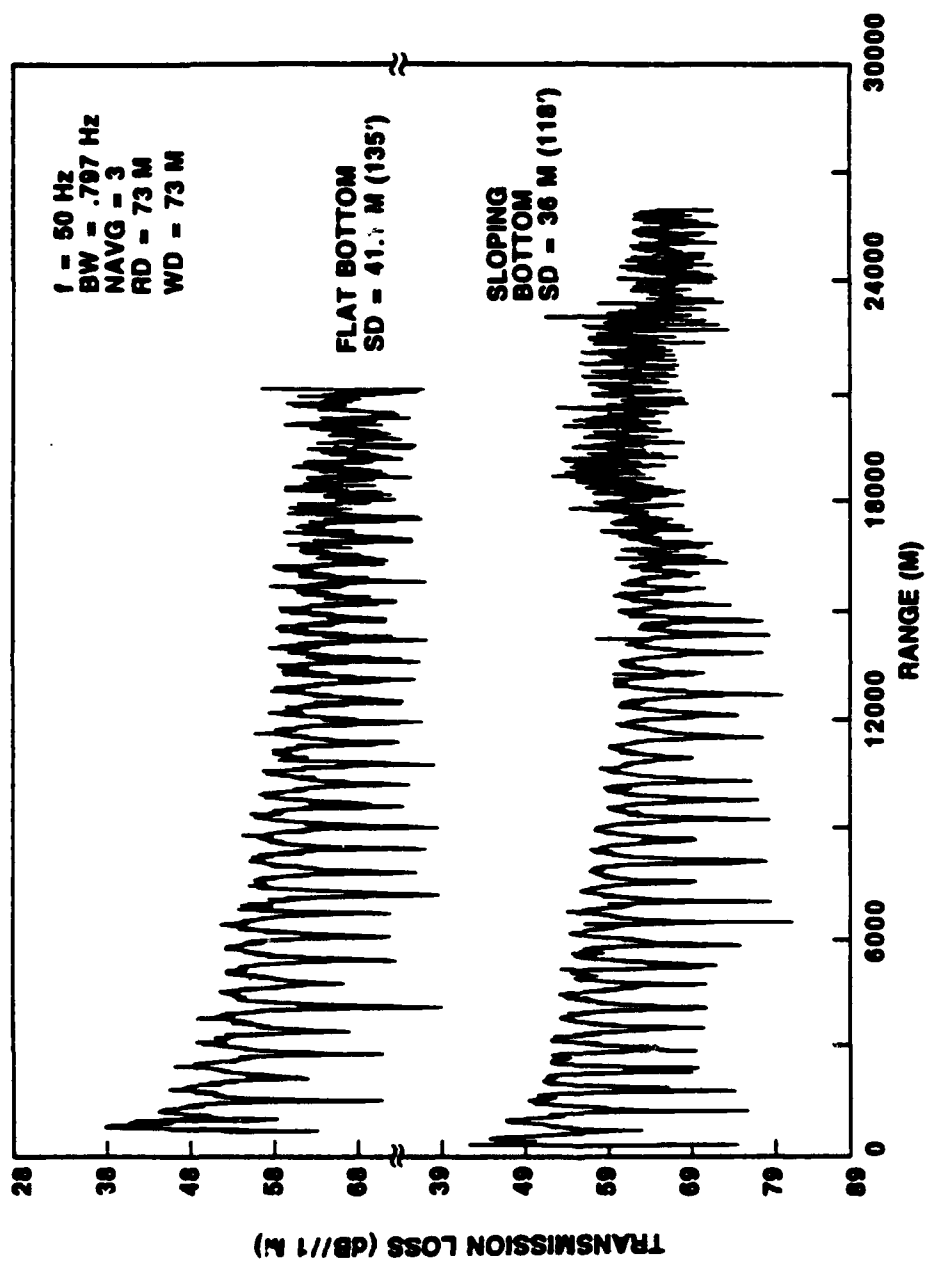
88

Figure 4-5 Transmission Loss, Sloping vs Uniform Bottom, 50 Hz

The controlling mechanism of modal propagation is the height of the waveguide (water depth), the position of the excitation (source depth), and the sound speed in the medium. The cutoff frequency for each mode is inversely proportional to the water depth. The skip distance of the uniform versus sloping bottom is different, averaging approximately 600 m and 570 m, respectively. The source depth is constant but the water depth is decreasing as a function of range for the sloping bottom case presented. It is apparent in both the uniform and sloping depth results that there are two modes propagating in the waveguide. The effect of bathymetry on transmission loss of the two runs is not significant enough to change the number of dominant modes but may contribute to the subtle differences seen in the modal structure. The variation in the "skip distance" could be attributed to the fact that as the water depth decreases, the distance travelled by the wave would decrease, or the velocity of the wave would appear to increase. This would result in the beating effect occurring more frequently, which would decrease the skip distance. The most likely cause of the differences in the skip distances is the temporally and spatially changing velocity profiles. The sound velocity in the deepest layer travels approximately 6 m/s faster during TL3-3, the sloping bottom case. This increase in sound velocity may partially contribute or may be the cause of the different skip distances between the two cases. The velocity profiles are presented

90

in the the oceanographic section of this paper.

A prominent difference occurs between the uniform versus sloping case at ranges greater than 16 km. This unusual effect is seen in all eight frequencies from 50 Hz to 600 Hz. Shown in Figure 4-6 are the 175 Hz results. Studies of the sediment thickness and sub bottom sea-mounts were reported by Milliman and Ewing of Woods Hole Oceanographic Institute. It appears that this effect can be attributed to a sub-bottom feature shown to exist in the vicinity of the radial run for test TL3-3 (Milliman et al. 1989).
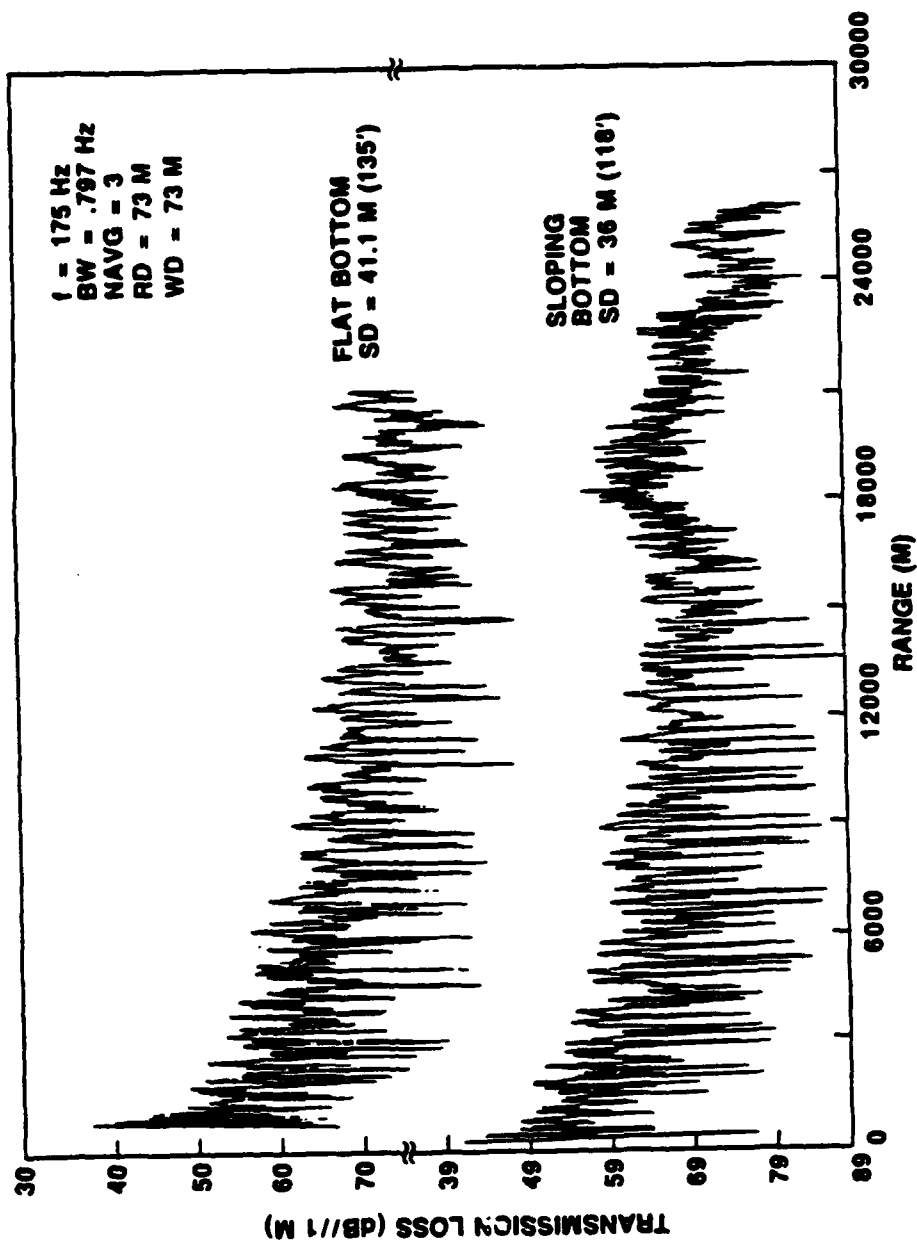
Figure 4-6 Transmission Loss, Sloping vs Uniform Bottom, 175 Hz

4.5 Determination of Wavenumber Spectra

In order to characterize the waveguide and identify the normal modes present, the Hankel Transform technique (Frisk and Lynch 1984) was used on the complex pressure versus range data. The hydrophone voltage level versus time data were analyzed in a sequential fashion using Fourier transforms. These Fourier coefficients represent the complex pressure versus time. The complex pressure versus time data are merged with the range versus time data obtained from the Del-Norte ranging system. This creates the synthetic aperture. The Hankel transform of the measured pressure field can be used to determine the depth dependent Green's function versus horizontal wavenumber and, as shown earlier, can be used to extract modal properties and characteristics of the bottom. The theory presented in Section 2.1.1 will provide a basis for the development of the experimental technique of calculating the wavenumber spectra. Although many of the equations will be repeated, the development will provide a step-by-step approach used in the computer programs to calculate the experimental wavenumber spectra.

Consider the case shown in Figure 4-7: a shallow water channel bounded by parallel reflectors at the ocean surface and bottom. The water column has a constant density ρ and a sound velocity profile which changes with depth as shown in Figure 4-7 as $c(z)$. The source is at some depth d in the
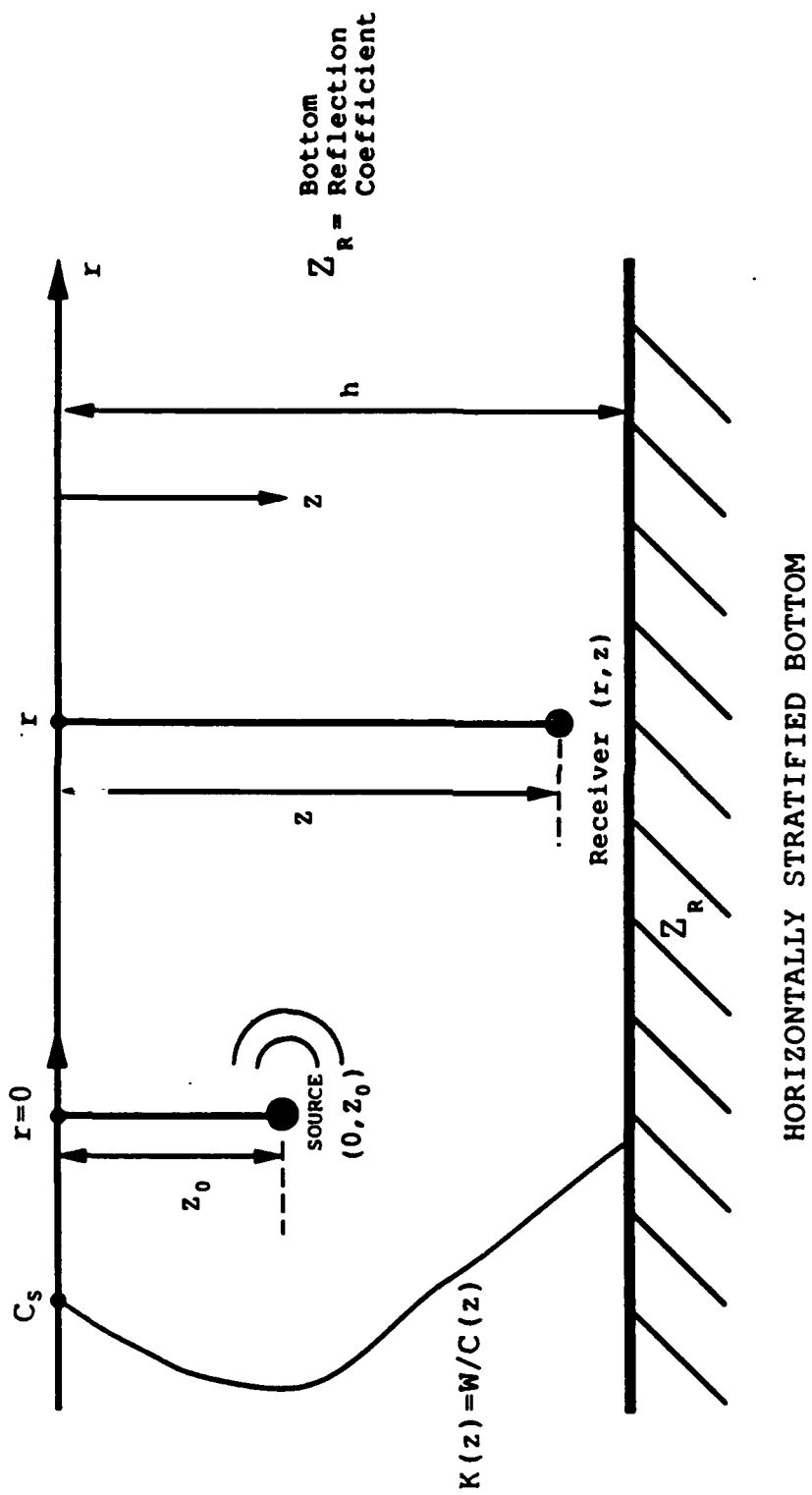
Figure 4-7 Horizontally Stratified Model of the Ocean

Z_R = Bottom Reflection Coefficient

h

z

r

Receiver (r,z)

HORIZONTALLY STRATIFIED BOTTOM

Z_R

z

$r = 0$

SOURCE $(0, z_0)$

z_0

$K(z) = W/C(z)$

C_S

water column of thickness h. The bottom is horizontally stratified. The governing differential equation 2-1 can be rewritten as the range-independent Helmholtz equation,

$$\left[\frac{1}{r}\frac{\partial}{\partial r}\left(r\frac{\partial}{\partial r}\right)+\frac{\partial^2}{\partial z^2}+k^2(z)\right]p(r;z,z_0)=-2\frac{\delta(r)}{r}\delta(z-z_0) \quad 4-20$$

where the wavenumber $k(z)=\frac{\omega}{c(z)}$, the point source is at range equal zero, and the depth equals the source depth z_0. The solution to this equation is the depth-dependent Greene's function (Frisk and Lynch 1984):

$$p(r)=\int_0^\infty g(k_r)J_0(k_r r)k_r dk_r \qquad 4-21$$

$$g(k_r)=\int_0^\infty p(r)J_0(k_r r)r dr \qquad 4-22$$

The function J_0 is the zero order Bessel function. The Bessel function can be replaced in the far field by Hankel functions of the first and second kind, from equation 2-23:

$$J_0(k_r r)=\frac{1}{2}[H_0^{(1)}(k_r r)+H_0^{(2)}(k_r r)] \qquad 4-23$$

The Hankel functions of the first and second kind represent a linear combination of two independent solutions for progressive waves. For values of $k \gg 1$, the asymptotic form may be used as an approximation, from equation 2-31:

$$H_0^{(1)}(kr)=H_0^{(2)*}(kr)\approx\sqrt{\frac{2}{\pi kr}}e^{i\left(kr-\frac{\pi}{4}\right)}. \qquad 4-24$$

It can be seen from equation 4-24 that the difference between the Hankel functions of the first and second kind depends on the direction of phase propagation. In the present experimental case, the Hankel function of the first kind is applicable. This corresponds to diverging or outgoing cylindrical waves. Substituting equation 4-24 into equation 4-22 gives

$$g(k_r) = \int_0^{\infty} p(r)\sqrt{\frac{2}{kr}}\, e^{i\left(kr - \frac{\pi}{4}\right)} r\, dr. \qquad\qquad 4-25$$

$$g(k_r)\sqrt{\frac{k}{2}}\, e^{-i\frac{\pi}{4}} = \int_0^{\infty} [p(r)\sqrt{r}]\, e^{ikr}\, dr$$

The approximate Hankel transform is now in a form that corresponds to a Fourier transform. The wavenumber spectra are obtained from the Fourier transform of the pressure field $p(r)$ multiplied by the square root of the range $\sqrt{r}$. Both the pressure field and the range are obtained from the experimental data. The Fourier transform is approximated by the use of Digital Fourier Transform (DFT) algorithms.

96

4.6 Synthetic Aperture Results

The complex pressure field determined from the Fourier transform of the hydrophone data as a function of range was used to determine the horizontal wavenumber spectra using the techniques developed in Section 4.5. The horizontal wavenumber spectra for 50 Hz are shown in Figure 4-8 for hydrophone 18. Hydrophone 18 was positioned at an approximate depth of 56 meters (3/4 water depth). The two peaks shown in the wavenumber spectra correspond to the two modes shown by the interference pattern of the 50 Hz transmission loss results. The peaks are separated by a distance Δk_r inversely proportional to the "skip distance." The two peaks occur at wavenumbers $k_{h1} = .1964$ and $k_{h2} = .1874$. These numbers can be compared to the water wavenumber, which defines the maximum wavenumber physically able to propagate in the waveguide for a specific water depth. The water wavenumber is calculated by the equation

$$k = \frac{\omega}{c_1} = \frac{2\pi(50Hz)}{1496m/s} = .21000 \qquad 4-26$$

where c_1 is the average sound speed in the water column from Section 3.1.2.1. The above calculation can be compared with the experimental wavenumbers to determine if the experimental results are reasonable. The calculated wavenumbers are close but do not exceed the water wavenumber. This is expected since the water wavenumber defined in Section 2.1.1 is the sum of the vertical and horizontal
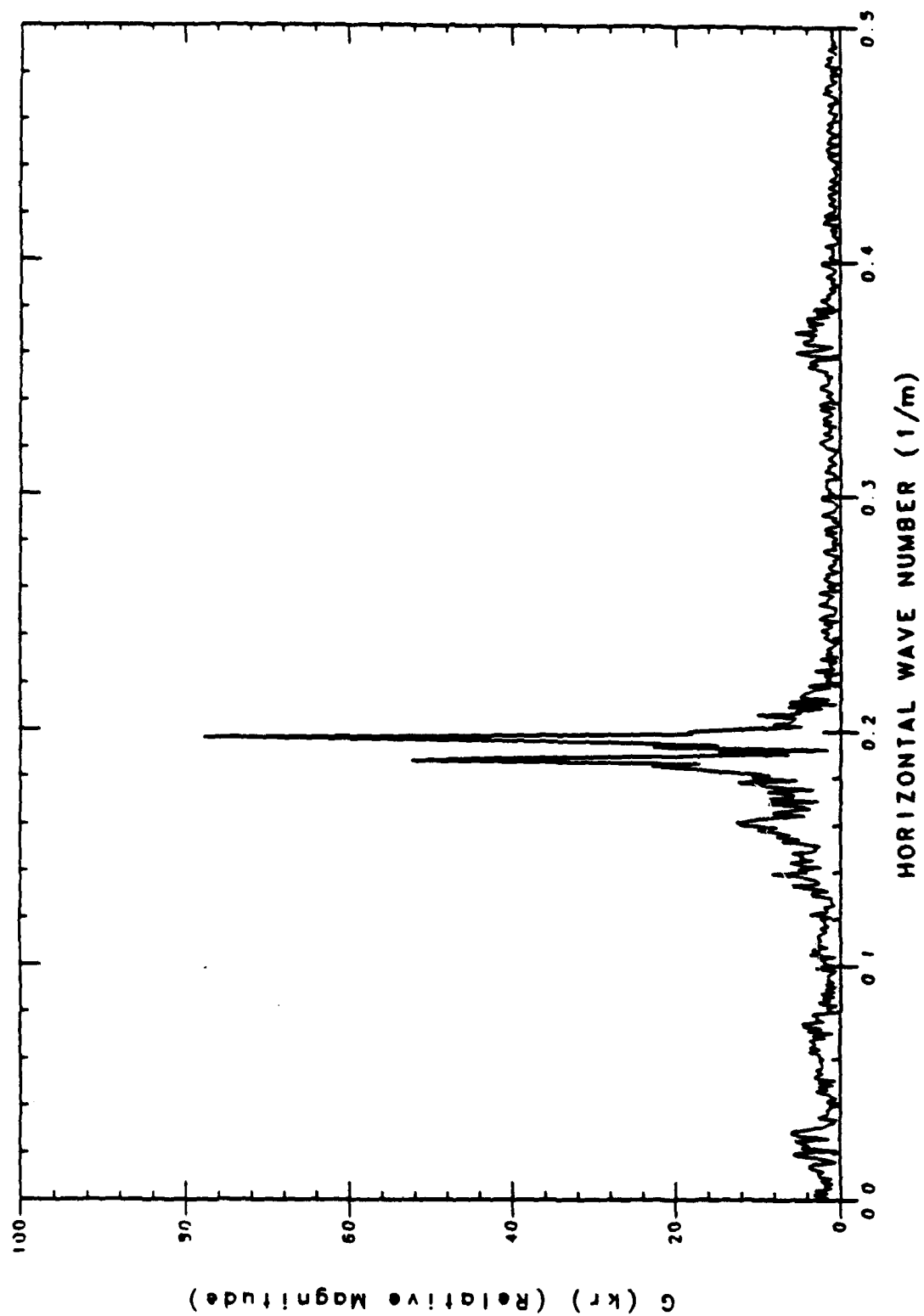
Figure 4-8 Experimental Wavenumber Spectra, 50 Hz

HORIZONTAL WAVE NUMBER (1/m)

G (kr) (Relative Magnitude)

98

wavenumbers.

The two important features to note in Figure 4-8 are
the position of the two dominant wavenumbers and their
amplitude. The relative strength of each of the modes and
their position in the wavenumber spectra will determine the
modal interference pattern. In the given case, the ampli-
tude of $k_{h2} = .7k_{h1}$, so a strong modal interference is
expected. This is apparent in the 50 Hz transmission loss
results shown in the previous section. Using equation 4-19,
the measured wavenumbers k_1, and k_2, and the measured
amplitudes a_1 and a_2, the propagation loss as a function of
range could be computed. Also the "skip distance" can be
solved by using the relationship

$$r = \frac{2\pi}{k_1 - k_2} = \frac{2\pi}{.00900} = 698\,m$$

In the previous section, the measured "skip distance" was
used to compute the difference in the wavenumbers, which
was calculated to be .009175 compared with the measured
.00900. Also the measured skip distance of 685 m can be
compared to the calculated distance of 698 m.

Two of the important parameters controlling propaga-
tion are the group velocity and the phase velocity. The
phase velocity is determined by the physical nature of the
medium, whereas the group velocity is the sum total of all
the wave trains travelling at different velocities and dif-

ferent frequencies. The following equations relate these two parameters:

$$U = \frac{d\omega}{dk} = \frac{d(Vk)}{dk} = V + k\frac{dV}{dk} \qquad\qquad 4-27$$

where U is the group velocity and V, the phase velocity. The relationships in equations 2-35 and 4-27 were used to estimate wavenumbers at the lower frequencies resulting in the following ratios:

$$k_n = \frac{\omega}{V_n} \qquad\qquad 2-1-33$$

$$\frac{k_{25}}{k_{50}} = \frac{\frac{2\pi(25)}{1.075}}{\frac{2\pi(50)}{1.025}} = .4767$$

$$k_{25} = .4767\, k_{50} = (.4767)(.1974) = .0941$$

$$k_{35} = .6916\, k_{50} = (.6916)(.1974) = .1365$$

The values for V are obtained using equation 2-35. This provides an estimate of the first mode for the lower frequencies of 25 Hz and 35 Hz using the 50 Hz experimental results.

5 Data Analysis and Comparison With Theory

The theoretical model chosen for the comparison of the experimental results was the computer code called SAFARI. The SAFARI model was chosen for many reasons. Primarily, SAFARI was capable of treating the bottom as a solid rather than a liquid. Values for shear wavespeeds could be incorporated into the sediment model, and comparisons of SAFARI predictions with and without the influence of shear could be made. Some researchers believe that shear has an important role to play in the propagation of sound through shallow water environments. Also, SAFARI can incorporate a layered sediment model including gradients of compressional wavespeed. This allowed the estimated geo-acoustical parameters for each layer in the sediment to be used in the predictions thus providing a more accurate representation of the environmental conditions.

Calculations were performed using the SAFARI-FIP module to obtain estimates of transmission loss versus range, wavenumber spectra, and pressure versus depth for comparison with the experimental data. The SAFARI-FIP module performs a single frequency calculation of the wavefield for a single source at multiple depths and ranges. The input parameters required by SAFARI for these calculations matched the experimental conditions as closely as possible. The compressional wavespeeds in the water column were derived from the CTD/SVP casts which produced the

velocity profiles presented in Section 3.1.2.1. The source, receiver, and water depths were obtained from the at-sea data logs which tracked each parameter at regular time intervals. The ranges from source to receiver were obtained from the Del Norte and LORAN computer log files. Sediment properties, such as compressional wavespeed, density, and shear wave speed, were taken from the T. Yamamoto (University of Miami) survey detailed in Section 3.1.1.2. A six layer sediment model shown in Table 5-1 was included in the input file used for the SAFARI predictions.

Table 5-1 Geo-acoustic Parameters of the 6010 Borehole Site

L	D(m)	$\rho\left(\frac{kg}{m^3}\right)$	$c_s\left(\frac{m}{s}\right)$	$c_p\left(\frac{m}{s}\right)$	$\alpha_p\left(\frac{dB}{\lambda}\right)$		$\alpha_s\left(\frac{dB}{\lambda}\right)$	
1	0-20	$2.00x10^3$	197.5	1803.3	0.18	0.45	1.16	1.72
2	20-50	$2.05x10^3$	327.6	2017.8	0.25	0.32	0.88	1.43
3	50-112	$2.15x10^3$	482.2	2129.5	0.15	0.36	0.67	1.64
4	112-150	$2.10x10^3$	617.2	2617.2	0.65	0.68	1.13	1.50
5	150-175	$2.15x10^3$	431.3	2002.1	0.09	0.38	0.35	1.02
6	175-200	$2.10x10^3$	690.1	2333.5	0.54	0.54	1.09	1.10

In this table, L is the layer number, D is the depth, c_s is the shear wavespeed and c_p is the compressional wavespeed. The attenuation in the layer for 10 and 100 Hz respectively is represented by α_p, which is the attenuation of the compressional waves and α_s, which is the attenuation of the shear waves.

Comparison of the pressure gradients calculated by

SAFARI and the experimental data yielded mixed results.
Shown in Figure 5-1 a,b is a comparison of the 25 Hz data
for two different source depths: 56 and 61 m, respectively.
The 25 Hz (56 m source depth) comparison in Figure 5-1 a
agrees very well, whereas the 25 Hz (61 m source depth)
comparison in Figure 5-1 b shows large differences. Shown
in Figure 5-2 is a comparison at 35 Hz. Both the SAFARI and
the experimental 35 Hz pressure profiles exhibit similar
characteristics (slope) near the bottom, but the mode shape
over the whole water column has a different structure.

The SAFARI calculations displayed a high sensitivity
to some of the input parameters, in particular range. Small
changes of the input range parameter (.1 km) produced radi-
cally different pressure profiles. This range sensitivity
is not evident in the experimental data. The pressure
profiles presented for 25 Hz (56 m source depth) and 25 Hz
(61 m source depth) were obtained at ranges of 1000 and
1300 m, respectively. The 35 Hz pressure profiles were
obtained at a range of 700 m. The experimental results show
similar mode shape characteristics independent of the
range.

SAFARI predictions of the transmission loss and wave-
number spectra for frequencies of 25 Hz and 35 Hz were
useful in explaining the range sensitivity seen in the
SAFARI pressure versus depth predictions. Shown in Figure
5-3 a,b are the SAFARI wavenumber calculations for 25 and
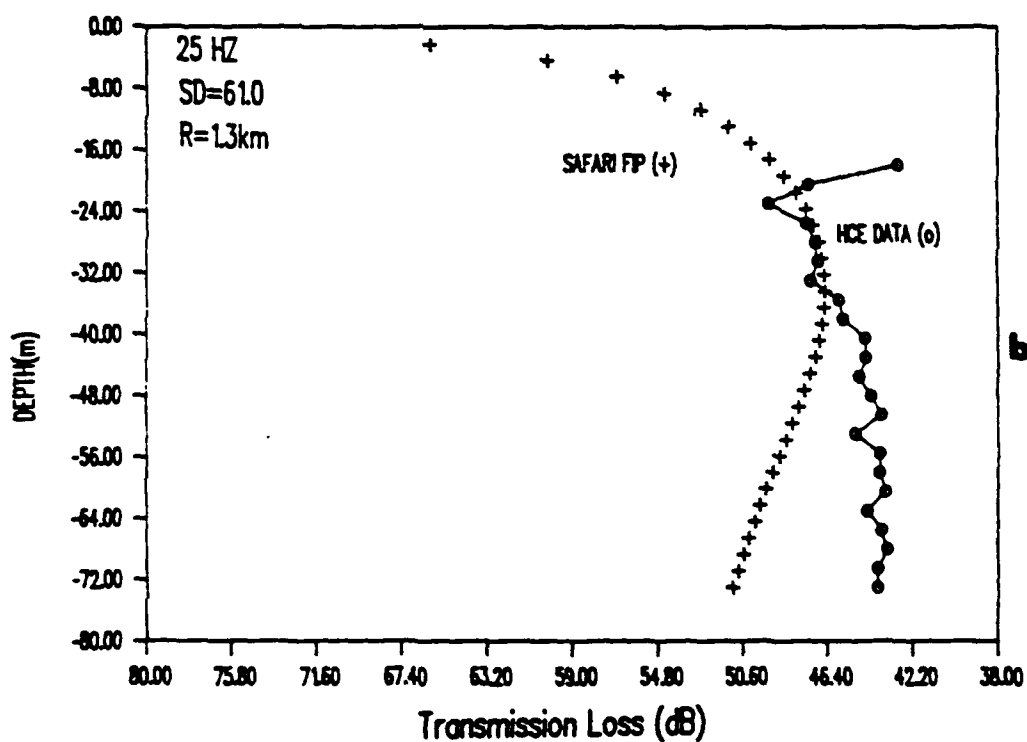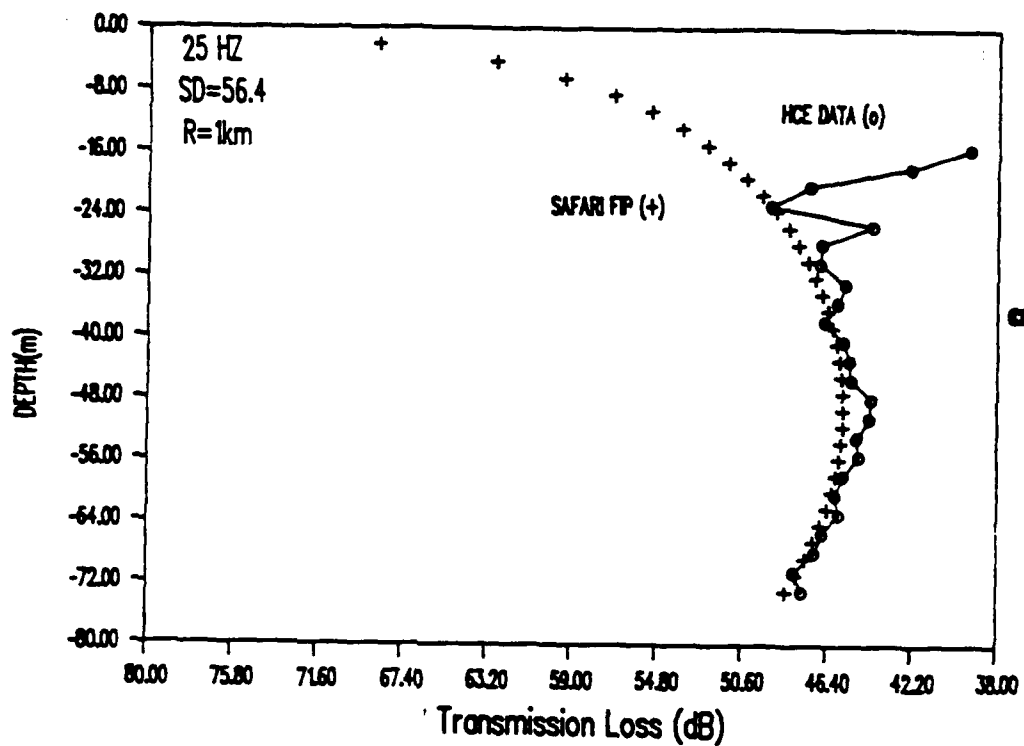35 Hz. SAFARI does not predict one propagating mode. An

Figure 5-1 SAFARI Pressure Profiles vs Experimental
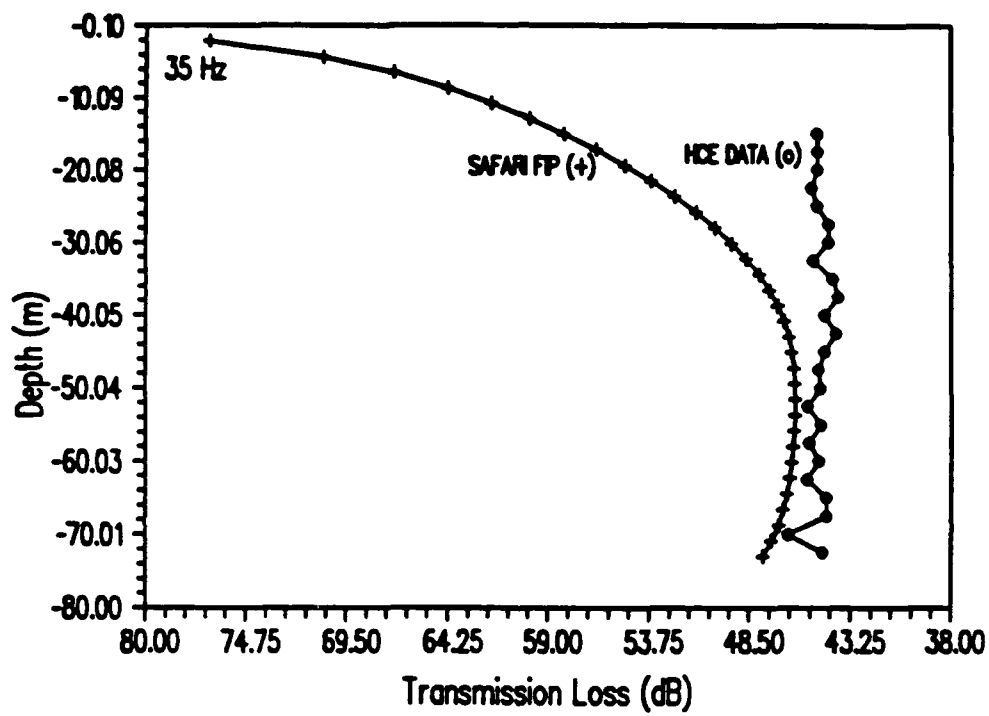Data, 25 Hz a. 56 m Source Depth ,
b. 61 m Source Depth

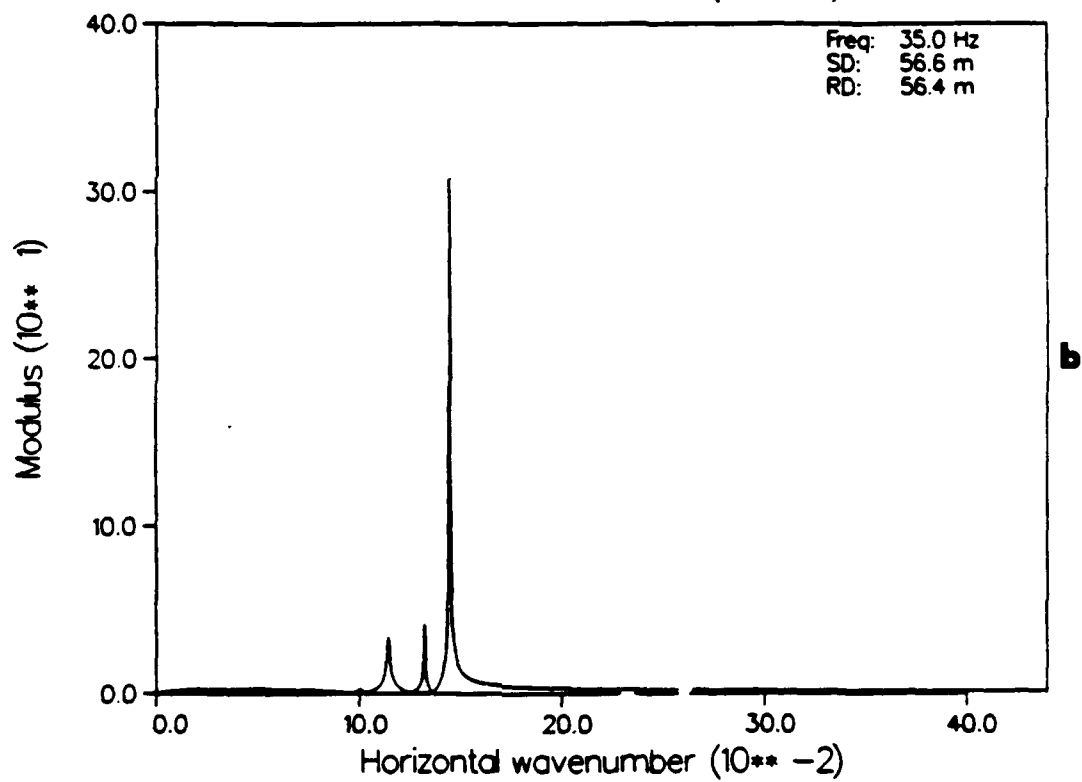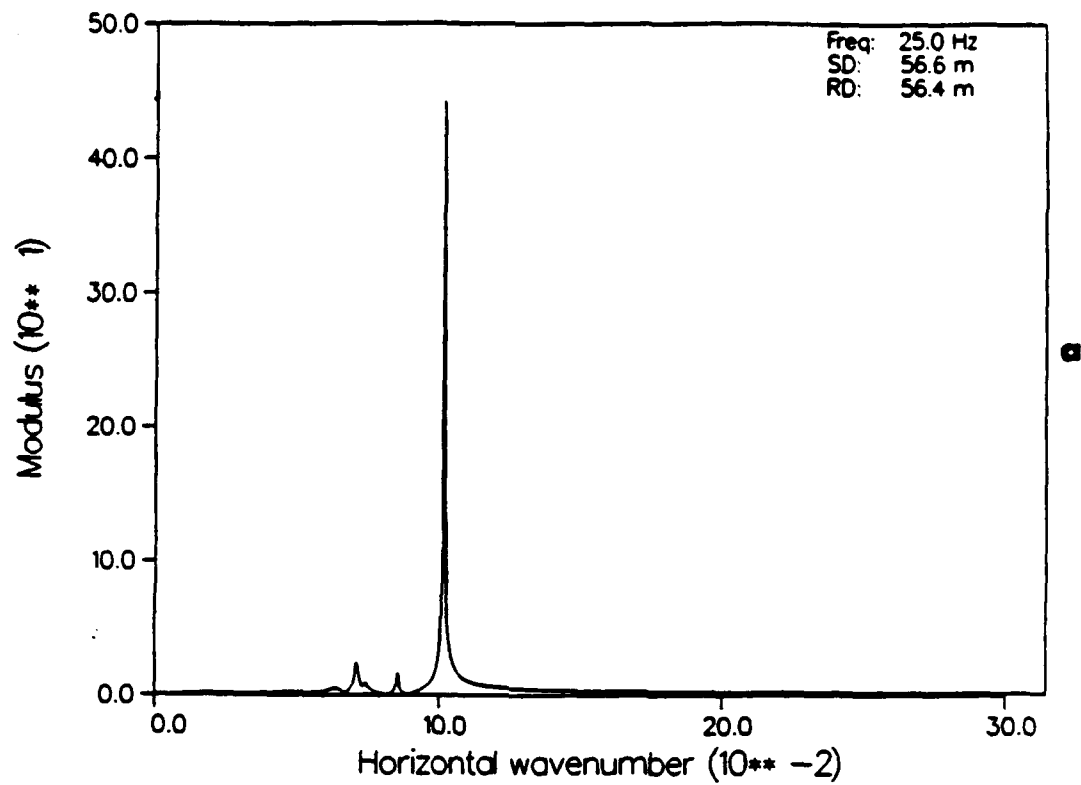Figure 5-2 SAFARI Pressure Profiles vs Experimental
Data, 35 Hz

Figure 5-3 SAFARI Wavenumber Spectra, 25 Hz, 35 Hz
a. 25 Hz , b. 35 Hz

additional two modes, for a total of three, are present in both the 25 and 35 Hz calculations. The dominant mode for 25 and 35 Hz occurs at wavenumbers of .1026 and .1458, respectively. The magnitudes of the higher order modes are small when compared to the dominant mode. The higher order modes for 25 Hz are 1/20 (13 dB) the strength of the dominant mode; the 35 Hz modes are approximately 1/10 (10 dB) the dominant mode. The impact of these higher order modes is apparent in the predicted pressure versus range calculations. Shown in Figure 5-4 a,b are the SAFARI transmission loss versus range calculations for 25 Hz and 35 Hz. At close ranges, where the experimental data for the pressure versus depth profiles were obtained, a distinct modal interference pattern can be observed. The fluctuations in transmission loss (4-5 dB in the 25 Hz case and 7-10 dB in the 35 Hz case) correspond to the range sensitivity of the pressure versus depth predictions.

The SAFARI wavenumber calculations can also be compared to the wavenumbers computed from the phase velocity or dispersion curves using equations 2-33 and 2-35. For 25 Hz, the SAFARI wavenumber is .10256 and the wavenumber computed from equation 2-33 is .0973 (5% difference). For 35 Hz, the computed wavenumbers are .14578 (SAFARI) and .1365 (equation 2-33), a difference of 6%.

Calculations of the effect of shear properties in the sediment were compared to results without shear. In order to support shear waves, the bottom had to be modeled as a
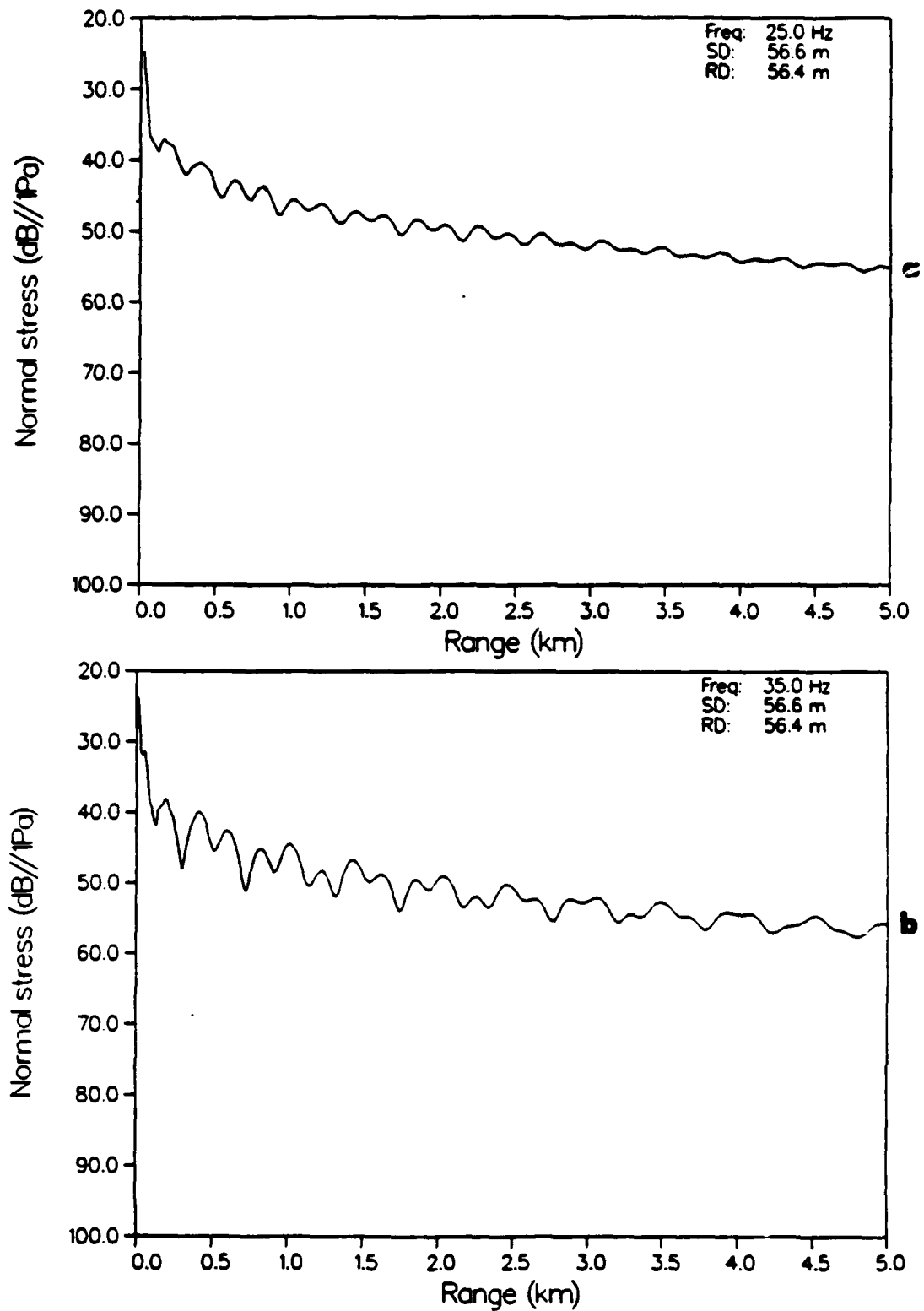
Figure 5-4 SAFARI Transmission Loss, 25 Hz, 35 Hz

a. 25 Hz , b. 35 Hz

solid. Without shear the bottom could be modeled as a liquid of different densities and wavespeeds at the interface. The SAFARI transmission loss calculation for 50 Hz with and without shear is shown in Figure 5-5. The difference between the solid and liquid bottom computations is indistinguishable.

The SAFARI calculation shown in Figure 5-5 was performed by R. Evans using environmental conditions modelled after run TL2-2. These results can be compared to the 50 Hz experimental results shown in Figure 4-4. Although the transmission loss levels agree, a number of differences in the modal structure can be noted. The most obvious difference between the two is the absence of the deep nulls in the SAFARI predictions. The deep nulls are produced by the interference of two modes in the waveguide. The SAFARI calculation appears more complex predicting the presence of additional modes. Also, the "skip distance" between the nulls is greater in the experimental results. The "skip distance" in the SAFARI calculation is 582 meters compared to 685 meters for the synthetic aperture results.

Figure 5-6 a,b shows the SAFARI 50 Hz wavenumber calculation for a solid versus liquid bottom. There are two dominant modes indicated by the two peaks in the wavenumber spectra. These peaks occur at wavenumbers .197 and .209. These can be compared to the wavenumbers obtained from the experimental data of .1874 and .1964. The difference in the
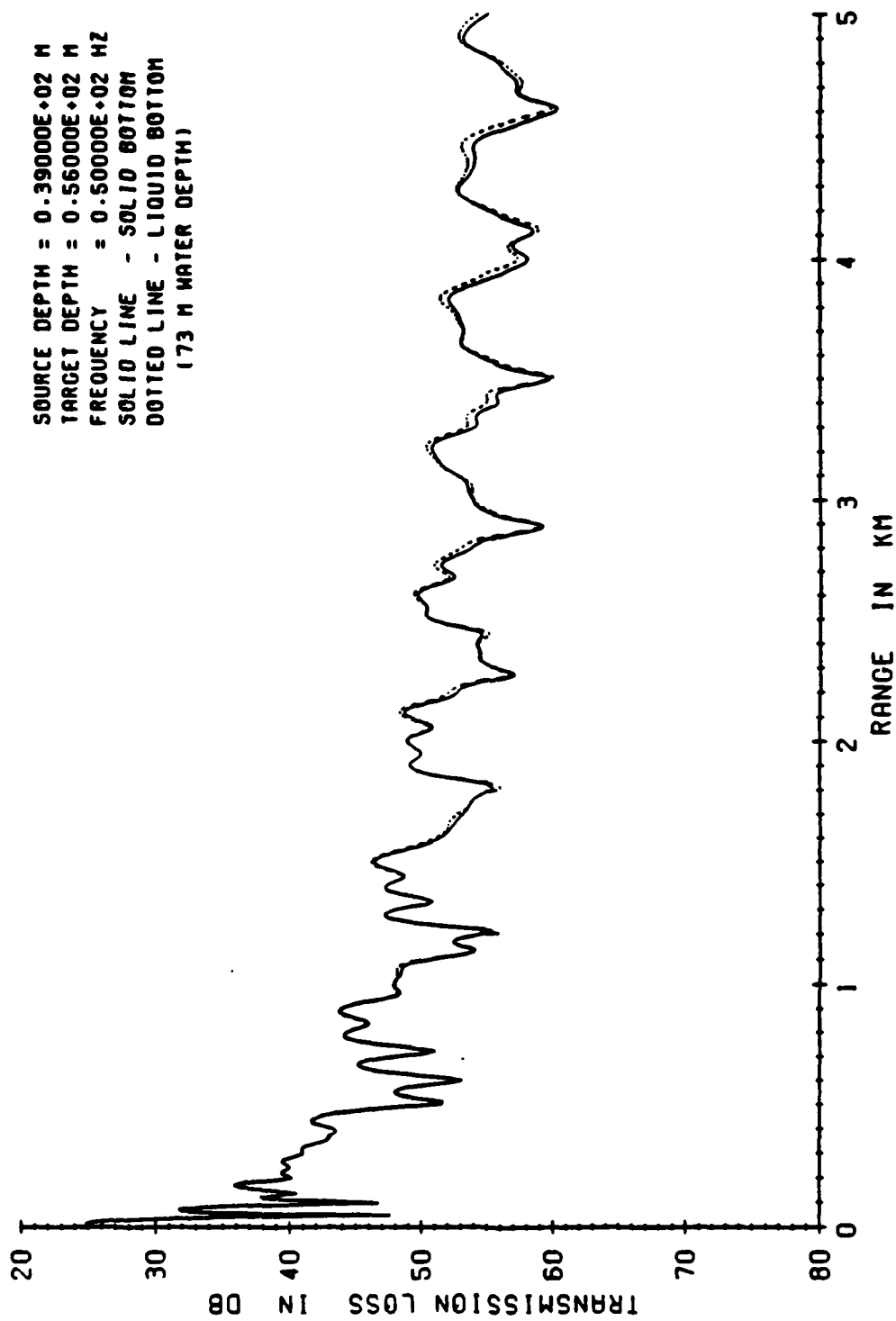
Figure 5-5 SAFARI 50 Hz Transmission Loss, Solid vs Liquid Bottom

SOURCE DEPTH = 0.39000E+02 M
TARGET DEPTH = 0.56000E+02 M
FREQUENCY   = 0.50000E+02 HZ
SOLID LINE - SOLID BOTTOM
DOTTED LINE - LIQUID BOTTOM
(73 M WATER DEPTH)

RANGE IN KM

TRANSMISSION LOSS IN DB

110
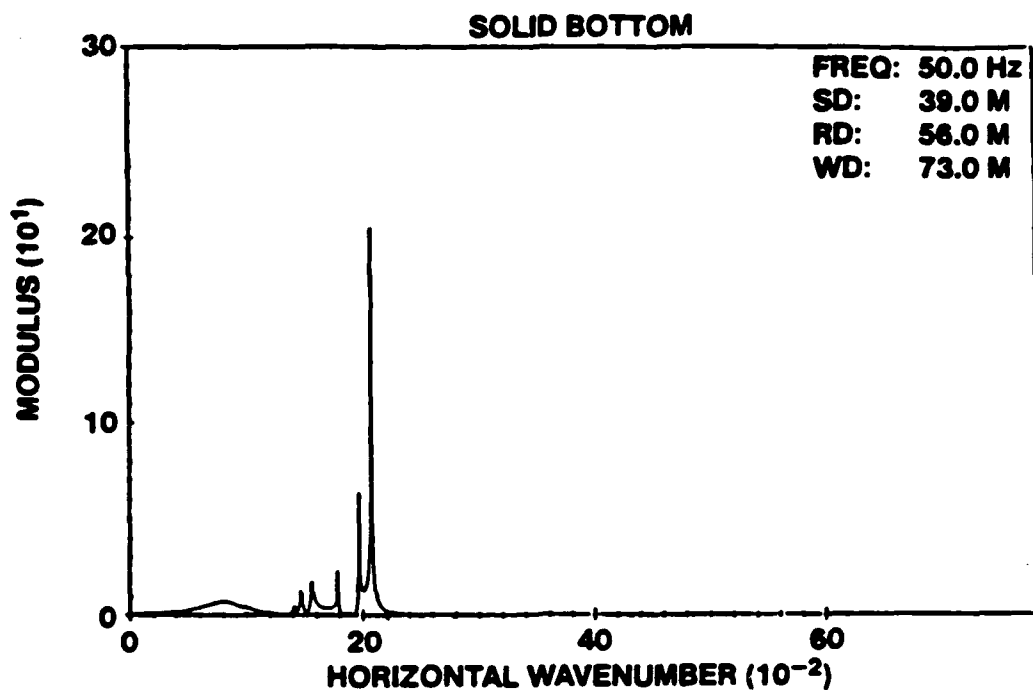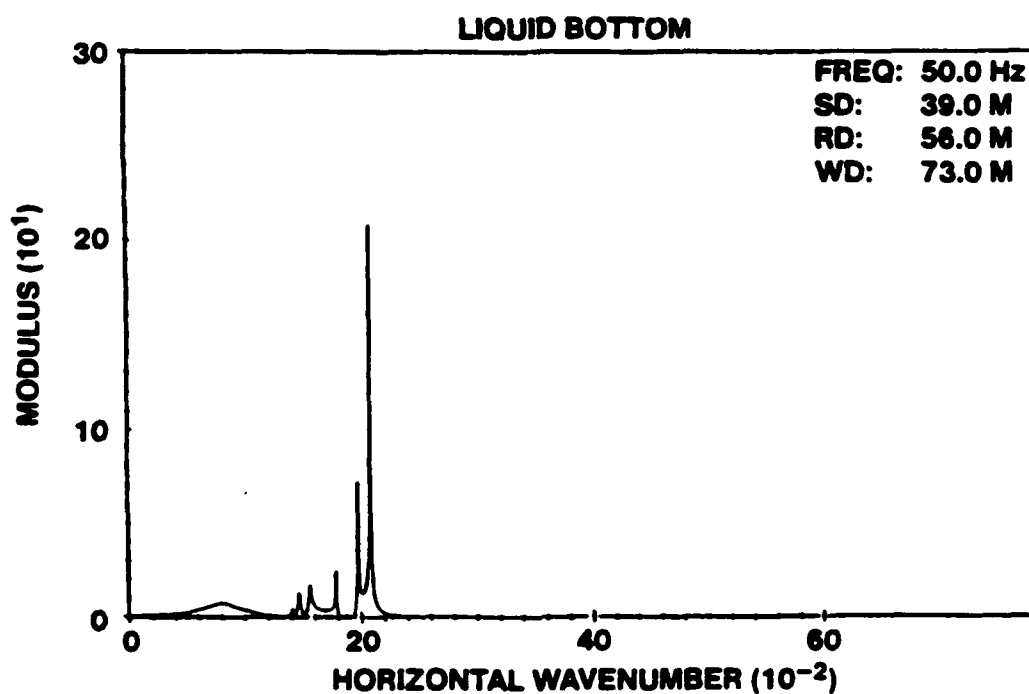
Figure 5-6 SAFARI 50 Hz Wavenumber Spectra,

a. Solid, b. Liquid Bottom

position of the dominant wavenumber of the SAFARI calculation and the data is .0126, or about 6%. This shows good agreement between the two. The difference in the wavenumber between the two modes, or the δK_r, is .012, or 6%, for the SAFARI calculations compared to .011, or 5.6%, in the data. Another notable difference is in the relative magnitudes of the wavenumbers. In the data we see equal or near equal strength of the modes, whereas in the SAFARI calculations the second mode is 1/3 the strength of the first mode. The most significant result contained in the SAFARI results is the prediction of higher order modes at wavenumbers .1800, .1567, and .1467. Although these modes have relatively little strength, approximately 1/10, they do contribute to the resulting modal structure. The difference in the relative magnitude of the peaks and the additional modes explains the complexity seen in the SAFARI predictions.

Since the measurements of source depth and water depth have some errors due to the experimental process, a sensitivity study of SAFARI results was performed by varying these parameters. Shown in Figure 5-7 are the 50 Hz transmission loss results for a variation in water depth of 71 to 75 m. Although the effect of water depth on modal propagation can be easily seen by the increasing complexity of the structure predicted as the water depth increases, the effect of varying the water depth is not significant enough to obtain a similar modal interference pattern, as seen in the experimental data. Varying the source depth
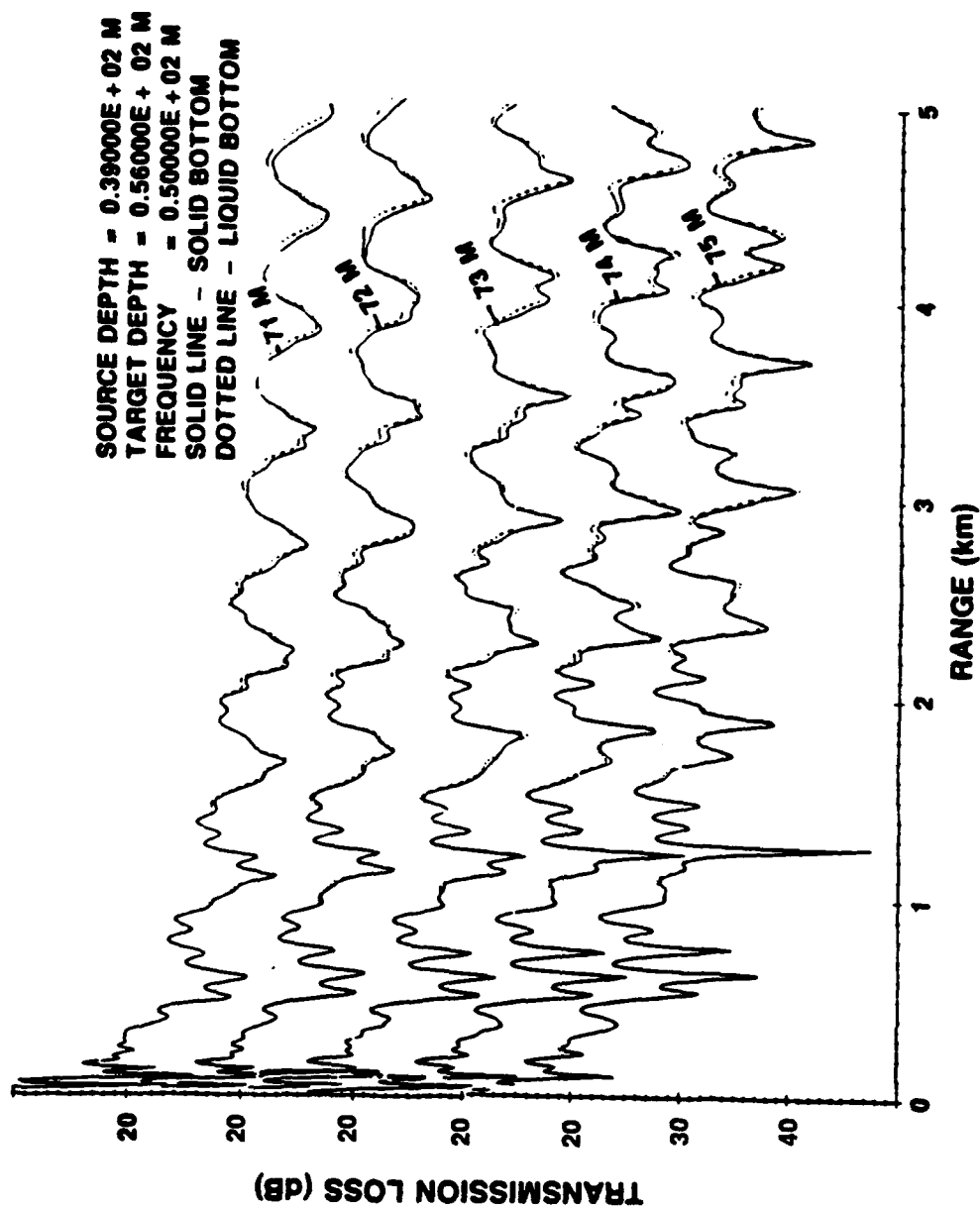
112

Figure 5.7 Effect of Water Depth Variation on SAFARI Calculations

113

between 35 and 39 m produces smaller changes in the pre-

dicted propagation, shown in Figure 5-8, but still does not

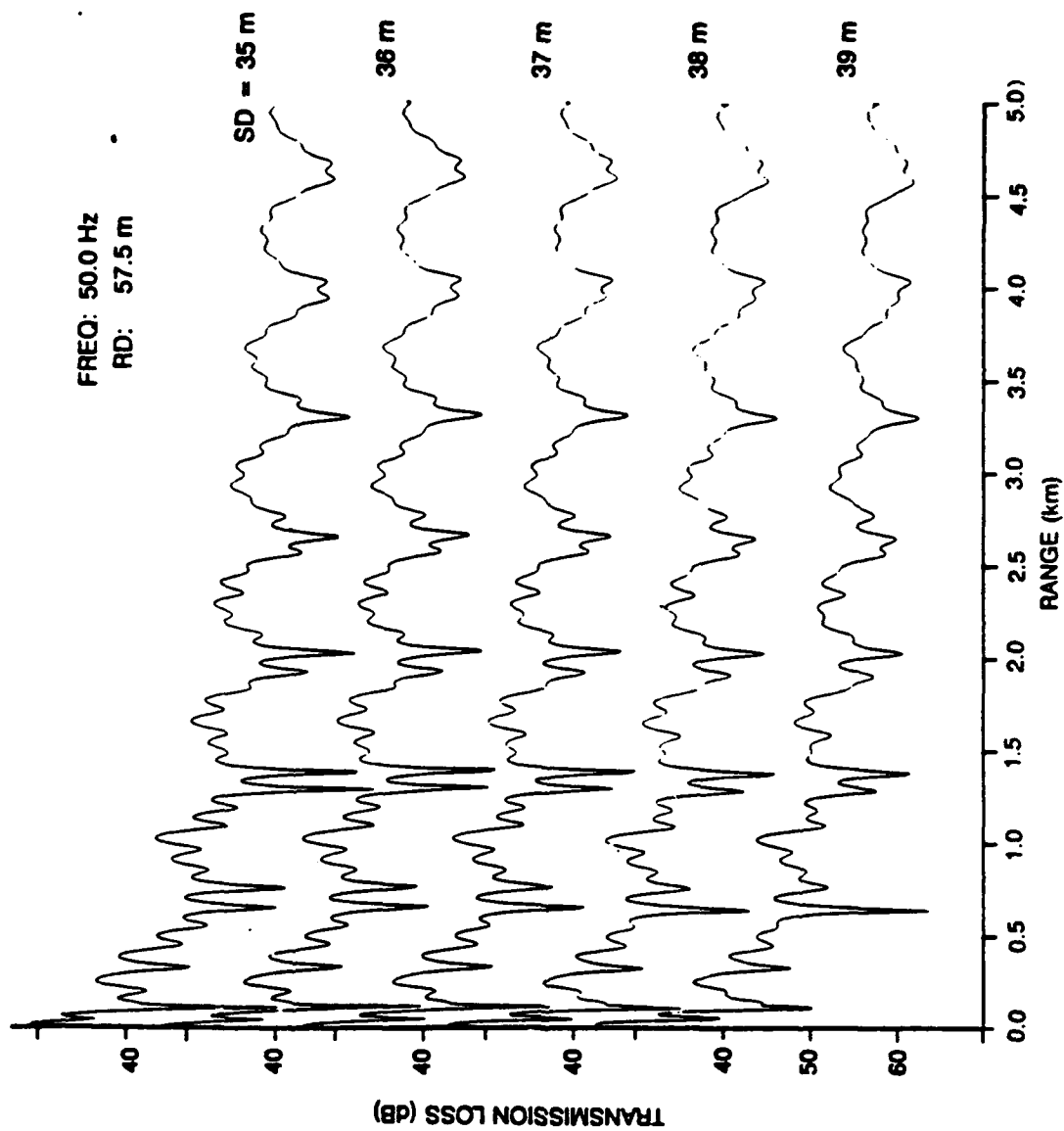predict the strong interference seen in the data.

Figure 5-8 Effect of Source Depth Variation on SAFARI Calculations

6 Discussion, Conclusions, and Recommendations

In summary, a high quality acoustic data set was obtained in a shallow water waveguide at several discrete frequencies for the analysis of boundary impedance, transmission loss, and wavenumber spectra. The experimental site was selected in a surveyed area which provided estimates of the geo-acoustic properties of the sediment. Oceanographic and bathymetric data were collected during the experiment to produce accurate representations of sound velocity versus depth and water depth. The experimental results were compared to predicted results using the theoretical model SAFARI. The SAFARI code used the estimated geo-acoustical parameters and the measured oceanographic data to perform its calculations.

Sound waves at frequencies between 10 and 55 Hz were transmitted over ranges of approximately 1 km to measure the pressure at the sediment water interface and the gradient of the pressure near the interface for the determination of impedance. Signals with frequencies less than 20 Hz were observed to have low signal-to-noise ratios. The received signals for 25, 30, and 35 Hz were found to have higher signal-to-noise ratios and appeared to be dominated by a single mode. The received signals with frequencies of 45 and 55 Hz were observed to have a more complex structure indicating additional dominant modes. These results were

reinforced by the estimates of signal phase variation versus depth.

The bottom boundary impedance was determined at frequencies shown to be dominated by a single mode. The boundary impedance calculations for 25, 30, and 35 Hz were performed using estimates of near bottom gradient and the pressure at the water sediment interface. The results were variable, but in general were higher than expected when compared to the impedance calculated using the estimated geo-acoustical parameters.

Experimental pressure versus depth profiles were compared to theoretical profiles generated by the computer code SAFARI. Some agreement was obtained but in general, the pressure profiles calculated by the SAFARI code were found to be very sensitive to small changes (.1 km) in the range input parameter. SAFARI calculations of transmission loss and wavenumber spectra at 25 and 35 Hz predict the presence of additional weak modes that are 10 to 13 dB the strength of the dominant mode. The interference of these modes can be seen in the transmission loss results and explains the variation with range of the pressure profiles.

The 50 Hz transmission loss results displayed a distinct and repeatable modal interference pattern clearly resulting from two dominant modes. The 50 Hz wavenumber spectra exhibit two large peaks which represent these two modes. This repeatable modal interference pattern was observed under a number of varying conditions. The temporal

and spatial changes of the velocity profiles in the water column, water depth, and source depth produced subtle changes but the distinct modal interference pattern persisted

The 50 Hz experimental transmission loss and wavenumber spectra results were compared to calculations performed by SAFARI. The resultant comparisons of transmission loss agree in level, whereas differences in the modal structure can be noted. The SAFARI transmission loss calculation displays a more complex modal structure which is not seen in the experimental results. The SAFARI calculations of wavenumber spectra predict two dominant modes along with a number of higher order, smaller amplitude modes. The presence of these lower wavenumber, higher order modes causes the complexity of the SAFARI transmission loss calculations. The results of SAFARI calculations with and without shear produce indistinguishable results, and a variation of input parameters, source depth, and water depth does not significantly change the modal structure.

The practical utility of the boundary impedance technique is very difficult to assess. The only comparison of the impedance can be made using the estimated geo-acoustical parameters. In general, the experimental impedance was higher than expected and variable. Two experimental values fell within the bounds of the geo-acoustical estimates. The variability in the experimental estimates was due to errors in calculating the pressure gradient near

118

the boundary and the inability to obtain adequate signal-to-noise ratios at those frequencies predicted to be below the cutoff frequency for single mode propagation. Calculations of the vertical wavenumber spectra and the dispersion curves could be useful in determining the pressure versus depth profiles. The pressure gradient could then be determined from the derivative at the boundary and the impedance calculated with less error. To further the investigation of this boundary impedance technique, additional experiments could be performed in shallower water (to get below cutoff) with a stronger low frequency source.

7 Bibliograpy

Brekhovskikh, L.M. 1980. _Waves in Layered Media_. New York:
Academic Press, Inc.

Brekhovskikh, L.M., and Yury Lysanov. 1982. _Fundamentals of Ocean
Acoustics_. Heidelberg, Germany: Springer-Verlag.

DiNapoli, F.R., and R.L. Deavenport. 1980. Theoretical and
Numerical Greene's Function Field Solution in Plane and Multilay-
ered Medium. _J. Acoust. Soc. Am._ 67: 92-105.

Frisk, George V., and James F. Lynch. 1984. Shallow Water
Waveguide Characterization Using the Hankel Transform. _J. Acoust.
Soc. Am._ 76: 205-216.

Harraka, A. 1988. Final Report, Hudson Canyon Experiment: NUSC
contract no. N6604-87-D-0550-0013. Syntek Engineering and Com-
puter Systems, Inc.

Milliman, J. D., Jiezao, Z., Anchun, L., and J. I. Ewing. 1989.
Late Quaternary Sedimentation on the Outer and Middle New Jersey
Continental Shelf: Result of Two Local Deglaciations. Report:
Woods Hole Oceanographic Institute, Woods Hole, MA, and Academia
Sinica Institute of Oceanology, Quigdao, Peoples Republic of
China.

Officer, C. B. 1958. _Introduction to the Theory of Sound
Propagation_. New York: McGraw-Hill Book Company.

Parssinen, E. 1988. Summary of Work on Acoustic Source for Hudson
Canyon Project: NUSC contract no. N6604-86-D0120. Planning
Systems, Inc.

Parssinen, E. 1989. Review of Projector Source Levels on 1988
Hudson Canyon Experiment: NUSC contract no. N6604-89-M-G374.
Kildare Corp.

Pekeris, C. L. 1948. Theory of Propagation of Explosive Sound in
Shallow Water. _Propagation of Sound in the Ocean_. The Geological
Society of America. Waverly Press.

Schmidt, H. 1988. SAFARI Seismo-Acoustic Fast Field Algorothm for
Range Independent Environments, Users Guide. SACLANTCEN Report
SR-113.

Tolstoy, I. 1973. _Wave Propagation_. New York: McGraw-Hill Book
Company.

Trevorrow, M., Yamamoto, T., Turget, C., Abbot, C., Baidey, M., Goodman, D., Nye, T., and K. Ando. 1988. Summary of Ocean Bottom Seismic and Pressure Measurements Taken in July, 1988 on the New Jersey Shelf and Georges Bank. University of Miami Technical Report, RASMAS TR-88-005.

Urick, Robert J. 1967. Principles of Underwater Sound for Engineers. New York: McGraw-Hill Inc.

INITIAL DISTRIBUTION LIST

Addressee	No. of Copies
ONR (M. Orr, R. Feden)	2
DARPA (W. Carey)	1
Univ. of Miami (T. Yamamoto)	1
SAIC (R. Evans)	1
WHOI (J. Doutt, S. Rajan)	2
Kildare, Corp. (J. Fitzgerald, E. Parssinen)	2
Rensselaer Polytechnic Institute (W. Siegmann)	1
PSI (J. Davis)	1
DTIC	12